Modifying the Wetting Behavior of Teflon AF1600 and PDMS Thin Films

Zur Erlangung des akademischen Grades
Doktor der technischen Wissenschaften (Dr. techn.)

Insitutue für Sensor- und Aktuatorsysteme
Technische Universität Wien

Yijie XIANG, Msc.
Matrikelnummer: 11919894

Supervisor: Univ. Prof. Dr. Ulrich Schmid

Wien, February 2024

Defense	Vienna 11/4/2024
Supervisor:	Univ. Prof. Dr.rer.nat Ulrich Schmid TU Wien, Österreich
Reviewer:	Prof. Dr. Gerald Urban Albert-Ludwigs-Universität Freiburg, Deutschland
Reviewer:	Univ.Prof. Dipl.-Ing. Dr. Peter Ertl TU Wien, Österreich

Acknowledgments

I extend my deepest gratitude to my supervisor, Prof. Ulrich Schmid, for not only providing me with the opportunity to conduct my thesis at the Institute of Sensor and Actuator Systems but also for fostering an environment of freedom and support throughout my research journey. His guidance, advice, and wealth of experience have been invaluable to me.

I am indebted to my colleagues and the entire team at ISAS for their unwavering support, both scientifically and administratively. While it is challenging to single out individuals amidst a collective effort, I wish to express special thanks to the technicians, Michi, Sophia, and Patrick, for their exceptional dedication and contributions.

I am particularly grateful to Dr. Paul Fulmek, my closest colleague, whose rigorous thinking and work have inspired me throughout this journey. His support and collaboration have significantly enriched my project and academic experience.

I would also like to acknowledge Dr. Daniel Platz for his support and assistance, which have been instrumental in overcoming challenges and achieving milestones.

At TU Wien, I extend my appreciation to Dr. Markus Sauer and Dr. Annette Foelske from the X-ray center for their expertise and assistance with XPS experiments, which provided valuable insights for my research.

To my parents, whose financial support enabled me to relocate to Vienna and embark on my studies at TU Wien, I offer my heartfelt thanks. Their belief in me has been a constant source of motivation and encouragement.

I would also like to express my gratitude to my significant other, my beloved cats, and all my friends for their unwavering support and encouragement throughout the ups and downs of my academic journey.

Thank you to everyone who has played a role, big or small, in shaping my academic and personal growth. Your support has been instrumental, and I am profoundly grateful for it.

Kurzfassung

Diese Studie präsentiert eine umfassende Untersuchung der Oberflächeneigenschaften von zwei weit verbreiteten hydrophoben Materialien, nämlich Teflon AF1600 und Polydimethylsiloxane (PDMS). Ferner befasst es sich mit den temperaturabhängigen Benetzungseigenschaften. Dabei werden verschiedene fortgeschrittene Techniken wie Kontaktwinkelmessungen, Rasterkraftmikroskopie (AFM), Rasterelektronenmikroskopie (SEM), Fourier-Transform-Infrarotspektroskopie (FTIR) und Röntgenphotoelektronenspektroskopie (XPS) eingesetzt, um die Benetzungseigenschaften, Oberflächentopografien und chemischen Zusammensetzungen zu untersuchen. Ein neuartiges Reibungs-Adsorptionsmodell (FA Modell) wird entwickelt, um die temperaturabhängige Kontaktwinkel von Wasser auf hydrophoben Materialien zu beschreiben. Das Modell geht davon aus, dass eine hydrophobe Oberfläche spezifische Adsorptionsstellen hat und die Adsorptionsenergie je nach verschiedenen Oberflächenbedingungen variiert. Oberflächen, die mit Luft (Fest-Luft-Grenzfläche) oder Wasser (Fest-Wasser-Grenzfläche) in Kontakt stehen, werden durch die Oberflächenspannung im Vakuum und die unterschiedlichen Adsorptionsenergien beschrieben. Zusätzlich wird immer beobachtet, dass der Kontaktwinkel konstant bleibt, während sich das Tropfenvolumen ändert, bis die vorrückenden und nachrückenden Kontaktwinkel erreicht sind. Daher wird ein weiterer Faktor eingeführt – die variable Reibungskraft mit einem Grenzwert (F_{fmax}). Die experimentelle Bestimmung beider Faktoren für Teflon AF1600 wird durch Kontaktwinkelmessungen erreicht. Das FA-Modell wird anschließend verwendet, um den Kontaktwinkel während der Elektrobenetzung (EW) auf Teflon AF1600 bei unterschiedlichen Temperaturen zu beschreiben und zeigt eine hohe Übereinstimmung bis zu einer Temperatur von 50 °C. Die Anwendbarkeit des Modells auf Teflon AF1600, das mit Sauerstoffplasma behandelt wurde, wird ebenfalls nachgewiesen, was einen effizienten Ansatz zur Charakterisierung von Benetzungsverhalten auf rauen und strukturierten Oberflächen ohne Kenntnis strukturbezogener Parameter ermöglicht. Die Validierung des FA-Modells erstreckt sich zusätzlich auf die EW dieser plasma-behandelten Oberflächen. Neben den Benetzungseigenschaften taucht die Studie in Oberflächentopografien und chemische Zusammensetzungen ein, um ein tiefergehendes Verständnis von Oberflächenmodifikationen durch Sauerstoffplasma-Behandlung zu schaffen. Während die Sauerstoffplasma-Behandlung hauptsächlich Material entfernt und nanoskalige Strukturen auf Teflon AF1600 erzeugt, führt sie auf der PDMS-Oberfläche zur Bildung einer steifen Oxidschicht. Auf PDMS-Oberflächen entstehen gebeulte Strukturen aufgrund des der unterschiedlichen mechanischen Eigenschfaten zwischen der steifen Oxidschicht und dem weichen PDMS-Bulk. Die Oberflächeneigenschaften (Benetzbarkeit und Topografien) von plasma-behandeltem Teflon AF1600 zeigen eine hohe Abhängigkeit von der angelegten Plasmaenergie, während für PDMS eine hohe Abhängigkeit zwischen Benetzbarkeit, Topografien und Schlüsselparametern wie Verdünnungsverhältnis, Schichtdicke und Plasmabehandlungszeit vorgestellt und diskutiert werden. Zusammenfassend trägt diese Studie

nicht nur zum grundlegenden Verständnis der Oberflächeneigenschaften von Teflon AF1600 und PDMS bei, sondern präsentiert auch einen neuartigen Modellierungsansatz, der dazu verwendet werden kann, Benetzungsverhalten unter verschiedenen Bedingungen zu analysieren und vorherzusagen. Damit ebnet sie den Weg von unterschiedlichsten, hydrophoben Oberflächen für einen weiteren Erkenntnisgewinn in den Oberflächenwissenschaften und zur Realisierung von zukünftigen Bauelementkonzepten.

Abstract

This study presents a comprehensive investigation into the surface properties of two widely used hydrophobic materials, namely Teflon AF1600 and polydimethylsiloxane (PDMS), including the temperature dependency of the wetting properties. Various advanced techniques including contact angle (CA) measurements, atomic force microscope (AFM), scanning electron microscopy (SEM), fourier-transform infrared spectroscopy (FTIR), x-ray photoelectron spectroscopy (XPS) are employed for the investigations of wetting properties, surface topographies, and chemical compositions. A novel Friction-Adsorption (FA) model is developed to describe the temperature-dependent water CA on hydrophobic materials. This model assumes that a hydrophobic surface has specific adsorption sites and the adsorption energy varies depending on different surface conditions. Surfaces that are in contact with air (solid-air interface) or water (solid-water interface) are described by the surface tension in a vacuum and the different adsorption energies. In addition, it is always observed that the CA stays constant while the droplet volume changes until reaching the advancing and receding CAs. Therefore, another factor – variable friction force with a limit value (F_{fmax}), is introduced. Experimental quantification of both factors for Teflon AF1600 is achieved through CA measurements. The FA model is then applied to describe CA when performing electrowetting (EW) on Telfon AF1600 at different temperatures, demonstrating high consistency at temperatures up to 50 °C. Furthermore, the model's adaptability to oxygen-plasma-treated Teflon AF1600 is demonstrated, offering a straightforward approach to characterize wetting properties on roughened and structured surfaces without information about the structure-related parameters. Additionally, validation of the FA model extends to EW on these plasma-treated surfaces. Beyond surface wettability, the study also delves into surface topographies and chemical compositions, providing an in-depth understanding of surface modifications induced by oxygen plasma treatment. While the oxygen plasma treatment predominantly removes material and induces nanoscaled structures on Teflon AF1600, oxygen plasma results in the creation of a stiff oxide layer on the PDMS surface. Buckling structures are formed on PDMS surfaces due to the mechanical mismatch between the stiff oxide layer and soft bulk PDMS. The surface properties (i.e. wetting properties and topographies) of plasma-treated Teflon AF1600 exhibit high dependency on applied plasma energy, while high correlations between wetting properties, topographies, and key parameters such as dilution ratio, film thickness, and plasma treatment time are revealed for PDMS. In conclusion, this comprehensive study not only contributes to the fundamental understanding of surface properties for Teflon AF1600 and PDMS, but also introduces a novel modeling approach that can be applied to analyze and predict wetting behaviors under varying conditions, thus paving the way for advancements in both surface science and future device design.

Contents

Chapter 1

Introduction

Contents

1.1 Motivation and objectives

Surface science is an important branch of science and is a vital field dealing with both fundamental and application-oriented research questions, thus stimulating interdisciplinary activities across traditional disciplines, such as chemistry, physics, and engineering. Among many others, a fundamental understanding of surface properties and its wetting phenomenon is not only crucial to science itself but also of tremendous value to many applications, such as printing and coating, microfluidic devices, fluid transportation, etc.[1]

When a water droplet is placed onto a solid surface, a sessile drop takes form, and the contact angle (CA) that emerges between the solid and water droplet is used to describe the wetting property. The concept of an “appropriate angle of contact”, as articulated by Young in his seminal essay “III. An essay on the cohesion of fluids” dating back to 1804, laid a foundational cornerstone for understanding solid/liquid systems [2]. The CA is described as the result of a mechanical equilibrium by interface tensions at the contact triple line. In characterizing the wetting properties of a surface, two CAs are essential: advancing and receding CAs. The difference between both CAs is termed contact angle hysteresis (CAH), commonly observed in natural materials with a range of $10 - 20°$ [1, 3–8]. While the concept of CA may seem straightforward, its measurement and interpretation pose intricate challenges. Accurate and reliable procedures for CA determination and interpretation demand thorough investigations into surface preparation, droplet application methods, measurement techniques, data analysis, and the time interval following droplet application [1, 9]. The literature classifies CA measurements into two groups: static and dynamic CA measurements [1, 9]. However, the term “dynamic CA measurements” might be misleading, as it seemingly suggests that the CA is influenced by dynamic effects and, therefore, cannot serve as a characteristic quantity for surface wetting properties. Upon closer examination, the terms static and dynamic indicate whether the triple line (solid-liquid-air contact line) is in motion. The dynamic condition of the triple line does not necessarily imply that the CA itself is dynamic. As pointed out by Strobel and Lyons in their study entitled “An essay on contact angle measurements”, dynamic effects on measured advancing and receding CAs are significant only at high capillary numbers, where the measured values become dependent on the triple line's speed [5]. The capillary number, a dimensionless characteristic parameter, quantifies the ratio of viscous forces to surface tension[10–12]. Despite the potential influence of dynamic effects on CA, dynamic CA measurements are still commonly employed in literature to characterize surface wetting properties without explicitly assessing the impact of dynamic effects. In contrast to dynamic CA measurements, static CA measurements are often performed by measuring a single CA through droplet application on a solid surface. As previously mentioned, natural materials often exhibit a CA hysteresis of 10-20°. A static CA, being any value between the two limits of advancing and receding CAs, is insufficient to fully characterize the wetting properties of a surface.

Beyond the complexity of the CA measurement methods, the root causes of CA hysteresis remain obscure. Several variables thought to influence CAs and hysteresis, such as surface roughness, chemical heterogeneity, and liquid-surface interactions like adsorption, are enumerated in literature[9, 13–16]. The widely used Wenzel and Cassie equations[17, 18] attempt to depict CAs on roughed and structured surfaces by integrating surface area fractions. However, these equations necessitate specific structural insights and mandate a homogeneous evaluation of surface structures or roughness, a requirement that is not always readily accessible, measurable, or determinable. Furthermore, ongoing discussions and debates in the scientific literature emphasize the uncertainty about when it is appropriate to use these equations, underscoring the need for a clearer and more broadly applicable way to describe CAs on roughed and structured surfaces and how liquids interact with these surfaces[9, 19–22].

In addition to the listed factors contributing to CAH, a comprehensive understanding of surface wetting properties necessitates the consideration of a crucial factor – temperature, as the interface tensions as well as a possible contribution of CAH – adsorption are temperature dependent. While some researchers have experimentally investigated the impact of temperature on the CAs[16, 23–30], the lack of well-defined CA measurement procedures has resulted in limited availability of reference values from these studies.

Beyond the fundamental understanding of wetting properties and CA, there is a growing interest in literature surrounding the manipulation and modification of these properties. On one front, it becomes essential to alter surface wettability for subsequent fabrication endeavors. For instance, hydrophobic surfaces are frequently subjected to exposure to air or oxygen plasma to improve their wettability, facilitating subsequent surface engineering, layer deposition, or alternatively, to reduce wettability for self-cleaning purposes[31–40]. On another front, electrowetting-on-dielectric (EWOD) provides another opportunity of controlling surface wettability, enabling e.g. transport and shape manipulation of micro-droplets in various application fields[41–48]. In the classical EWOD setup, an electrically conductive liquid droplet is placed on a plane and dielectric layer, which is arranged above an electrode. The CA between the electrolyte and the dielectric surface is determined by the interface tensions at the triple line, as well as the electric energy stored within the solid dielectric layer. Like the CAs on pristine surfaces, the CAs responsive to applied voltage are also influenced by surface roughness, chemical heterogeneity, liquid-solid molecular interactions, and of course, temperature. Several studies have explored a range of factors influencing CAs in electrowetting (EW), including variations in surface roughness, water adsorption, and the direction of triple-line movement (whether advancing or receding conditions) [49–57]. However, there is limited research addressing the impact of temperature on EW-CAs, making it an area that requires further exploration.

In summary, the complexity surrounding CA determination, influenced by various factors such as measurement methods (both static and dynamic), surface conditions (including roughness), and environmental variables (such as temperature), along with the absence of descriptive models for CAs and wetting phenomena under these conditions, has garnered significant attention in the literature. Further investigations are imperative to enhance our comprehension of wetting phenomena, particularly for practical and reliable applications such as EW.

This work aims to present precise methods for measuring CA and to develop a descriptive model for CA interpretations concerning temperature. Additionally, it includes an investigation into the response of EW on both experimentally ideal and structured surfaces. The goal is to provide a deeper understanding of surface wetting properties, considering not only contributions from surface roughness and structures but also the influence of temperature and related factors.

1.2 Outline and conceptual framework

Following this introduction, Chapter 2 will delve into the fundamentals that underpin this work. It will encompass key concepts such as wettability, surface tensions, equations outlining the characterization of CAs on both smooth and rough surfaces, as well as the discussion on the misconceptions and misunderstandings in this research field. Additionally, the chapter will introduce the materials employed in the investigation of surface wettability and the EW effect.

Expanding upon these fundamental principles, Chapter 3 will provide a comprehensive overview of the facilities and instruments utilized for surface film deposition, sample fabrication, and post-treatment. The subsequent chapter, Chapter 4, will elucidate the various characterization methodologies employed for assessing surface properties.

The subsequent four chapters will delve into the results and analyses derived from the conducted experiments. In Chapter 5, an in-depth exploration of the modification of Young's equation will be presented, encapsulating the incorporation of temperature's impact on CAs. Moving to Chapter 6, the focus will be the plasma treatment to change the surface properties and the extension of the modified Young's equation to the changed surfaces. Chapter 7 will then apply this modified equation to expound upon the EW-CAs. A distinct phenomenon in surface wettability, known as surface wettability recovery, will be explicated in Chapter 8.

Chapter 9 will serve as a synthesis, encapsulating the findings of this thesis and proposing directions for further experimental and theoretical exploration. To provide clarity, an appendix will feature a comprehensive list of all symbols employed, followed by an exhaustive list of references.

Chapter 2

Fundamentals and state of the art

Contents

2.1 Surface, wetting, and contact angle

The study of surfaces is a crucial area of science, particularly in understanding the fundamental interactions between liquids and solid surfaces, to understand and predict wetting phenomena for different combinations of liquids and solids. The wettability of a liquid, typically water, spreading on a solid surface [58–60], is often evaluated with contact angle (CA) measurements. CA is described as the result of a mechanical equilibrium by interface tensions at the contact triple line by Young in his legendary publication entitled “III. An essay on the cohesion of fluids”. The term triple line comes from the fact that it is a line or boundary where the three phases, involving the solid surface, the liquid droplet, and the surrounding air, intersect. The famous Young’s equation is written as[2]

$$\gamma_{\mathrm{la}} \cdot \cos\theta_{\mathrm{Y}} = \gamma_{\mathrm{sa}} - \gamma_{\mathrm{la}}, \tag{2.1}$$

where γ is the interface tensions, while the subscripts s, l, a represent solid, liquid and surrounding air, respectively. Sketches of the force equilibrium at the triple line are shown in Fig. 2.1 Depending on the value of CA, the wettability of a surface is classified as either hydrophilic or hydrophobic. Surfaces with a CA of less than 90° are hydrophilic and exhibit high wettability, as shown in Fig.2.1(left), while surfaces with a CA larger than 90 ° are considered hydrophobic and exhibit low wettability, as shown in Fig.2.1(right). Typically, the CA of water on a flat hydrophobic solid is in the range of 100 to 120 °[61]. Moreover, surface roughening[62–64] and structuring[65–68] can increase the CA to values higher than 150°, resulting in a surface wettability known as superhydrophobicity[61]. This extremely low wettability has numerous applications in self-cleaning surfaces and microfluidic devices [61], and is introduced in Chapter 2.1.2 in detail.

The concept of CA is simple, but its interpretation is not. Achieving impeccable and reliable measurement procedures for CA determination and interpretation requires investigation of surface preparation and conditioning, measurement procedures and techniques, and data analysis. These factors have been studied for many years to ensure accurate and reliable CA measurements and interpretations[1], and are introduced in the following subsections.

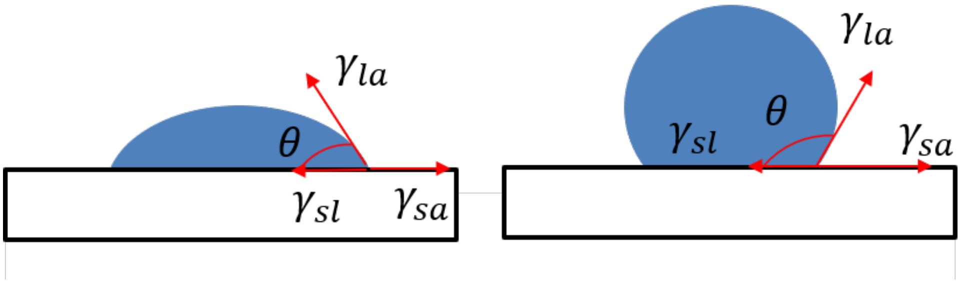

Fig. 2.1: Schematic illustration of the force equilibrium at the triple line when a drop sitting on a hydrophilic (left) and hydrophobic (right) solid surface.

2.1.1 Contact angles and hysteresis

Young's equation (Eq.2.1) implies a unique CA, which is described by the interface tensions of a liquid-solid-air system [69, 70]. In practice, however, the observed CA is often in a range between a maximum and a minimum value, which corresponds to the advancing and receding CA, respectively. A schematic illustration of the advancing and receding CAs is shown in Fig. 2.2. The difference between these two CAs is known as the contact angle hysteresis (CAH) [1, 5],

$$\mathrm{CAH} = \theta_{\mathrm{adv}} - \theta_{\mathrm{rec}}. \tag{2.2}$$

CAH is a characteristic property of the surface[4, 5]. A typical CAH observed on surfaces in the real world is 10°–20° or more[71]. The exact reason behind the CAH is not fully understood. There are several factors that are believed to contribute to the advancing and receding CAs and consequently the CAH, such as surface roughness, chemical heterogeneity, interface interactions, and others[4, 7, 13–15, 72–76]. However, the specific impacts and magnitudes of these factors are not understood in detail and are still under investigation.

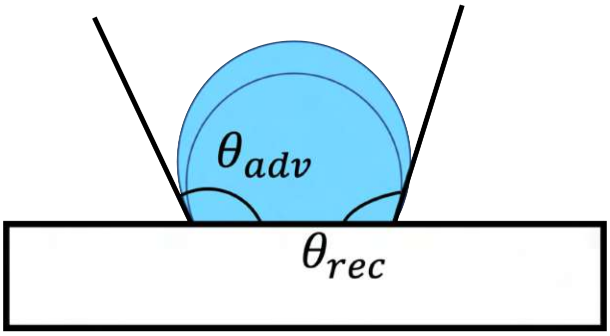

Fig. 2.2: Schematic illustration of advancing and receding CA.

2.1.2 Wetting on rough surfaces

When taking surface roughness and surface topography into account, there are two possible states to describe the wetting behavior: the Wenzel state and the Cassie-Baxter state. A sketch of both states is shown in Fig. 2.3. In the Wenzel state, the liquid is in full contact with the rough solid surface, resulting in an increased surface area of contact[18]. The CA in the Wenzel state can be described by the equation:

$$\cos(\theta_{\mathrm{W}}) = f_{\mathrm{r}} \cdot \cos(\theta_{\mathrm{Y}}), \tag{2.3}$$

where the f_{r} is the surface roughness factor and is written as

$$f_{\mathrm{r}} = \frac{\text{actual surface area}}{\text{projected surface area}}. \tag{2.4}$$

The Wenzel state describes that the surface roughness increases the hydrophobicity if the surface is hydrophobic i.e. CA>90°. In contrast, roughness enhances the wettability of hydrophilic surfaces i.e. CA<90°.

The Cassie-Baxter state originally provides an extended analysis of CAs for wetting behavior on porous surfaces[17]. It describes the formation of air pockets and the resulting composite interface between the liquid and solid phases when a liquid wets a porous surface. It is also applied to describe the CA on structured surfaces as air is trapped within the surface structures. The CA in Cassie-Baxter state is described by

$$\cos(\theta_{\mathrm{c}}) = f_{\mathrm{solid}} \cdot \cos(\theta_{\mathrm{Y}}) - (1 - f_{\mathrm{solid}}), \tag{2.5}$$

where f_{solid} is the area fraction of the partially liquid-wetted solid area, and the $1 - f_{\mathrm{solid}}$ is the fraction of the non-wetted area (air-pockets).

However, these methods of describing the CA on rough and structured surfaces by area fractions are arguable. The roughness factor f_{r} in the Wenzel equation, as well as the area fraction f_{solid} in the Cassie-Baxter equation, are related to the contact area (solid-liquid area), while the CA describes the mechanical equilibrium at the contact triple line according to Young's equation (Eq. 2.1). Gao and McCarthy conducted straightforward experiments to demonstrate that the CA is determined by the contact triple line and is irrelevant to the overall contact area. They used locally structured solid surfaces and conducted CA

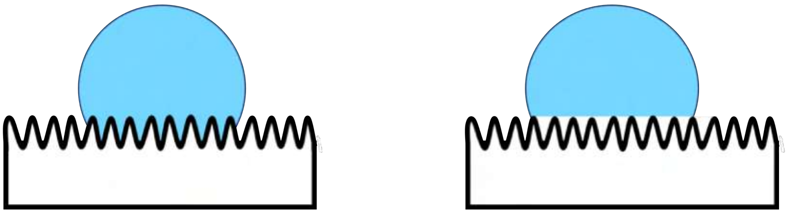

Fig. 2.3: Sketch of the Wenzel (left) and Cassie-Baxter state (right). In the Wenzel state, the solid is in complete contact with the liquid droplet, while in the Cassie-Baxter state, the solid surface is partially wetted by the liquid droplet, and local air-liquid contacts are presented in the global liquid-solid interface.

measurements when the triple line was at various positions. These positions included the contact triple line located on the structured area, the contact triple line extending beyond the structured area, and on the flat and unstructured surface area. The results revealed that the CA is determined by the solid-liquid contact at the triple line and is independent of the overall solid-liquid contact area. The surface structures presented in Gao and McCarthy work exhibited inhomogeneity of the surface structures. This inhomogeneity, particularly the difference between area fraction at the triple line and that across the overall contact area, has sparked discussions regarding the appropriate circumstances for using an area fraction approach[9, 19–22]. According to Nosonovsky, the Wenzel and Cassie equations are valid only for uniformly rough surfaces, while McHale suggested that local roughness and area fractions, instead of global roughness, should be considered. Details of these discussions can be viewed in the original papers cited in this work. A more comprehensive understanding of the CA characterization on rough and structured surfaces can be found in a review paper by Parvate, Dixit, and Chattopadhyay[78].

To summarize, while the Wenzel and Cassie-Baxter equations are commonly used to describe contact angles on rough and structured surfaces, their validity and scope of application are still under debate.

2.1.3 Contact angle measurements

In most CA measurements, a sessile drop is formed on a horizontal solid surface by dispersing the liquid through a microsyringe[1]. After the drop establishes its shape equilibrium, the profile of the sessile drop is captured and then applied for the CA analysis. Several mathematical methods have been applied to calculate the CAs at the triple line, including the tangential method, circle method[79, 80], ellipse method[81, 82], and Young-Laplace method[83–85].

As previously mentioned, natural surfaces exhibit CAH. To fully characterize the surface wettability, it is essential to measure both the advancing and receding CAs. These measurements require the establishment of the advancing and receding triple line and are achieved by increasing the drop volume or tilting the sample plate through the sessile drop method[1, 4–8], as shown in Figs. 2.4 and 2.5. The former involves an embedded needle to increase and decrease the drop volume at a low volume change rate[86–89]. However, the needle has an effect on the drop shape and can also break the axisymmetric of the drop shape, especially when measuring the receding CA, as shown in Fig. 2.4(right).

Consequently, the embedded needle causes errors and uncertainty in the drop shape analysis as well as the CA determination. To eliminate this effect, Erbil et al. reported a method for receding CA measurement on polymers by exploiting the evaporation of a liquid droplet[6]. The volume decrease due to evaporation establishes a receding triple line state without a needle. Consequently, a reliable receding CA is measured.

The latter CA measurement method, namely the tilting plate method, involves the CA measurement when a sessile drop is deposited on the surface and then the solid sample with the applied sessile drop is tilted at a very low speed[1, 5, 12, 90], so that no dynamic effects are involved in this measurement. When the drop starts sliding, the CA measured in the lead and trail edge of the droplet represents the advancing and receding CA, as shown in Fig. 2.5.

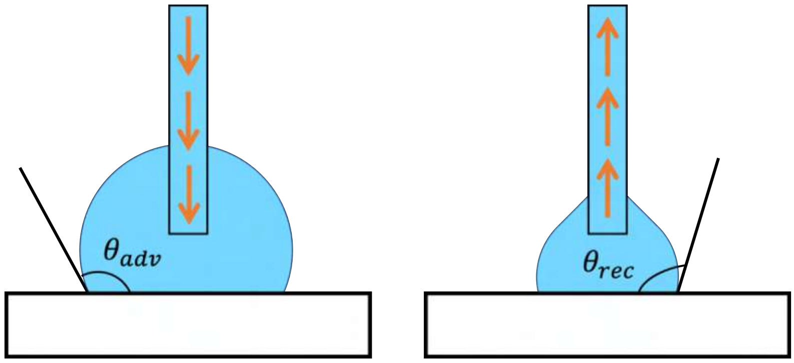

Fig. 2.4: Schematic showing of the needle-embedded sessile drop method for measuring advancing (left) and receding (right) CAs.

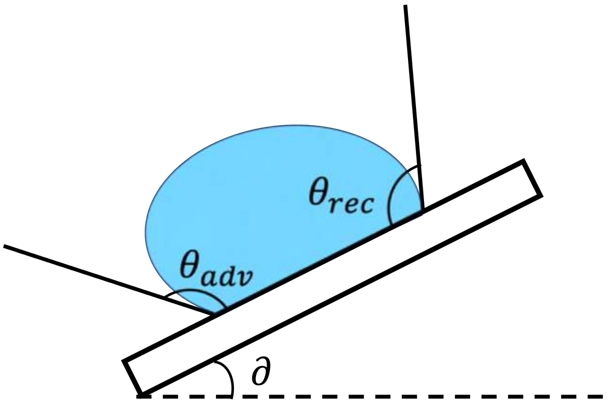

Fig. 2.5: Schematic showing of the tilting plate method for measuring advancing and receding CA.

An alternative CA measurement method in addition to the sessile drop method is the so-called captive bubble method. Instead of depositing a liquid on a solid surface to form a sessile drop, an air bubble is generated and injected into a tank containing the test liquid, where the test solid surface is positioned on top of the test liquid[1, 91].The advancing and receding CA can be therefore measured by decreasing and increasing the bubble volume, as shown in Fig. 2.6. An advantage of this method is that the temperature can be easily controlled. However, the solid surface is in contact with the test liquid for a long time period, which can cause aging and swelling of the surface material. In addition, the surface is firstly in contact with liquid and then covered by the air bubble, so that this air-solid interface can also experience liquid adsorption.

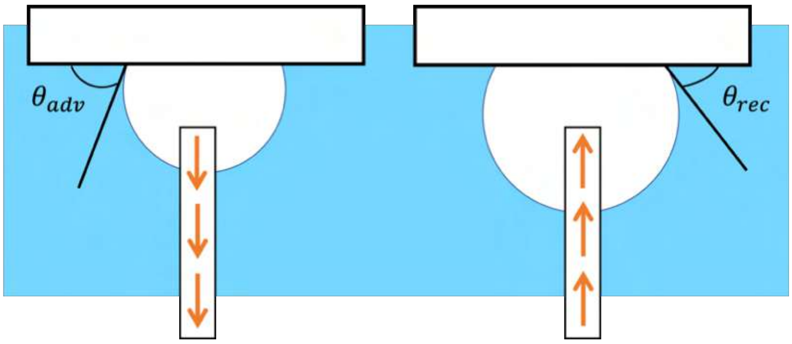

Fig. 2.6: Schematic showing of the captive bubble method for measuring advancing (left) and receding CA (right).

In addition to the above-mentioned methods, which rely on the optical analysis of the drop or bubble shape, the Wilhelmy plate method, which measures the surface forces through a tensiometer, also provides an indirect determination of CAs[1, 4, 92]. Instead of a droplet or bubble sitting on a surface, a vertical solid plate is lowered into a bath or pulled out of it at a very low rate to measure the advancing and receding CAs, respectively. Again, the low rate condition must be fulfilled to exclude any dynamic effects from the plate movement. A schematic showing of the Wilhelmy plate method is shown in Fig. 2.7. The solid surface is fabricated in a plate form with well-defined width w and thickness d. The force balance on the surface is described by the wetting force ($F_{wetting}$), gravity (F_g), buoyance force ($F_{buoyance}$), and the force measured by the tensiometer ($F_{tensiometer}$):

$$F_{wetting} + F_g = F_{buoyance} + F_{tensiometer}. \tag{2.6}$$

The wetting force $F_{wetting}$ is written as

$$F_{wetting} = (2w + 2d) \cdot \gamma_{\mathrm{la}} \cdot \cos\theta. \tag{2.7}$$

Based on Eqs. 2.6 and 2.7, the advancing and receding CAs are calculated. In comparison to the sessile drop-based methods, the Wilhelmy plate method relies on force measurement, eliminating errors due to the presence of a needle and due to a complex drop shape analysis. However, it does require precise sample dimensions (width w and thickness d), as well as a flat, rigid, and homogeneous surface in order to obtain accurate results[1].

In the literature, the measurement of advancing and receding CAs, which involves the movement of the triple line, is commonly referred to as dynamic CA measurements[1]. The term “dynamic” may imply that the CA is influenced by dynamic effects during the measurement process. The question that arises is whether the dynamic effect should be taken into account and whether the measured CAs significantly differ from the static CAs, which are obtained when the triple line is stationary. Strobel and Lyons suggested in their study entitled “An essay on contact angle measurements” that, only at high capillary

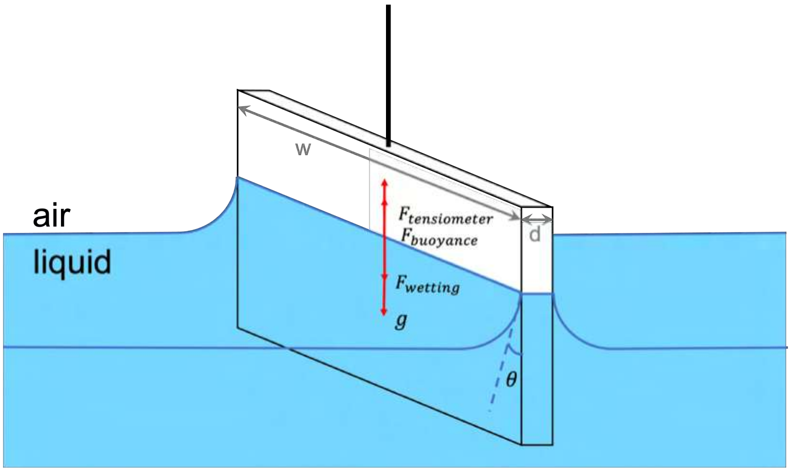

Fig. 2.7: Schematic showing of the Wilhelmy plate method for CA measurement.

numbers, the advancing and receding CAs suffer from dynamic effects and are dependent on the speed of triple line [5]. The capillary number (Ca) is a dimensionless characteristic number that quantifies the ratio between the viscous forces compared to surface tension forces and is defined as

$$Ca = \mu \cdot v/\gamma, \tag{2.8}$$

where μ is the dynamic viscosity of the liquid, v is the characteristic velocity of the liquid, and γ is the liquid surface tension.

As emphasized in the earlier description of CA measurement methods, the CAs are obtained at a slow rate of the liquid front (triple line) movement to ensure a significantly smaller capillary number than the critical value of Ca (10^{-5}), so that the measured CAs are supposed to be independent of the speed of triple line movement, and are considered equivalent to the CA measured immediately after the motion of the triple line comes to a halt, which is referred to as the static CA[5, 10–12]. The term “dynamic” in the context of “dynamic CA measurement” specifically refers to the movement of the triple line during the measurement process, and does not imply that the CA is significantly affected by dynamic effects or that it should be treated as a dynamic CA. On the contrary, it is crucial to minimize the rate of triple line movement during the measurement, since the CAs are intended to represent the surface wettability and should not be influenced by the specific measurement setup and dynamics of the triple line movement. It is indeed unfortunate that the term “dynamic CA measurement” has led to misunderstandings and a potential oversight in controlling the triple line movement during CA measurements.

2.1.4 Effect of temperature on wettability

In addition to surface roughness, the temperature is another crucial factor that significantly influences contact angles (CAs) and plays a vital role in applications requiring precise CA determination, such as adaptable liquid lenses based on the electrowetting (EW) effect[44, 45, 47, 93–95]. Temperature can affect the interface tensions, molecule interactions, and the wetting behavior of the liquid on the solid surface, thereby influencing the observed CAs. Despite its interest and importance, only a few studies have investigated the temperature dependency of CA. In the following, the related works regarding the temperature dependency of CA are briefly introduced.

2.1.4.1 Theoretical models

In the literature, there are semi-empirical models to describe the temperature dependency of the CAs of non-polar liquids.

Diaz, Savage, and Cerro developed a model to predict the variation of CAs with temperature under the consideration that an adsorbed film is presented next to the static air/liquid/solid triple line[96]. Fig. 2.8 shows the simplified profile of the liquid wedge in contact with an adsorbed film. They used the modified Young's equation, in which the CA is described by the specific interface free energies[3], instead of the interface tensions in the original Young's equation. The specific interface free energy, G, is evaluated by its bulk value σ and the disjointing pressure Π,

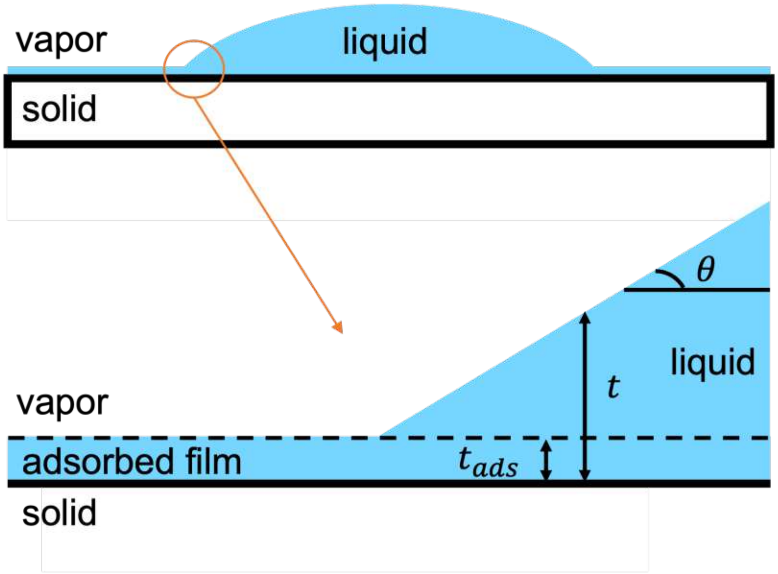

Fig. 2.8: Sketch of a non-polar liquid drop on a solid surface (top) and the simplified profile of the liquid-air interface in contact with the adsorbed film (bottom).

$$G(t,\theta) = \sigma + \int_t^{\infty} \Pi(t,\theta)dt. \tag{2.9}$$

θ is the CA and t is the local liquid film thickness, as shown in Fig. 2.8.

The shape of the air-liquid interface is described by the Young-Laplace equation,

$$2H\sigma + (p_l - p_a) = 0 \tag{2.10}$$

where H is the mean curvature of the liquid-air interface and p_l and p_a are the internal pressure in liquid and air.

Near the contact triple line, the interface free energies are dependent on the thickness of the liquid film and can be expressed as:

$$G(t,\theta) \cdot 2H = -\Pi(t,\theta) - (p_l - p_a). \tag{2.11}$$

Plugging Eq. 2.9 into Eq. 2.11, the fully-augmented Young-Lippmann equation, which describes the interface free energy close to the triple line, is written as[3]

$$-G(t,\theta)\cdot 2H = \frac{dG(t,\theta)}{dt}. \tag{2.12}$$

The mean curvature of the interface, $2H$, is expressed as[3]

$$2H = -\frac{d\cos\theta}{dh}. \tag{2.13}$$

Combining Eqs. 2.12 and 2.13, and taking the two boundary conditions into consideration:

(1) at a point outside the molecular region, the disjointing pressure is zero and the interface free energy G equals the bulk value σ. The CA is θ, as shown in Fig. 2.8;

(2) at the horizontal adsorbed film, where $\cos\theta_{ads} = 1$.

the resulting equation that describes the relationship between the CA, θ, and disjoining pressure, $\Pi(t,\theta)$, is

$$\cos\theta = 1 + \ln\left[1 + \frac{1}{\sigma}\int_{t_{ads}}^{\infty}\Pi(t,\theta)dt\right]. \tag{2.14}$$

A simplification of the liquid-air interface at the triple line is applied, that is, the triple line is in a wedge shape from the adsorbed liquid film to the droplet shape with a CA of θ, as shown in Fig. 2.8. Taking the Van der Waals's interaction between the molecules within this simplified geometry into account, the analytical expression for the disjointing pressure at a point on the liquid-air interface is

$$\Pi(t,\theta) = -\frac{A_{LL}-A_{SL}}{6\pi(t)^3} - \frac{A_{LL}}{12\pi(t-t_{ads})^3}\cdot\left[-1+\frac{3}{2}\cos(\theta)-\frac{1}{2}\cos^3(\theta)\right], \tag{2.15}$$

where A_{LL} and A_{SL} are the Hamaker constants for the molecular interactions of liquid-liquid and solid-liquid, respectively[3]. Combining Eqs. 2.14 and 2.15, one can obtain:

$$\cos\theta = 1 + \ln\left[1 - \frac{A_{LL}-A_{SL}}{12\pi\sigma(t_{ad}-l)} - \frac{A_{LL}}{12\pi\sigma l^2}\cdot(-\frac{1}{2}+\frac{3}{4}\cos\theta-\frac{1}{4}\cos^3\theta)\right]. \tag{2.16}$$

where l is the cutoff length of estimating the strength of binary molecular interactions. As the Hamaker constants, as well as σ, are temperature dependent, the Eq. 2.16 is able to describe the CA of non-polar liquid at different temperatures.

Diaz, Savage, and Cerro investigated the CAs of linear hydrocarbons (octane, decane, dodecane, tetradecane) on polytetrafluoroethylene (PTFE), and the results revealed a declining trend of CA with temperature and verified their proposed model[96]. In addition, Sullivan also applied a Van der Waals model for the gas adsorption on a solid surface to describe CAs[97]. More details of these models can be found in the original papers cited in this work and a recent review paper from Song and Fan[98] .

In summary, these models rely on the thermodynamic interpretation of the CA and consider the molecular interactions between the non-polar liquid, air, and solid phases at the triple line. By doing so, they provide a more comprehensive understanding of the temperature dependency of CAs. However, it is important to note that these models are generally applicable to non-polar liquids, as they primarily take Van der Waals's interactions between liquid and solid molecules into account. On the other hand, models describing the temperature-dependent CA of polar liquids, like water, are still lacking in the literature. The complex molecular interactions and polarity of water pose challenges in developing accurate theoretical models for its temperature-dependent CA behavior. Additionally, the presence of an adsorbed liquid film at the solid-air interface is a prerequisite for the application of these models. The forming of this adsorbed film requires liquid-solid CA smaller than 90 °. Furthermore, there is an ongoing debate regarding the interpretation of CA in terms of surface tension versus surface energy. Although mathematically interchangeable, the use of surface energy instead of surface tension to describe the CA is still a topic of discussion. More discussions between surface tension and surface energy are presented in Chapter 2.2.

2.1.4.2 Experimental studies

Although there is no widely accepted model for the temperature-dependent CA of water on different surfaces, several experimental studies have been conducted to investigate water CAs at various temperatures. For example, in a study by Ponter and Boyes (1971), the water CA on PTFE was investigated under reduced pressure conditions ranging from 2.3 to 101.2 kPa, with corresponding saturation temperatures from 20 to 100 °C[23]. The experiments were conducted in the air with saturated water vapor, and the CAs were measured using the sessile drop method. The results indicated that the CA remained constant at 105 °. However, as previously discussed (Chapter 2.1.1), CA hysteresis is commonly observed on natural materials, so the measured static CA after applying a droplet on a solid surface varies between the advancing and receding CA. Thus, a single static CA measurement without stating the triple line condition (advancing or receding) is insufficient to characterize surface wettability. Therefore, in the following, only the thorough investigations of the temperature-dependent wettability, which encompass clear measurements of advancing and/or receding CA, are discussed and presented in detail.

Tadros, Hu, and Adamson (1974) investigated the water CA on a stearic acid surface using the captive bubble method over a temperature range of 5 to 70 °C[24]. The results revealed an increase in the advancing contact angle from 76 ° to around 98 ° as the temperature increased from 5 to 50 °C, followed by no further change temperature up to 70 °C.

Using the tilting plate method, Phillips and Riddiford (1965) measured the advancing and receding CAs of water on a siliconed glass surface at three different temperatures (4, 22, and 75 °C) in a water-saturated environment[25]. The results showed that the advancing and receding CAs remained unchanged at values of 105 ° and 76 °, respectively.

Similarly, Jones and Adamson (1968) investigated the CAs of water on naphthalene using the captive bubble method at temperatures ranging from 10 to 78 °C[26]. Their results showed a decrease in both advancing and receding CAs, from 92 to 82 ° and from 89 to 81 °, respectively.

The investigation of water CAs in response to temperature changes has revealed diverse behaviors, including increasing, decreasing, or remaining constant trends. These variations are influenced by several factors, such as the characteristics of the solid materials, the specific temperature range under consideration, and the wettability of the surface (hydrophobic or hydrophilic), among others.

It's worth mentioning that there are more recent studies investigating the temperature dependency of water CA on various surfaces, such as stainless steel (Hayashi et al., 2004; Song, Zeng, and Fan, 2020)[27, 28], metallic surfaces (Hirose et al., 2006)[29], graphite, silicon, and gold (Osborne, 2009), PTFE and nanoparticle-coated surfaces (Weisensee et al.,2015)[16]. However, these studies rely on single static CA measurements and are not sufficient to reveal the wetting properties. Interested readers can refer to the original papers for more information.

2.2 Surface tension and surface energy

The surface energy (J/m^2) and surface tension (N/m) are mathematically equivalent and consequently are used interchangeably in the literature. Commonly, one uses the term surface tension when speaking of liquids, while the term surface or interface energy is used when it comes to solid. However, it is worthwhile to point out that surface tension and surface energy are different quantities[1, 9, 99], as surface tension is a tensor whereas surface energy is a non-directional scalar property of a surface. The quantities employed in Young's equation for describing CA, are surface tensions[2], as the CA is determined by the mechanical equilibrium at the triple line.

2.2.1 Measurement of liquid surface tension

The surface tension of the liquid is measured and determined using the pendant drop method, which is a widely used technique in material science, biotechnology, and food science, where surface tensions are crucial parameters. The pendant drop method involves suspending a drop of liquid from the end of a needle, as shown in Fig. 2.9, and analyzing its shape using optical techniques[100, 101]. The shape of the pendant drop is studied

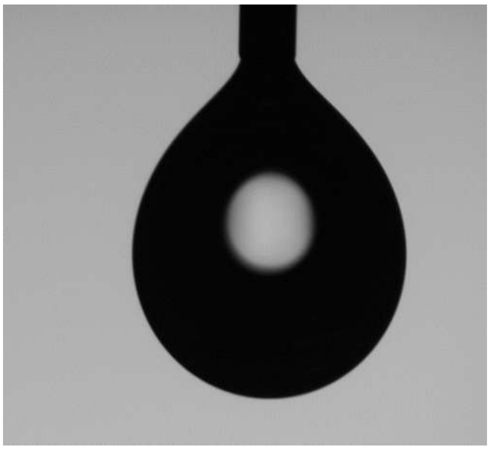

Fig. 2.9: A pendant drop.

based on the Young-Laplace equation, which describes the pressure difference across an interface between two static fluids and is given by:

$$\Delta p = p_{inner} - p_{outer} = \gamma \cdot (\frac{1}{R_1} + \frac{1}{R_2}), \tag{2.17}$$

where R_1 and R_2 are the principal radii of curvature. When there are no external forces acting on the droplet, the droplet is in a spherical shape. In reality, droplets are affected by gravitational force, which results in an additional pressure difference along the z-axis of the droplet. The pressure difference is

$$\Delta p_{hyd} = \Delta \rho g h, \tag{2.18}$$

where $\Delta\rho$ is the density difference between the two static fluids, and h is the droplet height. As a consequence, the droplet deforms from the ideal spherical shape to a characteristic “pear shape”. A numerical method is used to analyze the shape during the pendant droplet measuring process. Finally, the surface tension is calculated based on the droplet shape, see Eq. 2.17[8, 101].

2.2.2 Measurement of solid surface tension

The solid surface tension and surface energy can be measured and determined by three basic approaches: (1) Zisman method[102], (2) surface tension component methods (Fowkes method[103–106], van Oss, Chaudhury and Good model[107–109]), and (3) equation of state[69, 110–112]. The Zisman method is an empirical approach based on the correlation between $\cos(\theta)$ of various test liquids on a solid surface versus the surface tensions of the test liquids (alkanes). The $\cos(\theta)$ is fitted as a linear function and the critical solid surface tension, γ_C, is determined by extrapolating the linear function to $\cos\theta = 1$. The Zisman approach is limited to surfaces with low surface tensions, where the Van der Waals interaction is dominant and the correlation can be assumed as linear[102].

The surface tension component methods assume that the surface tension consists of different components, which address different intermolecular interactions individually[1]. The Fowkes method originally considers the dispersion interaction only and then is extended to include polar and H-bonding interactions[103–106]. The van Oss, Chaudhury, and Good (vOCG) model assumes that the surface tension consists of an apolar component γ^{LW} and a polar component γ^{AB}. The former represents the Van der Waals interactions and is composed of dispersion and dipole-dipole interactions. The latter includes hydrogen-bonding interactions[107–109].

The method of the equation of state is totally different from the surface tension component methods described above. The equation of state method assumes that the surface tension γ_{sl} only depends on the surface tension of liquid-air (γ_{la}) and solid-air (γ_{sa})[1, 70, 80, 110], and the surface tension is obtained by curve fitting with CAs and adjustable parameters. More details about these methods can be found in their original papers as well as a review book[1].

However, the surface tension component methods and equation of states approaches are semi-empirical, and based on many assumptions[1]. One of them is the reversible work of adhesion assumption proposed by Dupré[113]. Hypothetically, when a solid surface and a liquid surface are brought together, the free energy change per unit area (work of adhesion $W_{\mathrm{sl}}^{\mathrm{ad}}$) is equal to the interface energy of the newly formed interface, γ_{sl}, subtracted by the surface energy of the precursor surfaces, γ_{la} and γ_{sa},

$$-W_{\mathrm{sl}}^{\mathrm{ad}} = \gamma_{\mathrm{sl}} - \gamma_{\mathrm{la}} - \gamma_{\mathrm{sa}}. \tag{2.19}$$

The validity of this assumption is questionable as the molecules of a solid material are immobile during any interface interaction[1]. In addition, the determination of surface tension requires the measurement of CA. As discussed above, the CA always varies in a range between the advancing and receding CA and is affected by non-material factors, like roughness and surrounding temperature. Therefore, instead of using surface tension, the advancing and receding CA measurement is more straightforward and meaningful to describe the wettability of a solid surface.

2.3 Hydrophobic materials

Hydrophobicity describes the physical characteristic of a molecule that appears to be repelled by water. Hydrophobic materials, which are typically non-polar in nature, exhibit a low affinity for water, leading to their water-repellent properties[114]. The most applied hydrophobic materials are polymers, including acrylics, epoxies, polyethylene (PE), polystyrene (PS), polyvinyl chloride (PVC), perfluoroalkoxy alkanes (PFA), polytetrafluoroethylene (PTFE), polydimethylsiloxane (PDMS), and several commercial copolymers such as Teflon AF groups as well as Cytop. Here, the Teflon AF and PDMS and including their excellent properties and application potential are introduced in detail in the next subsections.

2.3.1 Teflon AF

Teflon AF is an amorphous fluoropolymer group based on a copolymer of 4,5-difluoro-2,2-bis-(trifluoromethyl)-1,3-dioxol (PDD) and tetrafluoroethylene (TFE). The chemical formula of Teflon AF is shown in Fig. 2.10. Depending on the m and n values (mole %) there are a few Teflon AF products. Teflon AF1600 (65 % PDD), is one of them and has

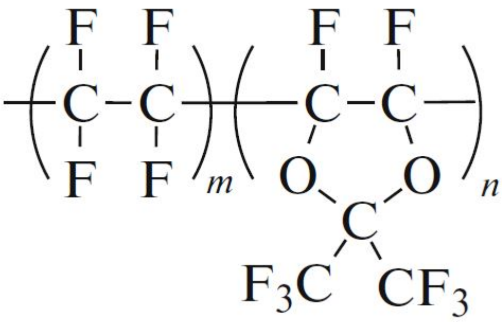

Fig. 2.10: Chemical formula of Teflon AF group. m and n represent the mole percentage of TFE and PDD. For Teflon AF1600, m, and n are 65% and 35%, respectively.

extraordinary properties like other conventional hydrophobic fluoropolymers (PTFE, PFA, etc.), such as high-temperature stability[115], outstanding chemical resistance, and low surface energy[116], widely used in application fields requiring a high WCA, e.g. EW-based variable focus liquid lens[45, 52] etc.

In comparison to conventional fluoropolymers, which are mostly semi-crystalline or highly crystalline and only soluble in high-boiling solvents at a temperature near their melting point[117], Teflon AF material is amorphous and soluble in some fluorinert solvents at room temperature. The former property makes it optically transparent, and the latter allows for fabricating thin film through various methods, such as spin coating, dip coating, and spray coating[117, 118].

2.3.2 PDMS

Polydimethylsiloxane (PDMS) is an elastomer containing carbon and silicon. The chemical form is shown in Fig. 2.11. PDMS exhibits excellent thermal and chemical stability, optical transparency, and biocompatibility. In comparison to Teflon AF materials, PDMS is extremely cost-efficient (Teflon AF1600 powder: 465 €/g; PDMS liquid + cross-link agent: 0.24 €/g), so it becomes an alternative for applications where a hydrophobic surface is required.

In addition to these excellent properties, PDMS also offers possibilities for efficient modification of its mechanical properties[119–121], wetting characteristics[122–124], and surface topography[119, 121, 125]. These unique properties continuously attract considerable interest and attention, leading to various application areas such as surface engineering[126–129], optical gratings[130, 131], microfluidics[132–134], stretchable electronics[135], biochips[128, 133, 136].

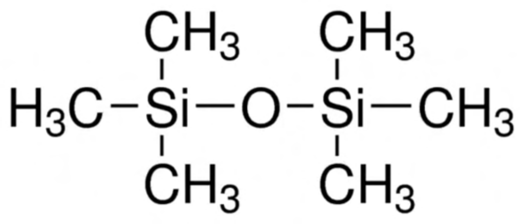

$$\begin{array}{ccccc} & \mathrm{CH_3} & & \mathrm{CH_3} & \\ & | & & | & \\ \mathrm{H_3C}- & \mathrm{Si} & -\mathrm{O}- & \mathrm{Si} & -\mathrm{CH_3} \\ & | & & | & \\ & \mathrm{CH_3} & & \mathrm{CH_3} & \end{array}$$

Fig. 2.11: Chemical formula of PDMS.

2.4 Electrowetting on dielectric

Electrowetting-on-dielectrics (EWOD) is one of the most widespread techniques for manipulating the drop shape as well as the CA between an electrolyte droplet and a dielectric surface[93]. In the classical EWOD experimental setup, an electrically conductive liquid droplet is placed on a plane and dielectric layer, which is arranged above an electrode. Under static equilibrium conditions, the liquid maintains a constant electric potential. Specifically, the base surface of the liquid represents an equipotential surface, which corresponds to an electrode with a defined area. The CA between the electrolyte and the dielectric surface is affected by the interface tensions at the triple line, as well as the electric energy stored within the solid dielectric layer. When performing EW on a dielectric layer (EW-CA), the CA is described by the famous Young-Lippmann (YL) equation,

$$\cos\theta = \cos\theta_{\mathrm{Y}} + \frac{c \cdot U^2}{2 \cdot \gamma_{\mathrm{la}}} \quad , \tag{2.20}$$

where c (F/m^2) is the specific capacitance of the dielectric layer. θ_{Y} is the CA described by Young's equation [2], as the result of the force equilibrium of surface tensions at the triple line. There are several approaches to deriving the YL equation, like a thermodynamic and electrochemical approach, an energy minimization method, and an electromechanical approach. More details about these different approaches and EW theory can be viewed in a review paper "Electrowetting: from basics to applications"[42].

Due to the low energy consumption and easy control and manipulation of liquid droplets, EWOD has been widely used in applications, for example, generating transporting, and mixing small droplets in microfluidic devices [41–43], adjustable liquid lenses [43–48], etc.

However, the EW-CA is also affected by material and ambient-related factors, such as surface roughness [13], chemical inhomogeneity [14], and water adsorption [15, 137], resulting in a CA hysteresis. Several works have been published to explore the EW response on materials with high CA hysteresis [49–51]. In these studies, the EW response was investigated for increasing and decreasing droplet volume to achieve the advancing and receding triple line conditions and the corresponding CAs. Compared to the theoretical predictions (Eq. 2.20), not only the advancing and receding EW-CAs have been observed [49, 50], but also a completely different behavior of the triple line has appeared, namely stick-slip behavior [51]. The stick-slip refers to the alternate movement of the triple line: sticking to a position and slipping over the surface.

Furthermore, the CA is affected by temperature [52, 137], especially in the liquid lens application field, since the interface tensions, as well as the CA hysteresis, are temperature-dependent [137, 138]. Therefore, a deeper understanding of the EW-CA dependence on temperature is required to enable a precise prediction and control of the wetting properties.

2.5 Summary

The wetting property of a surface, typically characterized by the CA between a liquid and a solid surface, is a fundamental property of surfaces and interfaces. Despite the long-standing Young's equation that provides insights into the relationship between surface/interface tensions and CA at the triple line, there have been numerous misunderstandings and misuses in this field.

Firstly, there is often confusion between the concepts of surface tension and surface energy. While these terms can be mathematically interchangeable, they represent different quantities.

Secondly, there is ongoing debate regarding whether the CA is influenced by the contact area or the contact triple line. This question arises from the well-known Wenzel and Cassie-Baxter equations, which expand upon Young's equation by incorporating contact area-based concepts, such as area ratios, to describe the CA on rough and structured surfaces.

Another common misunderstanding pertains to CA measurements. It is essential to characterize surface wettability by measuring both the advancing and receding CAs since natural surfaces exhibit a CAH of at least 10-20°. Moreover, advancing and receding CA measurements involve the movement of the triple line. Consequently, these CAs are often referred to as “dynamic CA measurements” in the literature. However, it is important to note that CAs obtained at a low triple line movement rate are not significantly influenced by dynamic effects and should not be treated as dynamic CAs.

In addition to the above-mentioned issues in the literature, a notable gap exists in providing a comprehensive explanation of CAH. To address this gap, there is a growing demand for in-depth investigations into the determination and quantification of CAH.

Furthermore, the temperature has a significant impact on contact angle (CA) determination. There have been only a limited number of studies that have investigated the temperature dependency of CA, both from a theoretical and experimental aspect. While a few models have been proposed to describe the temperature dependence of CA for non-polar liquids, the theoretical investigation of CA for polar liquids like water is relatively rare due to the complexity of molecular interactions involved. Experimental studies have focused on examining the temperature dependency of water CA on various solid surfaces. These investigations have revealed diverse trends in CA with temperature, depending on factors such as the nature of the solid materials (hydrophobic or hydrophilic), the specific experimental setup, and the temperature range being investigated. To gain a better understanding of the surface wetting properties and to broaden their practical applications, there is a pressing need for both theoretical and experimental investigations into the effects of temperature on CAs. By unraveling the temperature effects on CAs, researchers can advance the field of interface science, and optimize processes in e.g. EW-based applications.

Chapter 3

Fabrication details

Contents

Parts of this Chapter have been published in “Temperature Dependence of Water Contact Angle on Teflon AF1600”[137], “Temperature-dependent electrowetting behavior on Teflon AF1600”[139] and “Surface properties of µm and sub-µm polydimethylsiloxane thin films after oxygen plasma treatment”[140]

3.1 Microfabrication techniques

Microfabrication techniques are essential in the development of microelectronics, microsensors, microactuators, and other microsystems. These techniques are used to fabricate homogeneous thin films, create micro-, and nano-structures, modify surface properties, etc. The most commonly used microfabrication techniques are photolithography, film deposition, etching, and bonding[141, 142].

Photolithography is a process to create patterns on a substrate, typically a silicon (Si) wafer. The process involves ultraviolet (UV) exposure through a photomask to project a desired pattern to the UV-sensitive photoresist[143, 144]. The process initiates with the wafer undergoing spin-coating to apply a thin layer of photoresist. Subsequently, a photomask, comprising optically opaque and transparent regions housing the desired pattern, is positioned over the wafer. During exposure, UV light penetrates the transparent regions of the photomask, inducing a chemical change in the photoresist. This alteration renders the photoresist either more or less soluble in a developer solution, dictated by the type of photoresist employed: positive or negative. After exposure, the wafer undergoes development, where the developer solution selectively removes either the exposed or unexposed sections of the photoresist. The resulting patterned photoresist acts as a protective mask in subsequent wet or dry etching processes.

In contrast, the lift-off process, another advanced patterning technique, utilizes the photoresist layer as a sacrificial rather than a protective layer, as depicted in Fig. 3.1. This method involves creating an inverse pattern by selectively removing the photoresist from areas where material deposition is intended. A negative photoresist is employed for this purpose. Following the standard photolithography process for negative photoresist pattern formation, a uniform layer of the target material is deposited across the entire substrate. The subsequent removal of the sacrificial layer, achieved through etching, leaves behind the desired material pattern on the substrate.

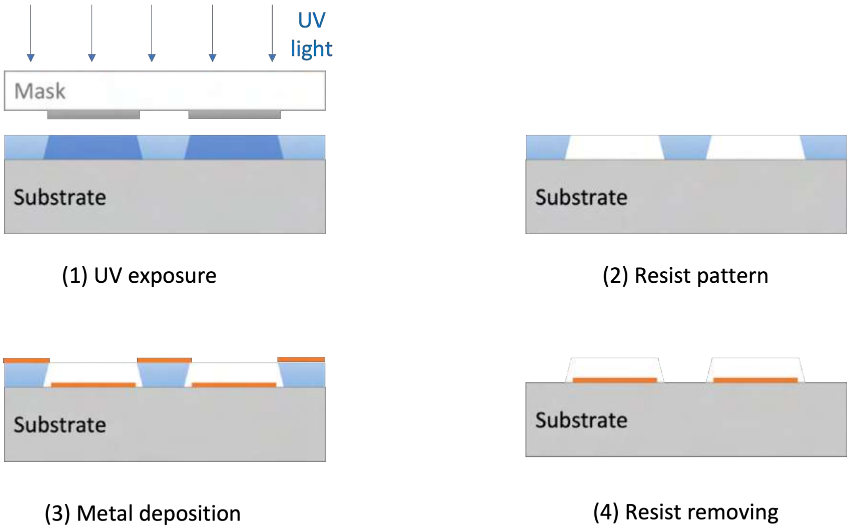

Fig. 3.1: Lift-off process. Typical steps of a lift-off process for patterning a metallic thin film.

The etching process involves the removal of material from a substrate using either chemical or physical means or a combination of both. An effective etching process requires high selectivity and in most cases prefers an anisotropic process. The high selectivity describes a complete etching of the top layer of a multilayer structure without damaging the underlayer. Anisotropic etching refers to different etching rates in different directions, whereas isotropic etching removes material uniformly in all directions. The etching process is basically divided into wet and dry etching depending on how the material is removed. Wet etching refers to the eroding of material by compounds dissolved in an etching solution and can offer a high selectivity. In this work, for instance, the buffered hydrofluoric acid (87.5 wt% NH_4F, 12.5 wt% HF) is applied to remove silicon dioxide. Differing from wet etching, the material is eroded by the atoms or molecules of a fully or partially ionized gas during a dry etching process[143]. The material to be etched during the dry etching process is either carried out by the kinetic energy of the particles from the gas, or by a chemical reaction between the material and the gas. For the realization of micro-structures with steep sidewalls and a high aspect ratio in silicon, the deep reactive ion etching (DRIE), also known as the Bosch process, is applied. The DRIE process achieves high selectivity through alternating cycles of Si etching and the formation of a passivation layer [143].

Film deposition, as its name suggests, refers to the formation of typically amorphous or polycrystalline films up to a thickness of micrometers films on the surface of a substrate. Chemical vapor deposition (CVD) and physical vapor deposition (PVD), are among the most important deposition technologies in microelectronics and microsystems technology[145]. The main difference between the two methods lies in the way that the raw material or precursor is supplied. In CVD processes, the precursor is supplied to the deposition chamber in a gas phase or from a vaporized liquid source, whereas in PVD processes, it is supplied from a solid target. During a CVD process, one or more volatile precursors are introduced and allowed to react and/or decompose on the surface of the substrate to produce the desired deposit. CVD is practiced in a variety of formats depending on how the chemical reactions are initiated. The main one related to this work is plasma-enhanced CVD (PECVD). PVD is a process in which the material is vaporized and deposited onto a substrate by evaporation or sputtering. In the evaporation method, the source material is evaporated in a vacuum chamber and condenses back to the solid state on the substrate. There are several energy sources that are applied to evaporate the material. The main methods related to this work are the thermal and electron beam methods. In the sputtering process, high-energy particles are used to bombard the solid material, causing atoms or molecules to be emitted and deposited onto the target substrate[146].

In addition to CVD and PVD, spin coating is also applied in this work for the deposition of uniform thin films of polymers. Spin coating is a process wherein the coating material, typically a solution, is applied or deposited onto a substrate. The substrate is rotated at a desired speed to spread the liquid material uniformly across the surface. The coated substrate is then placed on a hot plate or in an oven to allow the solvent to evaporate, leaving behind a thin and uniform film. The thickness of the coated film depends on the number of rotations per minute (rpm) and the time of rotation[147]. More details of the microsystem technology can be found elsewhere[143, 145, 146, 148, 149].

In the following, the processes of fabricating samples and microstructures investigated in this thesis are presented.

3.2 Fabrication of hydrophobic thin films

3.2.1 Teflon AF1600 films

Spin-coating is applied to achieve nano- and micro-meter thick Teflon AF1600 layers. The spin coater applied in this work is Süß MicroTec. The fabrication process has been investigated to achieve homogeneous and pinholes-free surfaces.

Firstly, various solutions by weight of Teflon AF1600 (DuPont Co. USA) in fluorinert FC-40 solvent (3M Company), 1, 2, 4 %, were prepared and stirred at 50 °C for four days. The solution was additionally filtered by a PTFE membrane with a pore size of 5 µm to remove undissolved or aggregated particles. Afterward, the solution was placed in a vacuum for a few minutes to remove air bubbles, which were trapped in the solution or created by the filtration process.

Due to its high hydrophobicity, it is difficult to achieve adhesion of Teflon AF1600 to silicon substrates. To address this, a titanium (Ti) primer was applied to the wafer to enhance adhesion. The spin-coating process for the Ti primer was carried out at 4000 rpm for 1 min, followed by heating the primer-coated wafer at 120 °C for 2 min. Next, the primer-coated wafer was spin-coated with the solution of Teflon AF1600 at various speeds (1000 − 4000 rpm) and times (60 − 120 s) to achieve different thicknesses. The coated wafers were then subjected to a two-step baking process on a hotplate, involving temperatures of 175 °C and 165 °C for durations of 10 min and 5 min, respectively. This baking process ensured a homogenous and pinhole-free surface. Details are presented in Chapter 5.2.

The resulting thickness of the Teflon AF1600 film was determined by measuring the step height with a profilometer (Dektak) and the thickness results are shown in Fig. 3.2. Furthermore, the thickness results showed that the film thickness increases from ≈ 180 nm to ≈ 440 nm with a 2 % solution at spin coating conditions of 1000 rpm and 1 min when the Ti primer was applied.

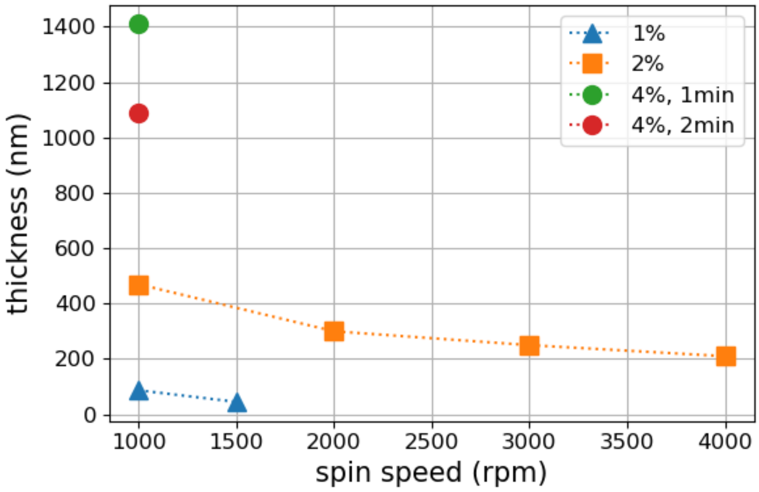

Fig. 3.2: The thickness of Teflon AF1600 film with different solutions concentrations and spin speeds. The inserted lines serve as a guide to the eyes.

In summary, this work achieved various Teflon AF1600 thicknesses with a homogenous surface by controlling the film thickness through adjustments in solution concentration and spin coating parameters. Additionally, the application of Ti-primer to enhance the adhesion of Teflon AF1600, along with the subsequent appropriate baking steps, contributed to the successful outcomes.

3.2.2 PDMS films

PDMS is an elastomer and the fabrication process is different in comparison to Teflon AF1600. PDMS elastomer (Sylgrad 184 kit, Dow Corning) was prepared by mixing the prepolymer base and curing agent with a 10:1 ratio by weight and followed by a degassing process in a vacuum desiccator for 30 min. To achieve a micrometer and submicrometer thickness, the PDMS mixture was diluted with non-aqueous liquid, n-heptane, at various dilution ratios. The next step involved spin-coating the diluted PDMS mixture onto a silicon die with the dimension of 20×20 mm^2 in a nitrogen environment, using various spin speeds and times[133, 150]. Subsequently, the samples were cross-linked for 2 h at 100 °C in a cleanroom environment. The fabrication parameters and the resulting thickness are shown in Table. 3.1 For a better overview, the PDMS films with a thickness of 3.5 µm and 0.85 µm are named M, m, and N, n, respectively. The lowercase letter represents the sample fabricated from a more diluted PDMS. For instance, M is non-diluted, while m is diluted by a dilution ratio of 5:1.

sample	dilution ratio [wt%]	thickness [µm]	spin speed[rpm]	spin time [s]
M	0:1	3.5 ± 0.10	7000	150
m	5:1	3.5 ± 0.10	500	30
N	5:1	0.86 ± 0.13	6000	120
n	9:1	0.85 ± 0.13	500	30

Tab. 3.1: The dilution ratio, fabrication parameter, and the resulting thickness of the PDMS samples.

3.3 Surface modification

Two primary methods, namely plasma treatment and photolithographic micro-structuring, were utilized in this work to modify the surface properties, including surface topography and wetting characteristics. The plasma treatment was conducted by an STS 320 RIE plasma etching system using a radio frequency (RF) power supply at 13.56 MHz. The photolithographic micro-structuring was conducted using a mask aligner of Süß MA06 generation 4 and followed by DRIE using Oxford plasma lab 100.

In the following, the details of those two methods are introduced.

3.3.1 Plasma treatment

Plasma treatment is one of the most wide-used methods to modify surface properties, especially in the polymer-related application field[33–37]. The effects of plasma treatment parameters on the surface properties of Teflon AF1600 were investigated through oxygen and nitrogen plasma treatment. The plasma chamber was first evacuated to a pressure of 12 mTorr and purged with nitrogen gas to initiate the process. The oxygen plasma treatment was conducted under various conditions, including chamber pressure ranging from 20 to 40 mTorr, oxygen gas flow rate from 20 to 40 sccm, plasma power from 50 to 400 W, and treatment time from 10 to 140 s. After the plasma treatment, the chamber was purged with nitrogen gas for 1 minute and the pressure was then pumped down to 12 mTorr for 2 minutes. The parameter details are given in Chapter 6.

Unlike the oxygen plasma treatment on the other polymers, where the plasma removes surface material and creates nano-structures on the surface[33–37], the oxygen plasma does not remove material but reacts with the PDMS surface and generates a thin silica layer. The thickness of the silica layer is a function of the oxidation time[151–153]. In this work, oxygen plasma treatment was performed on PDMS at different durations of 5, 15, and 30 seconds, with a constant chamber pressure, oxygen gas flow rate, and power of 120 mTorr, 20 sccm, and 100 W, respectively.

3.3.2 Photolithographic micro-structuring

In contrast to plasma treatment, which modifies the surface topography randomly, as well as alters the chemical composition, leading to changes in surface wettability, photolithography can be employed to create regularly arranged micro-structures on the surface. These micro-structures lead to incomplete contact between the liquid and the surface, known as Cassie state (details see Chapter 2.1.2), ultimately resulting in the establishment of superhydrophobicity.

Because of the weak adhesion between Teflon AF1600 and photoresist, and the limited thickness of the Teflon AF1600 layer that can be fabricated, micro-structuring was performed on a Si substrate using DRIE in the Oxford Plasma Lab 100. Then, a layer of Teflon AF1600 with a thickness of 100 nm was deposited on the structured Si substrate using the spin-coating method, as detailed in Chapter 3.2.1. Two different arrangements of structured pillars were used, namely cubic and hexagonal, as shown in Figure 3.3. The diameter of the pillar ranges from 1 to 20 µm. The pitch ranges from 2 to 40 µm. The resulting ratio of solid surface to the projected surface, f_{solid}, ranges from 0.1 to 0.4. Details can be seen in Chapter 6.3.

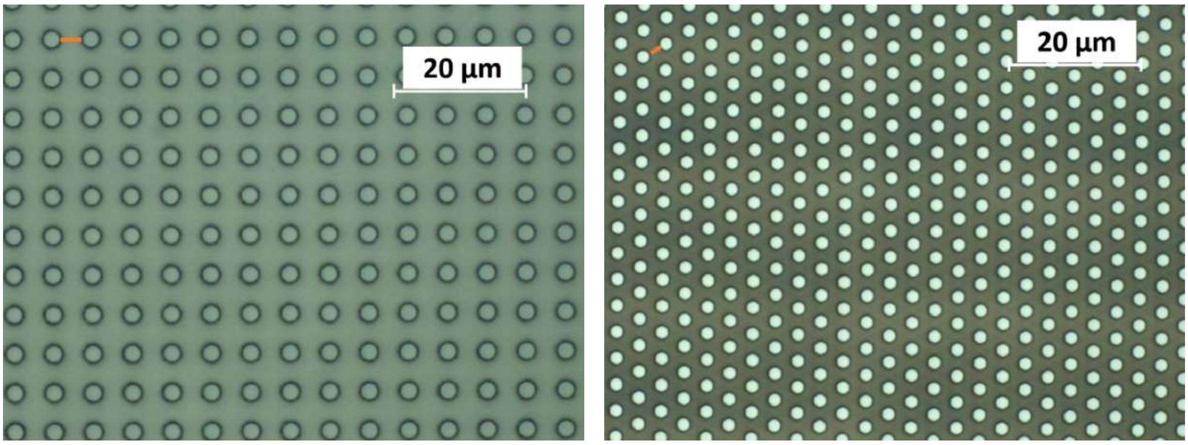

(a) cubic (b) hexagonal

Fig. 3.3: Optical micrograph of different arrangements of the pillar: cubic(left) and hexagonal (right). The orange line represents the distance between pillars.

3.4 Fabrication of samples for EWOD performance

To create samples for EWOD, the conductive Si (0.015–0.025 Ω cm) wafer was chosen as a substrate. The conductive Si wafer is firstly cleaned with buffered hydrofluoric acid

(87.5 % NH_4F, 12.5 % HF) for 2 min to remove the native oxide. On one side of the Si wafer, 50 and 150 nm thick titanium (Ti) and gold (Au) layers were deposited using electron-beam and thermal evaporation through the instrument Balzers BAK550. The objective of incorporating a Ti layer between the Au layer and the conductive wafer is to enhance the adhesion of the Au layer and form an ohmic contact with the wafer. On the other side of the Si wafer, either a single layer or a multilayer was deposited as the dielectric.

In the following, the details of creating the dielectric layer are introduced.

3.4.1 Single layer

In this work, a Teflon AF1600 layer with a thickness of 1.09 µm is used as a single layer to evaluate the EWOD performance. The fabrication process is introduced in Chapter 3.2.1.

3.4.2 Multilayer

The dielectric layer in a multilayer structure consists of Teflon AF1600 and another insulator layer, such as SiO_2 and/or Si_3N_4. Initially, SiO_2 and Si_3N_4 layers were deposited by PECVD for the first trial. However, the EW test revealed that dielectric breakdown occurred at a much lower voltage than expected. For example, in the multilayer structure comprising 250 nm SiO_2 and 80 nm Teflon AF1600, the breakdown occurred at only 20 V, which was significantly lower than the expected applied voltage of 50 V required to achieve a CA of 80 ° (details can be found in Chapter 7). Consequently, Si wafers with a 250 nm thermal SiO_2 layer were used as the substrate, and a second dielectric layer, Teflon AF1600, was deposited to achieve the desired multilayer structure.

3.5 Fabrication of capacitor-type test structures

To accurately assess the EWOD performance, it is necessary to determine and measure the capacitance of the dielectric layer. According to the Teflon AF1600 datasheet[116], the dielectric coefficient is 1.93 and the dielectric strength is 21 kW/mm. To verify the electrical properties, capacitor-type structures were created. A typical example of a Teflon AF1600-based capacitor structure is shown in Fig. 3.4, and the fabrication process is described in a point-by-point manner in the following:

- A substrate of a 4-inch Si wafer was utilized, onto which a layer of chromium (Cr) and gold (Au) with thicknesses of 50 and 150 nm, respectively, were deposited using electron-beam and thermal evaporation. The formation of the bottom electrode was carried out through a lift-off process.
- A 1.09 µm thick Teflon AF1600 was spin-coated on the wafer, the details are described in Chapter 3.2.1.
- 100 nm Au was thermally deposited on top of the Teflon AF1600 layer. The wet etching process was applied to pattern the top electrode.

- The dielectric layer, Teflon AF1600, was structured by a dry etching process in oxygen plasma with the top electrode as a mask.

The capacitor-type test structures have a circular capacitance area and the diameter ranges from 1 to 8 mm. The capacitance and the dielectric property of Teflon AF1600 were measured and calculated. The results are presented in Chapter 7.3.1.

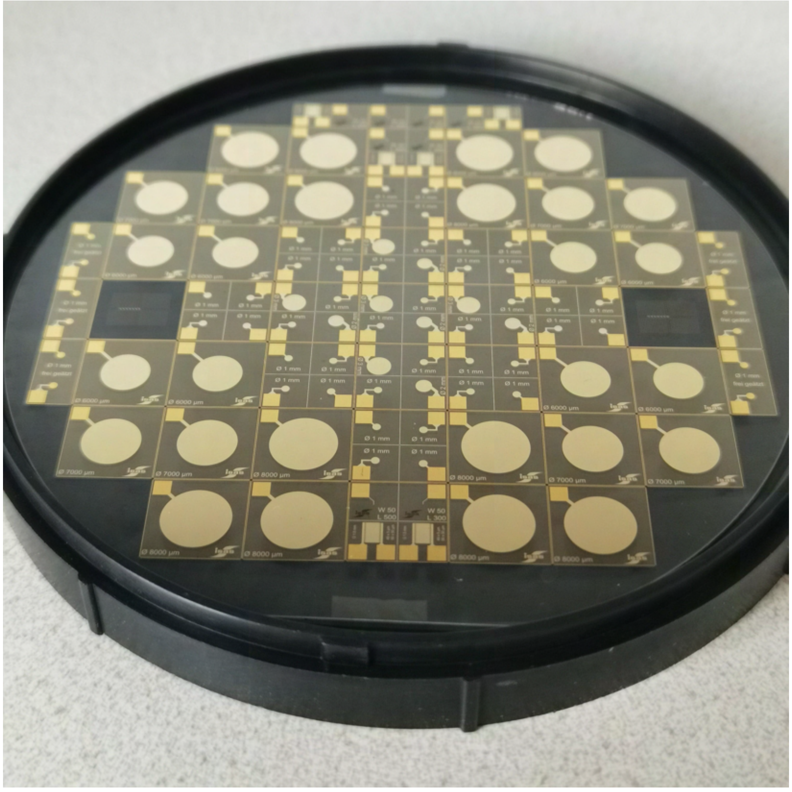

Fig. 3.4: Capacitor-type test structure on a 4-inch Si wafer.

3.6 Summary

In summary, microfabrication techniques, including photolithography, etching, and deposition methods are presented in this chapter. The details of fabrication processes for the layers and samples applied in this work are presented:

- homogeneous and pinhole-free Teflon AF1600 films with different thicknesses by improving and controlling the fabrication process.
- PDMS films with different thicknesses by dissolving the PDMS elastomer and adjusting the fabrication process.
- Modification surface properties by plasma treatment and photolithographic microstructuring.

- EWOD samples: thermally deposited Au-layer as the bottom electrode, 1.09 µm thick TeflonAF as the dielectric layer.
- Capacitor-type test structures: photolithographic patterned electrode-dielectric-electrode structure is applied for the capacitance determination.

Chapter 4

Characterisation techniques and measurement methods

Contents

Parts of this Chapter have been published in “Temperature Dependence of Water Contact Angle on Teflon AF1600”[137], “Temperature-dependent electrowetting behavior on Teflon AF1600”[139] and “Surface properties of µm and sub-µm polydimethylsiloxane thin films after oxygen plasma treatment”[140].

4.1 Liquid surface tension determination

In this work, the surface tension of the liquid is measured and determined using the pendant drop method, which is a widely used technique in material science, biotechnology, and food science.The pendant drop method involves suspending a drop of liquid from the end of a needle, as shown in the left image in Fig. 4.1, and analyzing its shape using optical techniques[100, 101]. More details about the pendant drop method are introduced in Chapter 2.1.3.

The device applied for the pendant drop method is a Krüss Droplet Shape Analyzer (DSA30S), which comprises a high-resolution camera, an illumination system, a two-dimensional automatic dosing system, and a three-dimensional manually adjustable sample placing system. Figure 4.2 displays the DSA30S. Furthermore, the base plate is designed to be temperature-controlled, and more information about this feature is provided in the following section.

4.2 CA measurement set-up and method

In this work, the Krüss DSA30S is utilized for CA measurement. This instrument is capable of performing both the pendant drop and sessile drop methods, as illustrated in Fig.4.1. The pendant drop method is used to measure the liquid surface tension, while the sessile drop method is employed for CA and solid surface tension determination. The images taken by Krüss DSA30S have a resolution of 200 Pixel/mm, and are analyzed for the droplet contour. As a result, Krüss DSA30S provides high measurement resolutions of 0.01° and 0.01 mN/m for CA and surface tension, respectively.

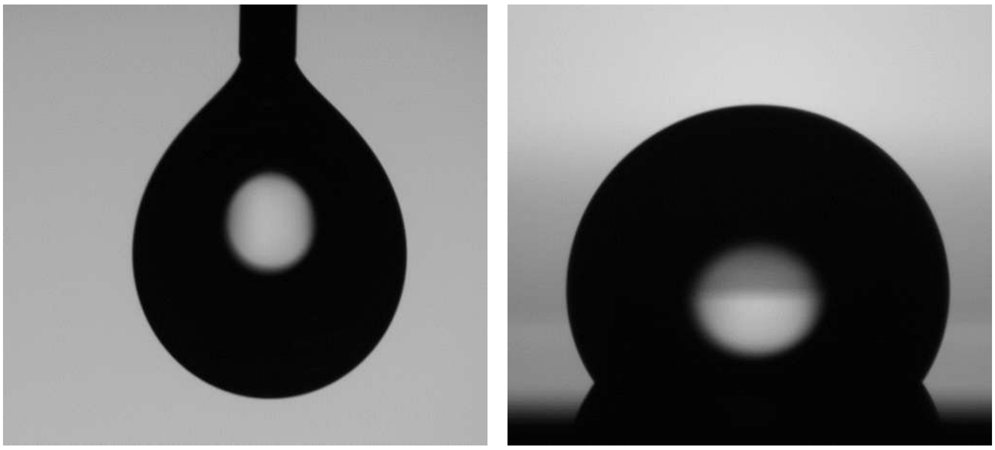

(a) Pendant droplet (b) Sessile droplet

Fig. 4.1: Example of a pendant drop (left) and a sessile drop (right). Picture provided by Krüss DSA30S.

The pendant drop method is introduced in the previous part of Chapters 2.1.3 and 4.1. In the sessile drop method, as shown in Fig. 4.1(right), a static drop is placed on a solid surface instead of being suspended from a dosing needle. Several fit methods, including ellipse fit, circle fit, Young-Laplace fit, and tangent fit method, can be used to analyze the droplet shape[154–157]. Each of these fit methods uses a different principle for droplet shape analysis and CA determination. For example, ellipse fit uses an ellipse to fit the droplet shape, while tangent fit analyzes the angle between the tangent line and the droplet baseline to determine the CA. In this work, CA is determined using the tangent fit method as it focuses on force equilibrium at the triple line, limiting the effect of variations in surface temperature, surface tension, and droplet shape away from the triple line on the CA.

4.2.1 Temperature- and humidity-controlled setup

One of the objectives of this work is to investigate the effect of temperature on surface wetting behavior, specifically on CA. To facilitate this, a costumer-built temperature-controlled unit is integrated into the CA measurement setup. The illustration of the setup is shown in Fig. 4.3[137, 139]. The chamber consists of a solid aluminum (Al) base plate and a massive Al cover, which are both temperature-controlled. The Al base plate is integrated with a platinum resistance thermometer (Pt100), which is connected to a temperature controller (Meerstetter TEC-1091). This ensures precise temperature control at the Al base plate with a resolution of 0.01 °C. The Al cover is designed to be detachable and is equipped with two resistance heaters and a K-type sensor to accurately control its temperature with a resolution of 0.5 °C. The high thermal conductivity of the Al minimizes any temperature gradients in the chamber.

In addition to the temperature control, the Al base plate is equipped with a groove, see Fig. 4.3 B (top view). The groove can be filled with water so that the humidity inside the closed chamber is adjusted to prevent droplets from evaporating. When the chamber temperature is maintained at 20 °C, the rate of evaporation is reduced from 0.16 µL/min to 0.004 µL/min. Therefore, any loss in droplet volume is neglected in this work and the droplet size is considered as constant within the measurement time period.

A small hole, measuring 0.1 mm in diameter, is positioned at the cover's top. This hole serves two purposes: facilitating pressure equalization with the ambient atmosphere and allowing the insertion of both the deposition and the platinum needle. The platinum needle is specifically employed for electrical connection in EWOD experiments.

To conclude, two set-ups are available for CA measurements:

- To enable the measurement of CA with spontaneous droplet volume changes, such as evaporation, the Al cover is not applied, and there is no water in the groove. The temperature at the Al base plate is controlled.
- To perform CA measurements that avoid spontaneous volume changes, such as CA on water-adsorbed surfaces, advancing and receding CA measurements, and EWOD performance, the setup requires the application of the Al cover, filling the groove with water, and precise temperature control of both the Al plate and cover to ensure a homogeneous temperature inside the chamber.

To facilitate future reference to the CA measurement setups, the former is named *Evaporation-Setup*, while the latter is referred to as the *Saturated-Humidity-Setup*.

In the following, the CA evolution during droplet evaporation with *Evaporation-Setup*, and advancing and receding CA measurements with *Saturated-Humidity-Setup* are introduced separately in detail.

4.2.2 CA evolution during droplet evaporation

One of the CA measurements employed in this study involves observing the CA evolution during the droplet evaporation process. To ensure accurate CA results that truly reflect the force equilibrium of the three interface tensions at the triple line while discounting the influence of gravity, strict control is maintained over the droplet size and

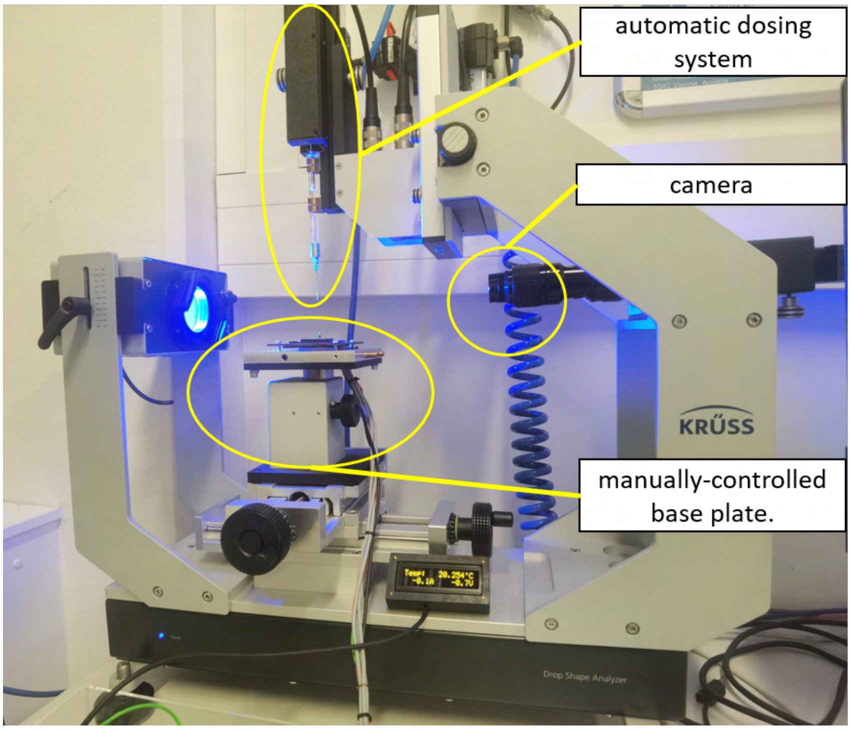

Fig. 4.2: Image of Krüss DSA30S, including illumination system, automatic dosing system, and manually-controlled base plate. The latter is integrated with a platinum resistant thermometer.

volume. Specifically, the droplet size is meticulously regulated to be smaller than the capillary length of the liquid. The capillary length, λ, is a length scaling factor that relates gravitational force and surface tension[5, 158], and is described by[159]:

$$\lambda = \sqrt{\frac{\gamma}{\Delta\rho \cdot g}}, \tag{4.1}$$

where γ is the liquid surface tension, $\Delta\rho$ is the mass density difference between liquid and surrounding liquid or gas, and g is the gravitational acceleration. The shape of a sessile droplet is related to the relationship between the radius of the droplet and the capillary length. When the radius is smaller than the capillary length, the droplet shape is predominantly governed by surface tensions, with the influence of gravity being negligible. In such cases, the droplet is considered to adopt a spherical cap shape, as illustrated in Fig. 4.4. On the other hand, when the droplet has a radius larger than the capillary length, gravitational forces become dominant in determining the droplet shape.

In conclusion, for realizing accurate and reliable CA measurements, the radius of the liquid droplet, which can be calculated through the droplet volume and the CA (through Eqs. 4.2, 4.3, and as shown in Fig. 4.4), is chosen as smaller than the capillary length, λ.

In this study, the primary liquids utilized are de-ionized (DI) water, hexane, and ethylene glycol (EG), with their corresponding capillary lengths at 25 °C presented in Table 4.1. Taking the DI water as an example, the droplet volume of DI water applied is

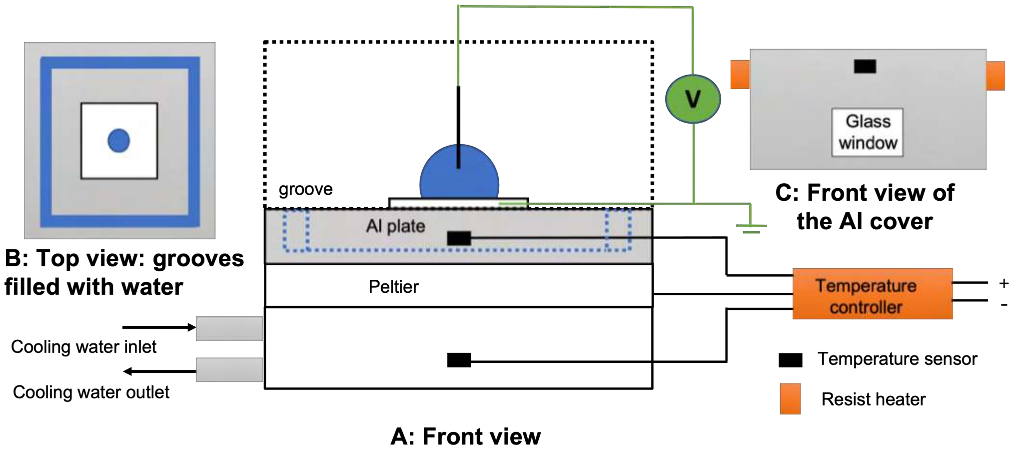

Fig. 4.3: Illustration of the experimental setup [137, 139]. A, front view. B, top view. C, front view of the Al cover with glass windows. A Peltier element under the Al plate, two resistance heaters at the Al cover (black dash line in A, details seen in C), temperature sensors, and a temperature controller guarantee a homogeneous temperature contribution inside the chamber. Two glass windows in the cover (shown in C) are assembled to allow the illumination and observation of droplets. A small opening at the top of the cover allows inserting a needle to deposit the liquid droplet and a 0.1 mm diameter Platinum (Pt) needle for electrical connection. The groove (blue dash line in A, details seen in B) is filled with water to control the humidity and prevent droplet volume loss during experiments.

strictly controlled as smaller than 10 µL, to eliminate the effect of gravitational effect on CAs and to allow reliable CA measurements.

Liquids	γ [mN/m]	ρ [km/m^3]	λ [mm]
DI water	72.8	997	2.7
Hexane	16.1	665	1.6
EG	48.0	1110	2.1

Tab. 4.1: Table of surface tension, mass density, and capillary length of DI water, hexane, and EG at $T = 25°\text{C}$. The liquid surface tensions are measured by the pendant drop method. The mass densities are taken from the datasheet.

4.2.2.1 CA evolution regimes

For droplets with a radius below the capillary length ($\lambda = 2.7$ mm in case of water), the shape of the droplet is approximately calculated as a spherical cap. The dimensions of the droplet are described using the spherical radius R, the height H, the baseline radius r and the CA θ, as shown in Fig. 4.4. The relationship between R, H, r and θ is shown by:

$$R = \frac{r}{\sin\theta} , \quad H = \frac{r}{\sin\theta} \cdot (1 - \cos\theta) . \tag{4.2}$$

The volume of the spherical cap is:

$$V = \frac{\pi}{3} \cdot H^2 \cdot (3 \cdot R - H) = \frac{\pi}{3} \cdot r^3 \cdot \frac{(2 + \cos\theta) \cdot (1 - \cos\theta)^2}{\sin^3\theta} \,, \tag{4.3}$$

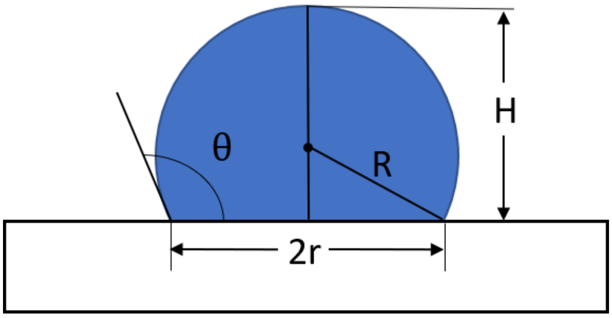

Fig. 4.4: Sketch of a small droplet sitting on a hydrophobic surface, with CA $\theta > 90°$, droplet height H, droplet radius R and contact base radius r.

Commonly two different regimes of CA evolution during droplet evaporation, are characterized: a constant contact radius (CCR), and a constant contact angle regime (CCA)[6, 15, 160–162]. Details can also be seen in Fig. 2. In the CCR regime, the contact radius, namely the contact area stays constant, meanwhile, the CA decreases due to the droplet volume loss by evaporation, see Eq. 4.3. When the CA reaches its receding CA, the droplet evolution transforms from CCR to CCA regime, in which a constant CA, namely the receding CA, is observed. The further droplet volume loss leads to a reduction in contact radius. An example of CA evaluation during droplet evaporation is shown in Fig. 4.5, where typical CCR and CCA regimes are observed.

During droplet evaporation, two distinct values of the CA are characterized: the initial CA, θ_{init}, when placing the droplet on the surface, and the receding or stabilized CA, θ_{rec}, [163, 164]. Two images of representative droplets for θ_{init} and θ_{rec} are shown in Fig. 4.5 as well. For inhomogeneous solid surfaces, an additional regime of stick-slip is observed additionally[15, 165]. One example of the stick-slip regime can be seen in Fig. 5.1 at Chapter 3.2.1 when measuring the CA on a pinhole-presented Teflon AF surface.

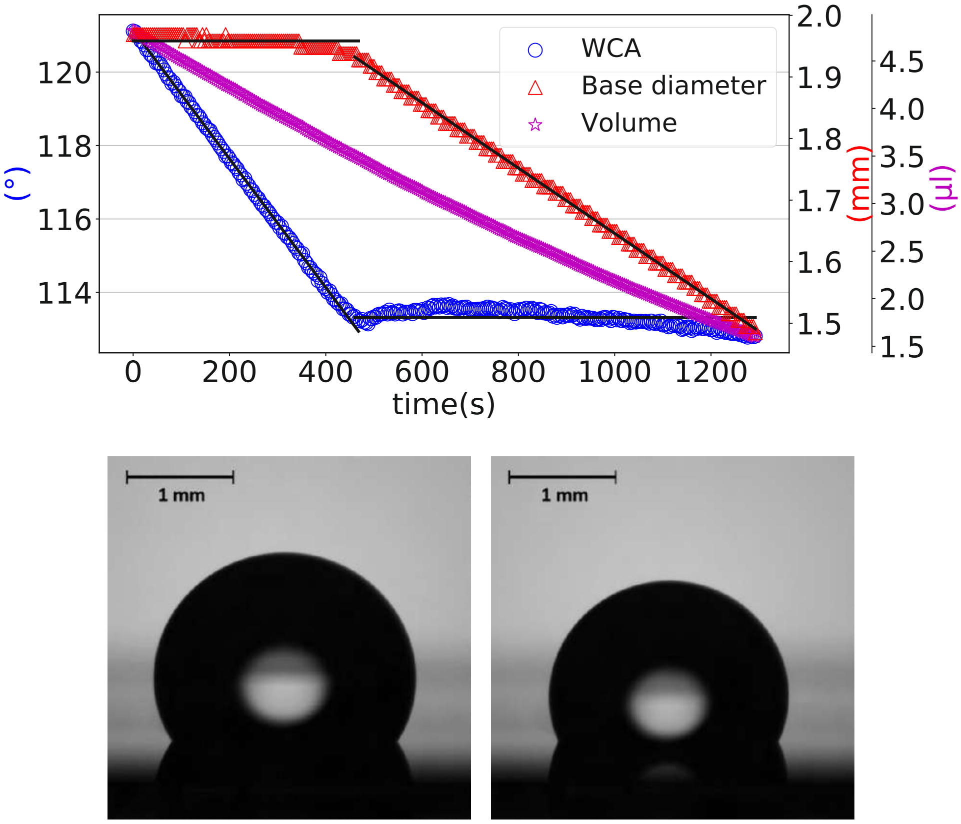

Fig. 4.5: Typical droplet evaluation process. Top: results of water CA (WCA), contact diameter, and droplet volume overtime during the evaporation process at $T = 20$ °C. From 0 to 300 s, the evolution shows a CCR regime, the base diameter stays constant while CA decreases. The CA at $t = 0$ is characterized as the initial CA (θ_{init}). After 300 s, the evolution experiences a CCA regime, in which the CA stays constant and the base diameter reduces. The CA at the CCA regime is characterized as receding CA (θ_{rec}). Bottom: two representative droplet images for θ_{init} at $t = 0$ (left) and θ_{rec} at $t = 500$ s (right), respectively.

4.2.2.2 Advancing and receding CA measurement

As discussed in Chapter 2.1.1, in order to obtain a comprehensive understanding of the wettability of a solid surface, it is necessary to consider both the advancing and receding CAs. These values provide a comprehensive understanding of how the liquid interacts with the surface, including factors such as surface roughness, chemical heterogeneity, and other properties that can influence wetting behavior.

In this work, the advancing and receding CA are measured by the sessile drop method. The receding CA is determined passively through droplet evaporation (*Evaporation-Setup*), as described in the previous section. In contrast, the advancing contact angle (θ_{adv}) is established by increasing the droplet volume and the setup applied is the *Saturated-Humidity-Setup*, see Chapter. 4.2.1. After depositing a droplet onto the surface, the deposition needle remains immersed in the droplet, and is used to increase the droplet volume.

4.3 Electrical characterisation

The EWOD effect enables the manipulation of CA on a solid surface and is dependent on the capacitance of the dielectric layer. In the case of a thin and planar dielectric layer, e.g. the EWOD sample used in this study (Chapter 3.4), the capacitance can be calculated using the following equation:

$$C = \epsilon_0 \cdot \epsilon_r \cdot A/d, \tag{4.4}$$

where $\epsilon = \epsilon_0 \cdot \epsilon_r$ is the permittivity, d is the thickness of the dielectric layer, and A is the electrode area. The electric force acting at the triple line is calculated by

$$F_{\mathrm{el}} = c/2 \cdot U^2, \tag{4.5}$$

where c is the specific capacitance, $c = C/A$. The necessary condition for the geometry $A \gg d^2$ is guaranteed by the sample and the droplet size. The dielectric layer Teflon AF1600 has a thickness of 1.09 µm in this work, while the contact area with the droplet is $5 - 7\ \mathrm{mm}^2$. Additionally, a constant permittivity ϵ is required for a homogeneous, linear, and isotropic dielectric property.

The first characterization was done with an LCR-Meter (Wayne Kerr WK6500). The samples used for the capacitance characterization were fabricated by photolithography and the fabrication process is described in Chapter 3.5. The LCR meters apply sinusoidal AC signals to determine the electrical impedance of the sample with a limited amplitude of 1 V in a wide frequency range. After standard open-short calibration of the measurement setup, excitation voltage levels between 10 mV and 1 V at frequencies between 500 Hz and 100 kHz were applied to the samples for characterisation.

Additionally, the voltage versus current (IV) measurement method is utilized for dielectric property characterization as well. The definition of capacitance, which is given by $C = Q/U$ as the quotient of charge Q and voltage U, leads to the equation $I = \dot{Q} = C \cdot \dot{U}$ for constant capacitance C. An Agilent B2911A Precision Source/Measure Unit was utilized to provide a small and constant current up to 100 µA to the Teflon AF capacitor and to measure the voltage at the sample. The resulting capacity of the sample is constant and equal to the LCR results for voltages up to 100 V. The characterization results are presented in detail in Chapter 7.3.1.

4.4 Set-up for electrowetting-on-dielectric performance

For the EWOD performance, the *Saturated-Humidity-Setup* for CA evaluation was used, details see in Chapter. 4.2. The electrical voltage is supplied by a pair of Kepco amplifiers (BOP) and controlled by a function generator (Agilent 33220A). Symmetrical triangular voltages with constant slopes are applied to EWOD samples, which are introduced in detail in Chapter 7.3.1.

4.5 Surface topography characterisation

Several measurement methods were employed to gather information about surface topography. Initially, an optical microscope was utilized during the fabrication process to check for surface impurities and pinholes. However, the optical microscope only provides limited information and cannot reveal details about microstructure or surface properties like roughness.

To obtain detailed analysis at micro- and nanoscale, two other techniques were applied in this study: the scanning electron microscope (SEM) and atomic force microscope (AFM). These techniques are introduced in the following subsections.

4.5.1 SEM

A scanning electron microscope (SEM) produces gray-scale images of a sample by scanning the surface with a focused beam of electrons[166]. When the electron beam interacts with the sample surface, the emitted signals, including scattered primary electrons, secondary electrons (SE), and X-rays, are detected to provide information on the surface topography and chemical composition of the samples. The SEs are commonly used to image sample shapes and provide topographic imaging with a high resolution of a few nanometers. The SEM instrument used in this work is a Hitachi SU8030. An acceleration voltage between 2-8 kV with a current between 2-10 µA was applied to obtain images of micro- and nano-structures and additionally the information on the height of photolithographic micro-pillars. For the non-conductive polymers, an ultrathin (≈ 10 nm) thermally evaporated gold layer was applied on the polymer surface to conduct away the accumulated electrostatic charge during scanning[35, 54, 167]. Further information on the working and operation principles can be found elsewhere[166, 168, 169].

4.5.2 AFM

Atomic force microscopy (AFM) is a scanning microscope that probes the surface of a sample[170, 171]. An AFM consists of a cantilever containing a sharp tip, laser, photodiode detector, piezoelectric scanner, and feedback electronics. Typically, AFM is operated in two basic modes, tapping and contact mode. The tapping mode is commonly used for visualization of the surface topography down to atomic resolution. It involves oscillating the cantilever at its resonant frequency, causing the tip to lightly tap the sample surface during scanning. The oscillation amplitude is monitored to maintain a consistent tip-sample interaction, and this data is used to generate an image. Tapping mode causes less damage due to the fewer contacts of the tip to the surface in comparison to the contact mode, in which the tip is continuously in physical contact with the sample surface while across the sample's surface. In addition to its imaging capabilities, the contact mode in AFM can also be utilized for acquiring force-displacement curves[151, 172, 173]. This involves lowering the tip towards the sample surface and recording the deflection of the cantilever (approval curve). By analyzing this approach force curve, it is possible to obtain the mechanical properties of the sample such as stiffness and Young's modulus [172, 173]. Further information on the working and operation principles can be found elsewhere[151, 172, 173].

In this study, the AFM instrument Brucker Dimension Edge is applied. Two types of cantilevers were selected for different purposes: NCHV-A for topographic imaging via contact mode and Brucker Scanasyst-Fluid for force-indentation measurements via contact mode. To analyze the force-indentation curve, open-source software called AtomicJ was used.[150, 151, 174, 175].

4.6 Chemical analysis

As previously discussed, plasma treatment is a highly effective method for modifying the surface properties of polymers. However, this technique may not only remove surface materials and modify surface topography, but also can introduce new species to the surface, resulting in changes to the functional groups and wetting properties of the surface [176]. Therefore, chemical analysis techniques such as Fourier-transform infrared spectroscopy (FTIR) and x-ray photoelectron spectroscopy (XPS) were applied as well in this study, to investigate these changes. These techniques are introduced in the following subsections briefly.

4.6.1 FTIR

FTIR is a widely used analytical technique in fields such as organic synthesis, polymer science, and petrochemical engineering for compound identification. FTIR can be performed in several different modes. The most common modes are transmission, attenuated total reflection (ATR-FTIR), and specular reflection mode. During transmission analysis in FTIR, a sample is exposed to IR radiation, absorbing some of the radiation while the rest passes through, resulting in a unique spectrum that corresponds to the molecular structure of the sample, often called a "fingerprint" [177–179]. ATR-FTIR involves placing an infrared transparent crystal in contact with the sample and sending IR light in at an angle so that the light totally internally reflects from the interface between the samples and the ATR crystal. In specular reflection FTIR, broadband IR light illuminates the sample and the reflected light is collected[180].

In this work, the Bruker Tensor 27 FTIR Spectrometer is used to investigate the functional groups of applied samples via transmission mode. Spectral data were collected in the range of 4000 to 400 cm^{-1} with a resolution of 4 cm^{-1}.

4.6.2 XPS

XPS is a surface-sensitive and non-destructive technique based on the photoelectric effect, in which x-rays simulate the surface of a material and the kinetic energy of the emitted electrons is measured[181]. XPS is a powerful analytical method for elemental identification and reveals chemical state information from the elements in the sample. However, insulating samples, like polymers, provide challenges to XPS analysis due to the surface charging effect[182]. Unlike conducting materials, which are able to continuously transfer electrons to the surface to replace electrons loss due to photoelectron and Auger processes, the loss of the electrons on the surface of an insulating sample leads to a positive charge when the photoelectrons are emitted. As a result, these photoelectrons may exhibit a shift to slightly higher binding energies[182]. This charging effect is generally compensated by using an electron flood gun to replace the loss of photoelectrons[182, 183].

In this work, XPS measurements were carried out on a PHI Versa Probe III-spectrometer equipped with a monochromatic Al-Kα X-ray source and a hemispherical analyzer (acceptance angle: $\pm 22°$). Pass energies of 140 eV and 27 eV and step widths of 0.5 eV and 0.05 eV were used for survey and detail spectra, respectively. The excitation energy was 1486.6 eV and the beam energy and spot size were 25 W, and 100 µm, respectively.

4.7 Summary

In this chapter, the experimental setup, as well as the characterization methods for the surface wetting property, dielectric property, surface structural information, and chemical analysis are presented.

- Wetting property:
  The wetting property of a liquid is determined by the pendant drop method, while the wetting property of a solid is described by CA via the sessile drop method. For the determination of various and temperature-dependent CAs (θ_{init}, θ_{adv}, θ_{rec}) two different CA measurement setups with the temperature-controlled units are presented: *Evaporation-Setup* and *Saturated-Humidity-Setup*.

- Electrical characterization:
  The determination of the dielectric property is essential for achieving reliable EWOD performances, and characterization processes are introduced for this purpose.

- Surface topography:
  The SEM and AFM are applied to reveal the surface structural information. Moreover, the contact mode of AFM is used to analyze the surface-near Young's modulus of samples.

- Chemical analysis:
  The FTIR spectrometer and XPS technique are applied for bulk and surface chemical analyses.

Chapter 5

Modification of Young's equation

Contents

Some sections of this chapter were previously published in the paper titled "Temperature Dependence of Water Contact Angle on Teflon AF1600"[137].

5.1 Introduction

The wetting property, which is typically quantified by the contact angle (CA), plays a crucial role not only in nano- and micro-fabrication processes, but also in a wide range of applications such as Lab-on-chip systems and optofluidics[45, 52, 93]. In recent decades, this property has gained significant attention due to the expanding application fields and the need for improved control of the CAs at different temperatures. The CA of a liquid drop (typically water) on a specific solid surface is determined by the force equilibrium of the three interface tensions at the triple line according to the well-known Young's equation[2], $\theta = (\gamma_{\mathrm{sa}} - \gamma_{\mathrm{sl}})/\gamma_{\mathrm{la}}$. However, in real life, the measured CA varies within a certain range between the so-called advancing CA, θ_{adv}, and the receding CA, θ_{rec}. The explanations for this variation of CA are surface imperfections, such as surface roughness[13], chemical heterogeneity[14], and adsorption[15, 16]. Wenzel's and Cassie's equations describe the CA on a roughened and structured solid surface and interpret this effect on the surface wettability. Details about these equations are introduced in Chapter 2.1.1.

Despite its importance, there is currently no quantitative model that can fully describe the variation of the CA. Instead, the Young CA, denoted as θ_Y, is often determined using the average of the advancing contact angle and the receding contact angle, i.e., $\theta_Y = (\theta_a + \theta_r)/2$, or alternatively, using $\cos\theta_Y = (\cos\theta_a + \cos\theta_r)/2$. However, this method lacks physical meaning and precision. There is a growing need for a better understanding of the relationship between Young's CA and advancing and receding CAs. In addition, the temperature dependence of CAs is not well understood, which is a critical factor for their wider applications, such as the EW-based variable liquid lens.

In this chapter, the author presents the temperature-dependent CAs on one of the most applicable hydrophobic materials, Teflon AF1600, and finds out that a temperature-independent friction-like force, as well as the temperature-dependent water adsorption onto a solid surface, contributes to the CA determination. Additionally, the author proposes a model to describe the CA affected by these contributions and quantifies them experimentally on Teflon AF1600.

5.2 Fabrication of homogeneous thin films

According to the standard fabrication process of Teflon AF1600 from Dupont, the baking procedure consists of three steps: 175 °C for 10 min to remove the solvent, 165 °C (glass transition temperature of Teflon AF1600) and 330 °C (glass transition temperature of PDD) for 5 min and 15 min, respectively. However, the optical observation of surface quality with a microscope after each baking step revealed that pinholes were introduced by the third baking step, i.e. the 330° for 15 min. A typical optical microscope image is shown in Fig.5.1(a). A consequence of the presence of the surface pinholes is the stick-slip phenomenon observed when measuring the CA on such surfaces, as shown in Fig. 5.1(b). The CA measurements were conducted with *Evaporation-Setup* and the details are described in Chapter 4.2. To eliminate these pinholes and improve surface homogeneity, two baking steps were considered. However, it is essential to ensure that the surface properties, including wettability, topography, and functional groups, stay unaffected by the third baking step. In order to facilitate this, various methods were used to determine the surface quality before and after the last baking step at a temperature of 330 °C: FTIR[115] (the reflective spectral range of $3500 - 400$ cm^{-1}) for analyzing the surface functional groups, AFM for observation of surface morphology, and CA measurement to estimate the surface tension. Details of those methods are presented in Chapter 4. The investigation showed that the surface properties of the Teflon AF1600 thin films were not affected by the last baking step. Therefore, two steps were applied for the baking process, at 175 °C and 165 °C for 10 min and 5 min, respectively, to achieve pinhole-free Teflon AF1600 surfaces.

The surface roughness was characterized by AFM, revealing a root mean square roughness of 0.82 nm over a scanning area of 1×1 µm^2 and a maximal height of 8.2 nm. A typical AFM image on Teflon AF1600 is shown in Fig. 5.2.

In summary, to obtain a high-quality Teflon AF1600 film for wettability studies, various fabrication steps were optimized, including controlling the film thickness, enhancing the adhesion of Teflon AF1600 by applying Ti-Prime, and pre-investigating the baking process to achieve a pinhole-free surface and avoid the stick-slip phenomenon during CA measurements. These steps ensure the reproducibility and accuracy of the wettability

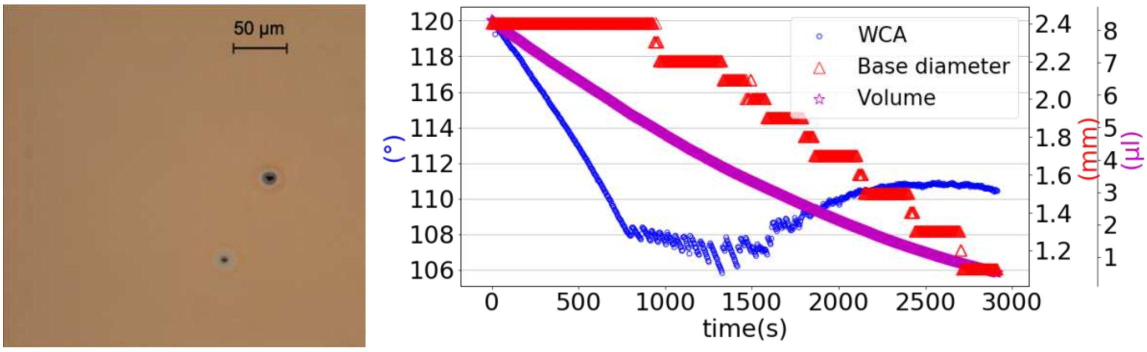

(a) Pinholes (b) Stick-slip phenomenon

Fig. 5.1: (a) Optical micrograph of a Teflon AF1600 surface: pinholes were observed after the third baking step at 330 °C.[137], (b) The stick-slip phenomenon by CA measurement on the pinholes-presented surface.

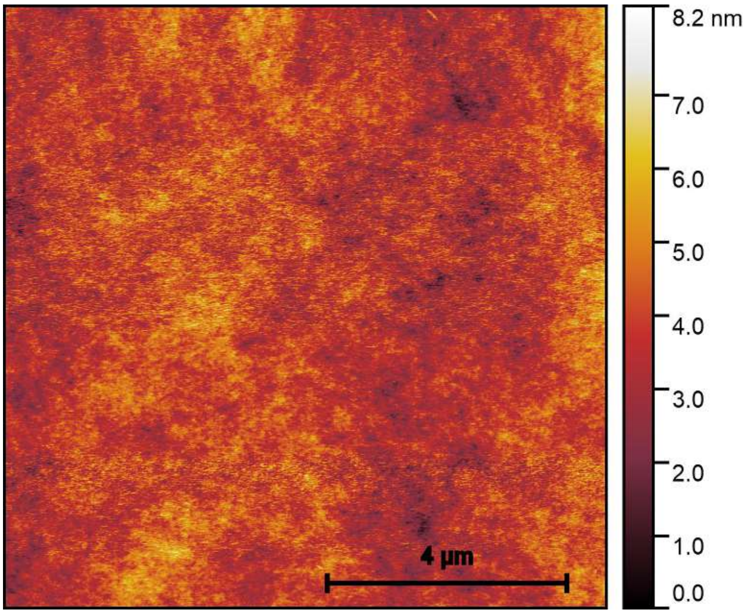

Fig. 5.2: Typical AFM image on Teflon AF1600 film.

measurements on the Teflon AF1600 surface. The improved fabrication process has been published in reference[137].

5.3 Temperature dependency of CA

To investigate the impact of temperature on surface wettability, the measurement of CAs on these optimized surfaces of Teflon AF1600 was conducted at different temperatures using *Evaporation-Setup*. Details of the temperature-dependent experimental setup and the *Evaporation-Setup* are reported in Chapter 4.2.1 and 4.2.2, respectively.

Water droplet evaporation is a dynamic process and the CA might suffer from dynamic effects. In addition, as introduced in the previous Chapter 2.1.3, static and dynamic CAs are different concepts. The static CA is determined by the force equilibrium at the triple line through the interface tensions, while the dynamic CA is additionally affected by viscous forces. In the droplet evaporation process, the reduction in droplet volume is accompanied by the movement of the triple line, which might affect the CA by the velocity of this movement[184, 185]. Therefore, to investigate the CAs that are only determined by interface tensions, it is necessary to validate whether the dynamic effect is negligible and whether the CAs are in a quasi-static condition. In the following subsections, an evaluation of the impact of the triple line movement on the CA determination is presented. The results of CAs measured at different temperatures under quasi-static conditions are also presented.

5.3.1 Quasi-static condition

The quantity used to evaluate the impact of triple line movement on the CA is the capillary number, Ca[186]:

$$\mathrm{Ca} = (\mu \cdot v)/\gamma, \tag{5.1}$$

where μ, γ, and v represent the dynamic viscosity, liquid surface tension, and triple line velocity, respectively. To ensure a quasi-static condition and disregard the dynamic effect during the droplet evaporation process, it is crucial to ensure that the Ca number remains below the critical value of 10^{-5} [5, 73]. Therefore, the velocity of the triple line for quasi-static conditions is expressed as:

$$v \leq 10^{-5} \cdot \frac{\gamma}{\mu}, \tag{5.2}$$

To illustrate, in the case of water evaporation at a temperature of 25 °C, with dynamic viscosity and surface tension values of $\mu = 0.0013$ Pa s and $\gamma = 0.072$ N/m, the maximum triple line velocity that satisfies the quasi-static condition is 0.55 mm/s. As the dynamic viscosity μ and surface tension γ in Eq. 5.2 are both temperature-dependent, the maximal speed of the triple line is also temperature-dependent. This temperature dependency is shown in Fig. 5.3.

The triple line movement velocity is written as the time derivative of contact radius r of the contact area between the droplet and solid surface,

$$v = \frac{dr}{dt}. \tag{5.3}$$

The contact radius as well as the CA determine the droplet volume, as described by Eq. 4.3 and shown in Fig. 4.4 in Chapter 4. The equation of droplet volume, Eq. 4.3, can be rewritten as in terms of the droplet base-radius r as a function of the volume V:

$$r = \sqrt[3]{\frac{3 \cdot V}{\pi} \cdot \frac{\sin^3 \theta}{(1-\cos\theta)^2 \cdot (2+\cos\theta)}}. \tag{5.4}$$

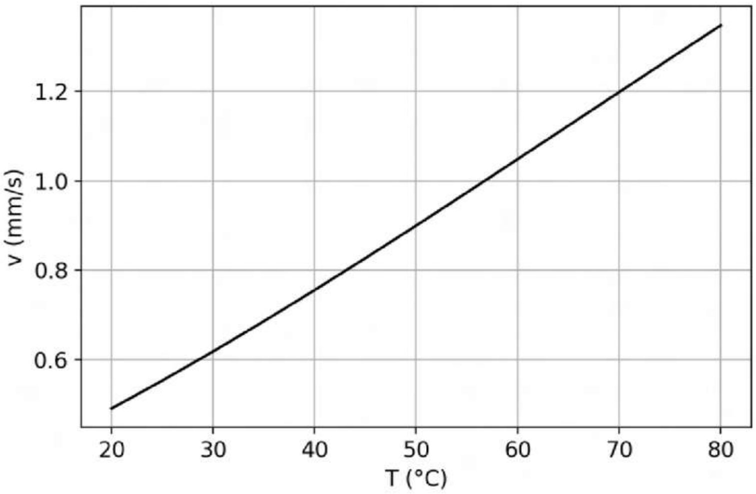

Fig. 5.3: The critical velocity of the triple line movement (for a water droplet) as a function of temperature.

In the droplet evaporation process, the triple line stays pinned during the CCR regime and starts moving in the CCA range, where the CA stays constant, and the contact radius decreases as a result of the volume loss. Details about the CCA and CCR are reported in Chapter 4.2.2.1. Based on the Eqs. 5.3 and 5.4, the droplet volume and the measured CA at the CCA regime (receding CA), the resulting speed of the triple line can be calculated.

In the investigated temperature range, the initial droplet volume was set at approximately 5 µL. The results of the CA evaluation are presented in Fig.5.4. The speed of the triple line movement due to the droplet evaporation is 0.00023 and 0.007 mm/s at temperatures of 20 and 80 °C, respectively. The obtained values for the triple line velocity are significantly lower by three orders of magnitude than the critical value shown in Fig. 5.3, indicating that the surface tension (γ) plays a more dominant role than the viscous force of the liquid ($\mu \cdot v$) in determining the CA using the *Evaporation-Setup*. Thus, the dynamic effects on CAs during droplet evaporation are negligible and the CAs measured are in quasi-static conditions.

5.3.2 Experimental results

The droplet evolution is observed by the water droplet evaporation process at different temperatures. Typical results of the droplet evolution, including the evolution of CA, the droplet volume, and the contact diameter at different temperatures are shown in Fig. 5.4. The results show clearly a CCR regime followed by a CCA regime during the droplet evaporation process. In the CCR regime, the triple line stays pinned, indicating a constant contact radius of the liquid solid area, while the volume and CA continuously decrease. Once the triple line gets depinned and starts to move, the CCA regime is established. In this regime, the CA stays constant while the volume and contact radius continuously decrease[137]. More details of CCR, constant contact radius regime, and CCA, constant contact angle regime, are introduced in Chapter 4.2.2.1.

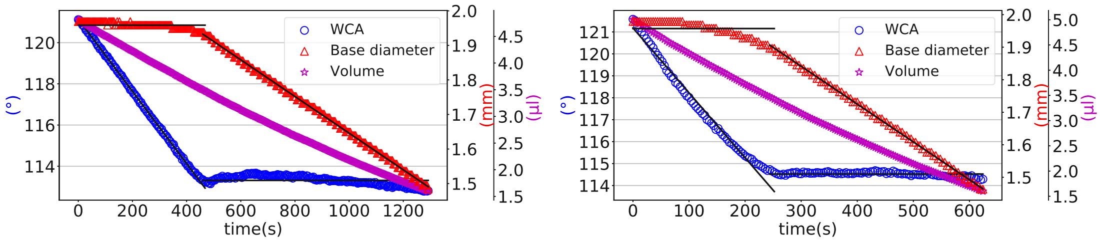

(a) T=20 °C (b) T=30 °C

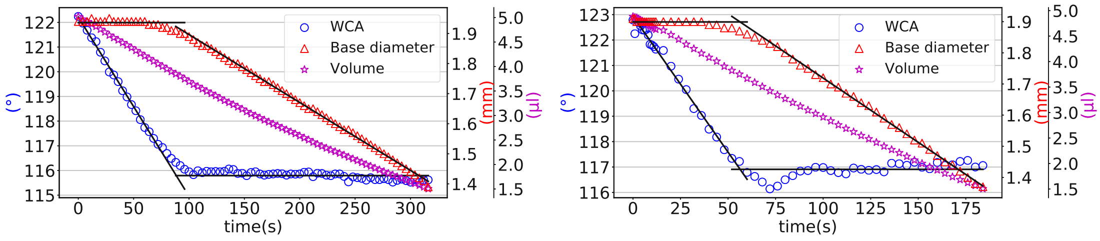

(c) T=40 °C (d) T=50 °C

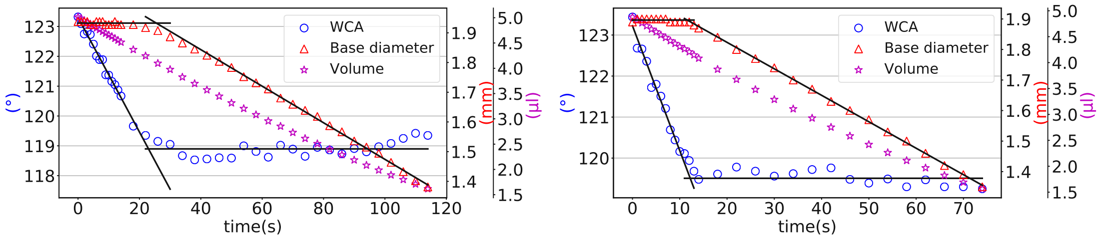

(e) T=60 °C (f) T=70 °C

Fig. 5.4: CA, contact base diameter and droplet volume evolution due to droplet evaporation over time at (a) $T = 20°\text{C}$, (b) $T = 30°\text{C}$, (c) $T = 40°\text{C}$, (d) $T = 50°\text{C}$, (e) $T = 60°\text{C}$, (f) $T = 70°\text{C}$. The solid lines represent the fitted curves in the CCR and CCA regimes. In the CCR regime, the contact base area stays constant and the CA decreases. In the CCA regime, however, the contact base area decreases and the CA stays constant.

Two characteristic CAs are extracted from the evaporation process: the initial CA (θ_{init}) and the receding CA (θ_{rec}). Both values are determined from the experimental data by a linear least square fit. The results of initial and receding CA (θ_{init} and θ_{rec}) as a function of temperature ranging from 20 to 80 °C are shown in Fig. 5.5. The initial CA, θ_{init}, slightly changes from 121.1 to 122.9 ° as the temperature increases from 20 to 80 °C, while the receding CA, θ_{rec}, significantly increases from 113.3 to 119.7 °.

The measurement uncertainty of θ_{init}, especially for temperatures higher than 50 °C with an evaporation rate larger than 0.02 µL/s, is determined from the maximum measurement delay of 1 s. The measured θ_{init} could be maximally 0.3 ° smaller than the actual θ_{init}. Moreover, the θ_{rec} at higher temperatures ($T > 50\,°\text{C}$) are more scattered with a standard deviation of about 0.25 ° compared to about 0.12 ° at lower temperatures ($T < 50\,°\text{C}$).

The initial CA, θ_{init}, refers to a CA on a dry solid surface. The receding CA, θ_{rec}, is believed to be affected by the water adsorption, as the triple line moves in the direction of the water-covered surface area, which is previously below the droplet and a part of the liquid-solid interface. Accordingly, the solid air interface tension γ_{sa} should have experienced the influence of water adsorption. When the applied temperature increases, the receding CA θ_{rec} increases due to the less adsorption of water onto the solid surface. Details about the water adsorption contribution are presented in the following sections.

A similar trend of θ_{init} when varying the temperature is observed by Weisensee et al.[16]. They measured the CA on PTFE-coated surfaces in the air and a pure water vapor environment when controlling the pressure from 60 to 1000 mbar, with the corresponding temperature ranging from 36 to 100 °C. The CA measured in the air environment, which is comparable to the initial CA (θ_{init}) in this study, showed no significant changes when the pressure and corresponding temperature increased. Furthermore, their results revealed that the CA was significantly higher, by approximately 10°, in an air environment in comparison to a pure water vapor environment. These results suggest that water adsorption may occur on the surface of a hydrophobic material, resulting in a decrease in the CA.

In summary, this chapter presents the primary results of the study regarding the relationship between CAs and temperature. The results reveal a minor variation in the initial CA, θ_{init}, and a significant change in the receding CA, θ_{rec}, with respect to the temperature. The subsequent sections will delve into the factors, such as water adsorption, that influence the values of θ_{init} and θ_{rec}.

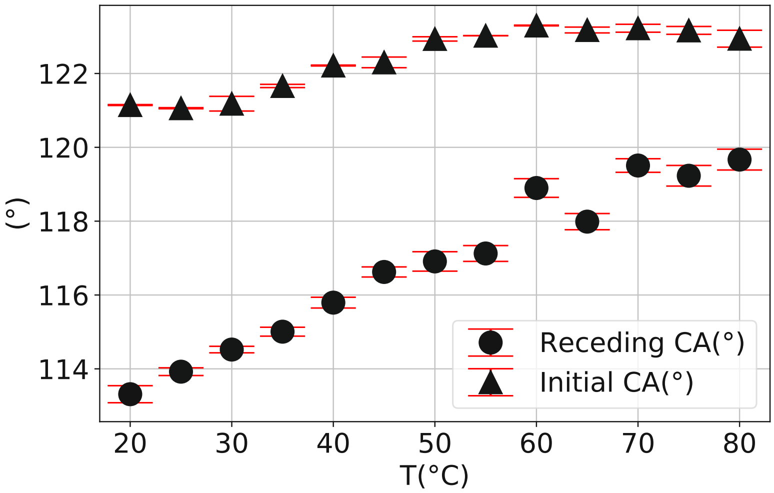

Fig. 5.5: Results of θ_{init} and θ_{rec} on Teflon AF1600 over temperature[137].

5.3.3 Analyse of the CA changes

According to Young's equation[2], the interface tensions equilibrium for initial and receding CA is written as:

$$\gamma_{\mathrm{la}}^{\mathrm{init}} \cdot \cos\theta_{\mathrm{init}} = \gamma_{\mathrm{sa}}^{\mathrm{init}} - \gamma_{\mathrm{sl}}^{\mathrm{init}}, \tag{5.5}$$

and

$$\gamma_{\mathrm{la}}^{\mathrm{rec}} \cdot \cos\theta_{\mathrm{rec}} = \gamma_{\mathrm{sa}}^{\mathrm{rec}} - \gamma_{\mathrm{sl}}^{\mathrm{rec}}. \tag{5.6}$$

The superscript *init* and *rec* refers to the initial and receding condition with the corresponding CA, θ_{init}, and θ_{rec}, respectively. Both CAs are described by the interface tensions, i.g. liquid air interface tension γ_{la}, solid liquid interface tension γ_{sl}, and solid air interface tension γ_{sa}. As γ_{la} depends on the temperature and pressure and stays constant during the evaporation process, the γ_{la} stays the same at the initial and receding condition, $\gamma_{\text{la}}^{init} = \gamma_{\text{la}}^{rec}$. The difference value of γ_{sa} and γ_{sl} at the initial and receding condition, contributes to the difference value of CAs, namely, θ_{init} and θ_{rec}. Combining the Eqs. 5.5 and 5.6, the effective solid surface tension between the initial and receding condition during the evaporation process, $\gamma_{\text{la}} \cdot (\cos\theta_{\text{rec}} - \cos\theta_{\text{init}})$, is described by

$$\gamma_{\text{la}} \cdot (\cos\theta_{\text{rec}} - \cos\theta_{\text{init}}) = \Delta\gamma_{\text{sa}}(\theta_{\text{rec}}, \theta_{\text{init}}) - \Delta\gamma_{\text{sl}}(\theta_{\text{rec}}, \theta_{\text{init}}) \tag{5.7}$$

with $\Delta\gamma_{\text{s}*}(\theta_{\text{rec}}, \theta_{\text{init}}) = \gamma_{\text{s}*}^{sta} - \gamma_{\text{s}*}^{init}$, the subscript $s*$ represents *sl* or *sa*.

Now, let's discuss the temperature dependency of Eq.5.7.

γ_{la}. The values of the temperature dependence of γ_{la} are taken from the literature [187] and validated by some own experiments.

θ_{init} *and* θ_{rec}. The θ_{init} and θ_{rec} as a function of temperature is acquired by the experiments, see the former section, Chapter 5.3.2.

$\Delta\gamma_{sl}(\theta_{rec}, \theta_{init})$. The difference of the solid-liquid tension, $\Delta\gamma_{\text{sl}}(\theta_{\text{rec}}, \theta_{\text{init}})$ is described by Gibbs adsorption equation[74],

$$\Delta\gamma_{\text{sl}}(\theta_{\text{rec}}, \theta_{\text{init}}) = -\frac{RT}{A_m} \cdot \ln\frac{\sin\theta_{\text{rec}}}{\sin\theta_{\text{init}}} \tag{5.8}$$

where R, T, A_m is the universal gas constant, absolute temperature, and molar surface area of Teflon AF1600. A_m is described by the following equation:

$$A_m = (\frac{M_0}{\rho})^{2/3} N^{1/3}. \tag{5.9}$$

For material Teflon AF1600, A_m is 192436.08 m^2/mol, calculated with the Avogadro constant $N = 6.022 \cdot 10^{23}$ mol^{-1}, the density $\rho = 1.78$ g/mL, and the monomer weight $M_0 = 193.63$ g/mol, which is given by the components 4,5-difluor-2,2-bis-47(trifluormethyl)-1,3-dioxol (PDD, 244.04 g/mol, 65 mol %) and tetrafluorethylen (TFE, 100.02 g/mol, 35 mol %). The results of the effective solid surface tension, $\gamma_{\text{la}} \cdot (\cos\theta_{\text{rec}} - \cos\theta_{\text{init}})$, which is calculated by the measured CAs, and the change of solid-liquid interface tension, $\Delta\gamma_{\text{sl}}(\theta_{\text{rec}}, \theta_{\text{init}})$, which is calculated by the Eq. 5.8, are depicted in Fig. 5.7. The results clearly show that the $\Delta\gamma_{\text{sl}}(\theta_{\text{rec}}, \theta_{\text{init}})$ (triangle points), cannot sufficiently explain the effective solid surface energy change, $\gamma_{\text{la}} \cdot (\cos\theta_{\text{rec}} - \cos\theta_{\text{init}})$ (round points).

$\Delta\gamma_{sa}(\theta_{rec}, \theta_{init})$. When turning back to Eq. 5.7, in addition to the constant γ_{la} and the change of γ_{sl}, the change of γ_{sa}, $\Delta\gamma_{\text{sa}}(\theta_{\text{rec}}, \theta_{\text{init}})$, should also contribute to the variation of CA from θ_{init} to θ_{rec}. The change of γ_{sa} is mainly due to the adsorption of water onto the surface and can be omitted at high temperatures. However, Figure. 5.7 shows that at $T = 80\,^\circ\text{C}$, the difference between the absolute value of the effective solid surface tension, $\gamma_{\text{la}} \cdot (\cos\theta_{\text{rec}} - \cos\theta_{\text{init}})$ and the $\Delta\gamma_{\text{sl}}(\theta_{\text{rec}}, \theta_{\text{init}})$, is about 3 mN/m. This change can not be explained by the adsorption of water on a hydrophobic surface at such a high temperature.

Consequently, an additional force, F_f, with a static friction-like behavior, as shown in Fig. 5.6, is introduced to expand Young's equation and ensure static force equilibrium:

$$F_\mathrm{f}(t) = \gamma_\mathrm{la} \cdot \cos\theta(t) + \gamma_\mathrm{sl}(t) - \gamma_\mathrm{sa}(t). \tag{5.10}$$

The CAs are observed over time during the evaporation process.

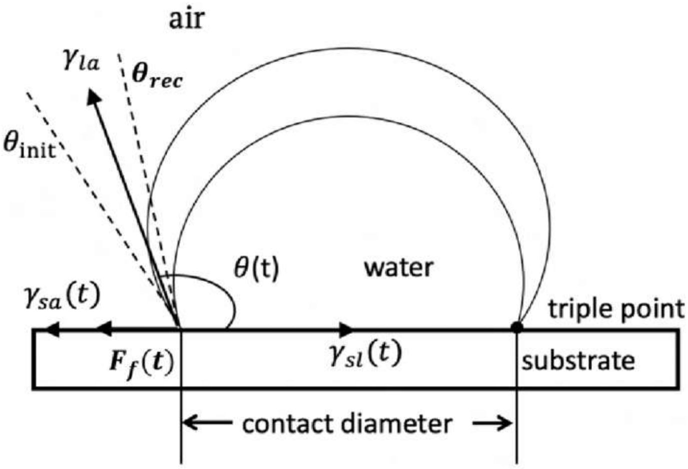

Fig. 5.6: Force equilibrium at the triple line during droplet evaporation. Interface tensions γ_la, γ_sl, γ_sa and a friction-like force F_f contribute to the force equilibrium.

When the droplet is initially deposited on the solid surface, it adjusts to an equilibrium shape by the initial interface tensions with an initial contact radius and an initial CA θ_init:

$$F_\mathrm{f}^\mathrm{init} = \gamma_\mathrm{la} \cdot \cos\theta_\mathrm{init} + \gamma_\mathrm{sl}^\mathrm{init} - \gamma_\mathrm{sa}^\mathrm{init}. \tag{5.11}$$

The superscript *init* refers to the initial solid surface condition (dry, free from adsorption) with the corresponding CA, θ_init. The initial droplet volume is about 5 µL. The contact radius of the solid liquid area is less than 1 mm. This value is much smaller than the capillary length of water, which is 2.7 mm, so that the effect of gravity on the CAs can be neglected. Details about capillary length can be found in Chapter 4.2. Therefore, we assume $F_\mathrm{f}^\mathrm{init} = 0$.

During the evaporation process, the CA experiences the CCR regime firstly, in which the contact areas stays constant and the CA decreases. The force equilibrium at the triple line is maintained due to the variable friction-like force F_f, that acts in the direction of γ_sa, see Fig. 5.6 When the value of F_f increases up to its maximum value, F_fmax, the triple line depins and starts to move in the CCA regime with the constant corresponding CA θ_rec. The force equilibrium is then written as:

$$F_\mathrm{fmax} = \gamma_\mathrm{la} \cdot \cos\theta_\mathrm{rec} + \gamma_\mathrm{sl}^\mathrm{rec} - \gamma_\mathrm{sa}^\mathrm{rec}, \tag{5.12}$$

where the superscript *rec* refers to the solid surface condition in the absorption-desorption equilibrium state around the triple line, with the corresponding CA θ_{rec}. Combining the force equilibrium equations, Eqs. 5.11 and 5.12, we get:

$$F_{\mathrm{fmax}} = \gamma_{\mathrm{la}} \cdot (\cos\theta_{\mathrm{rec}} - \cos\theta_{\mathrm{init}}) + \Delta\gamma_{\mathrm{sl}}(\theta_{\mathrm{rec}}, \theta_{\mathrm{init}}) - \Delta\gamma_{\mathrm{sa}}(\theta_{\mathrm{rec}}, \theta_{\mathrm{init}}). \tag{5.13}$$

The first term on the right side is calculated by the well-known $\gamma_{\mathrm{la}}(\mathrm{T})$ and the measured θ_{init}, θ_{rec}. The second term, $\Delta\gamma_{\mathrm{sl}}(\theta_{\mathrm{rec}}, \theta_{\mathrm{init}})$, is calculated by Eq. 5.8. The last term, $\Delta\gamma_{\mathrm{sa}}(\theta_{\mathrm{rec}}, \theta_{\mathrm{init}})$ is unknown with the droplet-evaporation experiments and will be discussed in the following part.

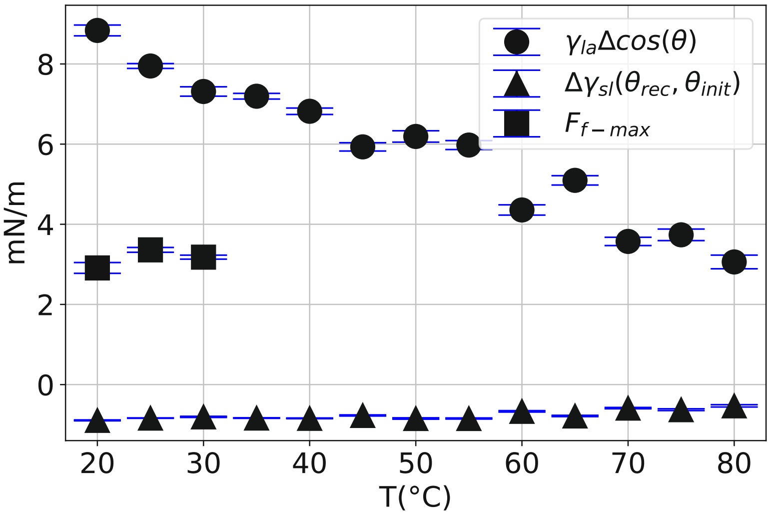

Fig. 5.7: Results of effective solid surface tension change $\gamma_{\mathrm{la}} \cdot \Delta\cos\theta$ from the evaporation experiments, the solid liquid interface tension difference $\Delta\gamma_{\mathrm{sl}}(\theta_{\mathrm{rec}}, \theta_{\mathrm{init}})$ calculated from the Gibbs adsorption equation (Eq. 5.8), the friction-like force F_{fmax} evaluated from soaking and evaporation experiments. All results are plotted against temperatures.

5.4 CA by soaking experiments

When the droplet evaporates, the triple line moves in the direction of the water-covered area, which is previously below the droplet. Accordingly, the solid-air interface tension, γ_{sa}, should have experienced the effect of water adsorption. Fowkes, McCarthy, and Mostafa described the change of solid-air interface tension ($\Delta\gamma_{\mathrm{sl}}$) based on the Gibbs adsorption equation[188],

$$\Delta\gamma_{\mathrm{sa}} = RT \int_0^{p_0} \Gamma \mathrm{d} \ln p_{\mathrm{v}}, \tag{5.14}$$

where Γ is the concentration of adsorbed vapor on a solid as a function of the vapor pressure p_{v} up to its equilibrium vapor pressure p_0 of the liquid. However, the concentration of adsorbed vapor Γ is hard to estimate and difficult to directly measure *in-situ* for hydrophobic materials. In this study, the direct analysis of the adsorption effect by measuring the CA on a surface, which is thoroughly soaked with water, is investigated. In the following, the experimental process and results are presented.

The samples were immersed in water at different temperatures for 10 min, allowing water adsorption on the surface. Then the samples were promptly placed into the closed chamber for the CA measurement using the *Saturated-Humidity-Setup*. Details of the setup can be found in Chapter 4.2.1. The CA of the soaked samples, θ_{soak}, exhibited values different from both the initial and receding CAs (θ_{init} and θ_{rec}). Table 5.1 presents the results of the CA measurements at various temperatures. Using the experimental results for the θ_{init} on the dry surface, and the θ_{soak} on the water-soaked surface, the difference between the CAs is calculated by using the force equilibrium equation at the triple line (Eq. 5.10), as

$$0 = \gamma_{\mathrm{la}} \cdot (\cos\theta_{\mathrm{soak}} - \cos\theta_{\mathrm{init}}) + \Delta\gamma_{\mathrm{sl}}(\theta_{\mathrm{soak}}, \theta_{\mathrm{init}}) - \Delta\gamma_{\mathrm{sa}}(\theta_{\mathrm{soak}}, \theta_{\mathrm{init}}), \tag{5.15}$$

where $\Delta\gamma_{\mathrm{sl}}(\theta_{\mathrm{soak}}, \theta_{\mathrm{init}})$ can be calculated by the Gibbs adsorption equation, Eq. 5.8. $\Delta\gamma_{\mathrm{sa}}(\theta_{\mathrm{soak}}, \theta_{\mathrm{init}}) = \gamma_{\mathrm{sa}}^{\mathrm{soak}} - \gamma_{\mathrm{sa}}^{\mathrm{init}}$, equals to $\Delta\gamma_{\mathrm{sa}}(\theta_{\mathrm{rec}}, \theta_{\mathrm{init}}) = \gamma_{\mathrm{sa}}^{\mathrm{rec}} - \gamma_{\mathrm{sa}}^{\mathrm{init}}$ with the consideration that the $\gamma_{\mathrm{sa}}^{\mathrm{soak}}$ and $\gamma_{\mathrm{sa}}^{\mathrm{rec}}$ are both referring to the solid surface that is covered with water before and is in adsorption equilibrium.

Combining the Eqs. 5.15 and 5.13, the limit of the friction-like force, F_{fmax}, is written as:

$$F_{\mathrm{fmax}} = \gamma_{\mathrm{la}} \cdot (\cos\theta_{\mathrm{rec}} - \cos\theta_{\mathrm{init}}) + \Delta\gamma_{\mathrm{sl}}(\theta_{\mathrm{rec}}, \theta_{\mathrm{init}}) - \gamma_{\mathrm{la}} \cdot (\cos\theta_{\mathrm{soak}} - \cos\theta_{\mathrm{init}}) - \Delta\gamma_{\mathrm{sl}}(\theta_{\mathrm{soak}}, \theta_{\mathrm{init}}), \tag{5.16}$$

simplified as:

$$F_{\mathrm{fmax}} = \gamma_{\mathrm{la}} \cdot (\cos\theta_{\mathrm{rec}} - \cos\theta_{\mathrm{soak}}) + \Delta\gamma_{\mathrm{sl}}(\theta_{\mathrm{rec}}, \theta_{\mathrm{soak}}). \tag{5.17}$$

The results of F_{fmax} are listed in Table. 5.1 and shown in Fig. 5.7 as well. The friction-like force, F_{f}, is assumed as temperature-independent and the results of soaking experiments show that its limit, F_{fmax}, maintains a constant value of 3.15 ± 0.19 mN/m at the investigated temperature of the soaking experiments, $20 - 30$ °C. This value is validated by the previous evaporation experiments at higher temperatures as well. For instance, at the temperature of 80 °C, the adsorption is assumed to be zero, namely the solid air interface tension, γ_{sa}, at initial and receding conditions is constant, $\gamma_{\mathrm{sa}}^{\mathrm{init}} - \gamma_{\mathrm{sa}}^{\mathrm{rec}} = 0$. The difference between the effective solid surface tension, $\gamma_{\mathrm{la}}(\cos\theta_{\mathrm{init}} - \cos\theta_{\mathrm{rec}})$, and the $\gamma_{\mathrm{sl}}^{\mathrm{init}} - \gamma_{\mathrm{sl}}^{\mathrm{rec}}$ calculated by Gibbs adsorption equation, is 3 mN/m, which is comparable to the friction limit, 3.15 ± 0.19 mN/m, from the soaking experiments.

T	θ_{init}	θ_{soak}	θ_{rec}	F_{fmax}
20	121.1 ± 0.01	116.1 ± 0.05	113.3 ± 0.23	2.91 ± 0.13
25	121.0 ± 0.01	117.2 ± 0.03	113.9 ± 0.10	3.36 ± 0.06
30	121.2 ± 0.2	117.7 ± 0.08	114.5 ± 0.09	3.18 ± 0.05

Tab. 5.1: Soaking experiment results: the effective solid energy change after soaking, $\gamma_{\mathrm{la}} \cdot (\cos\theta_{\mathrm{soak}} - \cos\theta_{\mathrm{init}})$ 5.58 mN/m at $T = 20$ °C, is comparable with the immersion energy 6 mN/m of Teflon measured by Chessick, Healey, and Zettlemoyer[189].

After immersing the samples in water and measuring the CAs, two different methods were used to release the adsorbed water from the surfaces: the first involved heating the samples to 50 °C for 10 s, while the second involved blowing nitrogen onto the surfaces. Subsequently, the CAs were measured again and found to be identical to those obtained on a fresh, non-water-adsorbed surface, e.g., 121.1 ± 0.01 ° at $T = 20\,^\circ\mathrm{C}$. These results suggest that the effect of water adsorption is reversible.

5.5 Introducing friction and adsorption-based contributions into Young's equation

As previously discussed, water adsorption can appear on hydrophobic materials and play a role in the force equilibrium at the triple line, consequently contributing to the determination of the CA. A model is introduced to describe the solid surface tension, γ_s, that takes the water adsorption into account by considering the adsorption coverage f on the solid surface.

The adsorption coverage, f, is defined as the area fraction of the occupied adsorption area to the total adsorption area[190]. The energy contribution of a fully occupied adsorption area is e with the same unity of γ, N/m or J/m^2. Therefore, the surface tension of a partially adsorbed surface is written as:

$$\gamma_\mathrm{s} = \gamma_\mathrm{s0} + f \cdot e, \tag{5.18}$$

where γ_s0 is the solid surface tension in a vacuum, representing a surface free from water adsorption. The interface energy between the liquid droplet and the solid surface is assumed as,

$$\gamma_\mathrm{sl} = \gamma_\mathrm{s0} + e, \tag{5.19}$$

with 100 % coverage ($f = 1$) as the contact area is fully covered with liquid. The solid air interface energy for the dry hydrophobic surface is assumed as,

$$\gamma_\mathrm{sa}^\mathrm{init} = \gamma_\mathrm{s0}, \tag{5.20}$$

with 0 % coverage ($f = 0$) as the solid air interface is free from adsorption. When the adsorption-desorption process reaches its equilibrium, like in the receding CA condition, the solid-air interface tension is written as

$$\gamma_\mathrm{sa}^\mathrm{rec} = \gamma_\mathrm{s0} + f \cdot e, \tag{5.21}$$

with an equilibrium coverage f.

Plugging those conditions into Eq. 5.10, the initial CA, θ_init, and receding CA, θ_rec, are described by

$$\gamma_\mathrm{la} \cdot \cos\theta_\mathrm{init} = -e, \tag{5.22}$$

and

$$\gamma_\mathrm{la} \cdot \cos\theta_\mathrm{rec} = F_\mathrm{fmax} - (1 - f) \cdot e, \tag{5.23}$$

respectively.

The relation between the initial CA and the receding CA is then given by:

$$\gamma_{\mathrm{la}} \cdot (\cos\theta_{\mathrm{rec}} - \cos\theta_{\mathrm{init}}) = F_{\mathrm{fmax}} + f \cdot e. \tag{5.24}$$

The friction-like force F_{fmax} is experimentally determined, $F_{\mathrm{fmax}} = 3.15 \pm 0.19$ mN/m, and is temperature independent. e can be calculated from Eq. 5.22. It shows a constant value in the temperature range $20 - 50$°C, with $e = 37.15 \pm 0.26$ mN/m.

The adsorption coverage f over temperature can be therefore calculated with Eq. 5.24. At room temperature (25 °C), the equilibrium adsorption coverage f for Teflon AF1600 is 0.12, which is consistent with earlier findings from the literature[16, 188, 189, 191]. These studies have reported adsorption coverages for hydrophobic materials in the range of 0.1 to 0.18 at room temperature. It should be noted that the adsorption coverage decreases as the temperature increases. At temperatures higher than 50 °C the coverage approaches zero.

As discussed in Chapter 2.1.1 and supported by our results from the previous sections, CA hysteresis can be attributed to two distinct factors: the temperature-dependent adsorption contribution and the temperature-independent friction force. The variable friction force allows the CA to vary between the advancing and receding limits, as shown in Fig. 5.8. Instead of using the equation of solid surface tension described by adsorption coverage f and the energy of a fully occupied adsorption area e (Eq. 5.18), a parameter, the adsorption contribution F_{ad}, is introduced to represent the solid energy difference between an adsorption-free solid state and an equilibrium adsorption-desorption solid state at isotherm condition. In the following, an approach is presented to describe how the friction force (F_{f}) and the adsorption contribution (F_{ad}) contribute to the CA limits and CA hysteresis.

In the case of the advancing CA limit, the triple line moves in the direction of the γ_{sa} (dry surface), as shown in Fig. 5.8(left). Therefore, the advancing CA (θ_{adv}) is determined by the three interface tensions as well as the F_{fmax} in the direction of γ_{sl}. In the case of receding CA limit, the triple line moves in the direction of the γ_{sl} (previously water-covered area). Consequently, the force equilibrium for determining the receding CA (θ_{rec}) is affected by both F_{fmax} and F_{ad}, see Fig. 5.8(right).

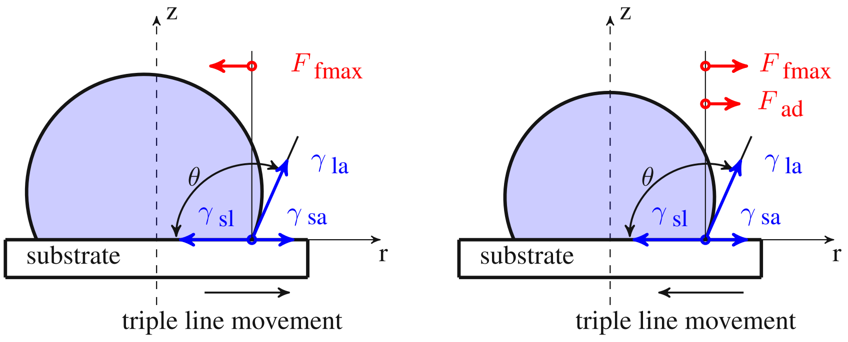

Fig. 5.8: Illustration of force equilibrium at the triple line for advancing CA (left) and receding CA (right).

The θ_{adv} and θ_{rec} are written as

$$\gamma_{\mathrm{la}} \cdot \cos\theta_{\mathrm{adv}} = \gamma_{\mathrm{la}} \cdot \cos\theta_{\mathrm{Y}} - F_{\mathrm{fmax}}, \tag{5.25}$$

and

$$\gamma_{\mathrm{la}} \cdot \cos\theta_{\mathrm{rec}} = \gamma_{\mathrm{la}} \cdot \cos\theta_{\mathrm{Y}} + F_{\mathrm{fmax}} + F_{\mathrm{ad}}, \tag{5.26}$$

respectively.

The θ_{Y} refers to Young's CA, which is only determined by interface tensions, equalling the initial CA (θ_{init}). Therefore, Young's CA as a function of temperature, $\theta_{\mathrm{Y}}(\mathrm{T})$, is approximated according to Eq. 5.22,

$$\cos\theta_{\mathrm{Y}}(T) = -\frac{e}{\gamma_{\mathrm{la}}(T)}, \tag{5.27}$$

where $e = 37.15$ mN/m and the $\gamma_{\mathrm{la}}(T)$ is the temperature-dependent liquid-air interface tension from literature[192]. The temperature-independent friction force limit F_{fmax} and the temperature-dependent adsorption contribution F_{ad} are experimentally determined and written as,

$$F_{\mathrm{fmax}} = 3.15 \text{ mN/m}, \tag{5.28}$$

and

$$F_{\mathrm{ad}}(T) = F_{25} \cdot (1 - \alpha \cdot (T - T_{25})), \tag{5.29}$$

with the parameter values $F_{25} = 4.95$ mN/m, $\alpha = 0.0182$ (1/K), and $T_{25} = 25\,^{\circ}\mathrm{C}$.

In summary, with the quantified F_{fmax}, $F_{\mathrm{ad}}(\mathrm{T})$, and the $\theta_{\mathrm{Y}}(\mathrm{T})$ (Eqs. 5.28, 5.29 and 5.27), the θ_{adv} and θ_{rec} can be calculated in a straightforward in the temperature range between 20°C and 80°C by the force equilibrium equations 5.25 and 5.26. It is worthwhile to mention that the equations of $\theta_{\mathrm{Y}}(\mathrm{T})$ as well as $F_{\mathrm{ad}}(\mathrm{T})$ are well justified at a temperature lower than 50 °C and are used as an approximation at higher temperatures. Furthermore, the CA hysteresis, which is calculated by $\cos\theta_{\mathrm{adv}} - \cos\theta_{\mathrm{rec}} = -\frac{2 \cdot F_{\mathrm{fmax}} + F_{\mathrm{ad}}}{\gamma_{\mathrm{la}}}$, reveals that Young's CA can not be simply represented as the mean value of θ_{adv} and θ_{rec}, $\theta_{\mathrm{Y}} = \frac{\theta_{\mathrm{adv}} + \theta_{\mathrm{rec}}}{2}$, or the mean value of the cosine of θ_{adv} and θ_{rec}, $\cos\theta_{\mathrm{Y}} = \frac{\cos\theta_{\mathrm{adv}} + \cos\theta_{\mathrm{rec}}}{2}$. Instead, Young's CA corresponds to the force equilibrium state, where both the adsorption and friction forces are zero, $F_{\mathrm{ad}} = F_{\mathrm{f}} = 0$.

5.6 Summary

In this chapter, the CAs results measured at different conditions are presented:

- the CAs as a function of temperature.
  The initial CA, θ_{init} (also Young's CA) on Teflon AF1600 is almost constant over temperature, slightly changes from 121.1 to 122.9 ° when the temperature varies from 20 to 80 °C;
  The receding CA θ_{rec} shows a significant increase from 113.3 to 119.7 °.

- the CAs on the water-adsorbed surface at different temperatures.
  CA values of 116.1, 117.2 and 117.7° at T=20, 25 and 30 °C, respectively.

In addition, a model is proposed to describe the solid surface tension by $\gamma_\mathrm{s} = \gamma_\mathrm{s0} + f \cdot e$, where f is the adsorption coverage and e is the energy of a fully occupied adsorption solid area. Depending on whether the solid surface is covered with water ($f = 1$), free from water ($f = 0$), or at an adsorption-desorption equilibrium at a specific temperature, γ_s can be γ_sl, $\gamma_\mathrm{sa}^\mathrm{init}$, or $\gamma_\mathrm{sa}^\mathrm{rec}$.

Based on these results, the Friction-Adsorption model (FA model) is introduced to describe the CA on the Teflon AF1600 surface. This model describes that apart from the interface tensions, γ_sl, γ_la, and γ_sa, two other important contributions should be taken into account for a precise CA determination:

- temperature-independent friction force,
  $F_\mathrm{f} \leq F_\mathrm{fmax} = 3.15\ \mathrm{mN/m}$,
- temperature-dependent adsorption contribution,
  $F_\mathrm{ad}(T) = F_{25} \cdot (1 - \alpha \cdot (T - T_{25}))$ (see Eq. 5.29).

The F_f can vary between the limit F_fmax in both directions of γ_sl and γ_sa, while the F_ad always acts in the direction of γ_sa. How those contributions affect the CA determination, is depending on the triple line movement:

- for advancing CA, the limit of friction force F_fmax contributes to CA determination,
  $\gamma_\mathrm{la} \cdot \cos\theta_\mathrm{adv} = \gamma_\mathrm{la} \cdot \cos\theta_\mathrm{Y} - F_\mathrm{fmax}$;
- for receding CA, both the limit of the friction force F_fmax and adsorption contribution F_ad should be taken into account,
  $\gamma_\mathrm{la} \cdot \cos\theta_\mathrm{rec} = \gamma_\mathrm{la} \cdot \cos\theta_\mathrm{Y} + F_\mathrm{fmax} + F_\mathrm{ad}$.

Due to the variable friction force F_f, the CA can vary between the advancing CA and receding CA.

All in all, the author points out that the CA variation on hydrophobic materials, particularly Teflon AF1600, is attributed to a temperature-independent friction-like force (F_f) and temperature-dependent water adsorption (F_ad). By considering these factors, we gain a more comprehensive understanding of the wetting behavior of hydrophobic surfaces and develop more accurate control of the CAs.

"

Chapter 6

Surface modification of Teflon AF1600

Contents

Some sections of this chapter were previously published in the paper titled "Characterization of Surface Modifications in Oxygen Plasma-Treated Teflon AF1600"[193].

6.1 Introduction

As introduced in Chapter 2, Teflon AF1600 is an ideal candidate for various applications due to its exceptional properties, such as high-temperature stability[115], excellent chemical resistance, and optical characteristics[194], along with a low surface energy[137].

To modify the surface properties of polymers, such as enhancing wettability for bonding or decreasing wettability for self-cleaning purposes, plasma treatment is a widely employed method, in addition to techniques like imprinting/embossing or layer deposition[31–40]. However, there are few studies addressing the modification of surface properties of Teflon AF1600, thus limiting the exploration of its full potential. Sabbatovskii et al. conducted low-pressure argon (Ar) plasma treatment of Teflon AF materials and the results revealed a hydrophilic surface[195]. Cho, Wallace, and Files-Sesler investigated the etching rate of Teflon AF by Ar, O_2, and CF_4/O_2 plasma, and the results showed enhanced wettabilities[196].

In addition to the limited studies of surface treatments for Teflon AF1600, the investigation of wettability through CA measurements on roughened and structured surfaces following plasma treatment presents a unique set of challenges, adding to the limited understanding of the altered surface properties of Teflon AF. In theoretical predictions, two fundamental equations are commonly employed: the Wenzel equation, introduced by Wenzel in 1936[18], and the Cassie-Baxter equation, proposed by Cassie and Baxter in 1944[17]. The Wenzel equation is utilized to describe the CA when a droplet completely wets a rough solid surface. In contrast, the Cassie-Baxter equation is employed when a droplet only partially wets a solid surface. However, these equations come with specific limitations and uncertainties. One notable challenge is that both the Wenzel and Cassie-Baxter equations require parameters derived from microscopic surface topography, which can be challenging to accurately determine. Furthermore, the validity of these equations has been a subject of debate in the literature, owing to various misleading explanation attempts and interpretations. More details about these equations and more discussions about their limitations and uncertainties can be found in Chapter 2.1.2.

In this work, oxygen plasma treatment was applied to modify the surfaces of Teflon AF1600. The resulting surface properties are systematically investigated and presented in this Chapter. In addition, the proposed Friction-Adsorption (FA) model, introduced in Chapter 5, is applied to describe the CA on these modified surfaces, where no parameters are required to quantify the structure-specific contact area. For comparison, photolithography was also applied to create regular structures on the surface. The resulting surface properties are additionally presented and discussed.

6.2 Plasma treatment

Plasma treatment of polymers results in two mechanisms: removal of the polymer and/or grafting of new species on the surface[176]. One common goal for plasma treatment is grafting new functionalities into the sample surfaces to increase the wettability[196, 197]. Another use is to modify the surface by creating structures during the material removal e.g. nanotextures in fluorinated ethylene propylene (FEP)[33], nano-pillars in FEP[34], nano-fibreillars in poly(ethylene terephthalate) (PET)[35, 40, 198], needle-like and nano-fiber structures in PTFE[36, 39], crown-shaped bumps in PTEF[37] and so on.

In this work, the author investigated the surface modifications of Telfon AF1600 by oxygen plasma with varied procedure parameters: treatment time, chamber pressure, applied power, and gas flow rate. The experimental process is presented in Chapter 3.3.1. In the following sections, the resulting properties, including thickness, surface topography, chemical changes, and wetting properties are presented and discussed.

6.2.1 Oxygen plasma treatment

Teflon AF1600 with a film thickness of 1.4 µm is used for this study. The fabrication details are reported in Chapter 3.2.1. The parameters for conducting the oxygen plasma treatment, plasma time, power, pressure, and gas flow rate are shown in Table 6.1.

6.2.1.1 Material Removal

The result of etched thickness is illustrated in Fig. 6.1. The result shows that the etched depth is proportional to the applied plasma energy, which is the product of time and power, as shown in Fig. 6.1(a), and independent of the oxygen gas flow rate and pressure (Fig. 6.1(b)).

sample	pressure[mTorr]	gas flow rate[sccm]	power[W]	time[s]	plasma energy [kJ]
T1	20	20	100	10	3
T2	20	20	100	20	3
T3	20	20	100	30	3
T4.5	20	20	100	45	4.5
T6	20	20	100	60	6
T8	20	20	100	80	8
T9	20	20	100	90	9
T12	20	20	100	120	12
P4.5	20	20	150	30	4.5
P6	20	20	200	30	6
P7.5	20	20	250	30	7.5
P9	20	20	300	30	9
P12	20	20	400	30	12
G3-30	20	30	100	30	3
G3-40	20	40	100	30	3
G6-30	20	30	100	60	6
G6-40	20	40	100	60	6
Pr3-30	30	20	100	30	3
Pr3-40	40	20	100	30	3
Pr6-40	40	20	100	60	6
E5	20	20	50	100	5
E6	20	20	50	120	6
E7	20	20	50	140	7
E8	20	20	400	20	8

Tab. 6.1: Oxygen plasma treatment on Teflon AF1600. The samples are named T, P, G, Pr, and E, representing the experimental series of varying etching time, power, gas flow rate, pressure, and plasma energy, respectively. The plasma energy is calculated by $time \cdot power$. The first number after the alphabet represents the plasma energy with the unit of kJ. The second number (after -) represents the pressure or gas flow rate. For instance, Pr3-30 means the sample treated by 3 kJ and pressure of 30 sccm in the experimental series of varying pressure.

6.2.1.2 Surface topography

Typical SEM images for surfaces treated by different plasma energies are shown in Figs. 6.2 and 6.3. The corresponding results from AFM analyses are illustrated in Fig. 6.4. These results reveal that the oxygen plasma treatment significantly modified the surface and induced nanoscaled features. Again, these features are mainly dependent on the plasma energy (Fig. 6.3) while the gas flow rate and chamber pressure do not play a role (Fig. 6.2).

For surfaces treated with a low plasma energy of 1 kJ, the created surface structures are too minuscule to be observed through SEM. Nevertheless, AFM measurements depict the formation of pillar-like structures on this surface, as illustrated in Fig. 6.4(b). As the plasma

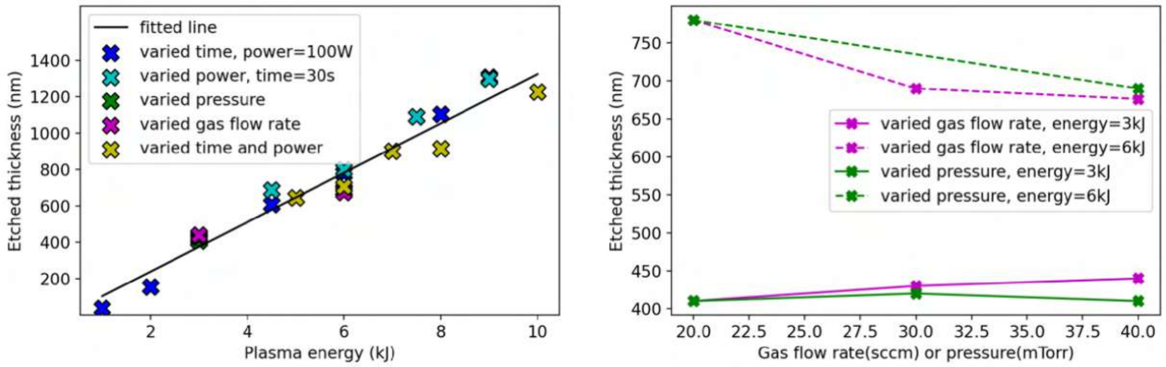

(a) (b)

Fig. 6.1: (a)The etched thickness of Teflon AF1600 after oxygen plasma etching as a function of plasma energy ($power \cdot time$); (b)The etched thickness as a function of the gas flow rate and the chamber pressure with a treatment time of 30 s and a plasma power of 100 W.

energy escalates to 6 kJ, the pillar-like structures increase both in dimension and height, evident in the SEM images (Fig.6.3(b)-(f)) and AFM images (Fig.6.4(c)-(e)). Beyond this level of plasma energy, the nanoscaled pillar-like structures undergo a transformation into fiber-like structures, as depicted in the SEM images (Fig. 6.3(g)-(i)). Unlike the needle-like structures, the fiber-like structures exhibit a few undercuts, complicating accurate AFM measurements. Consequently, AFM images are exclusively obtained from samples treated with energy up to 6 kJ.

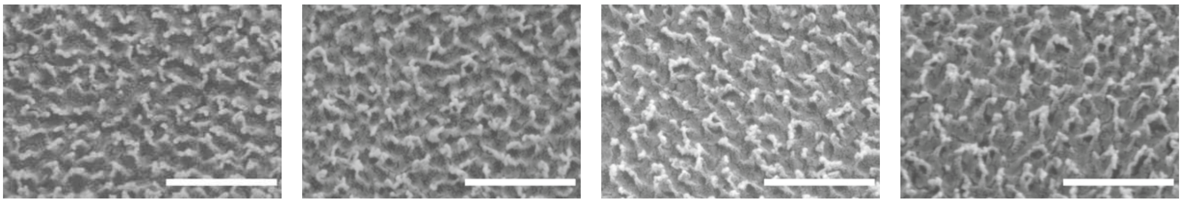

(a) 60 s, 100 W, 20 mTorr, 20 sccm. (b) 30 s, 200 W, 20 mTorr, 20 sccm. (c) 60 s, 100 W, 20 mTorr, 40 sccm. (d) 60 s, 100 W, 40 mTorr, 20 sccm.

Fig. 6.2: The SEM images of treated sample at plasma energy of 6 kJ by varied parameters. All images are taken by tilting the samples by 30°. The length of the white scale bar is 500 nm.

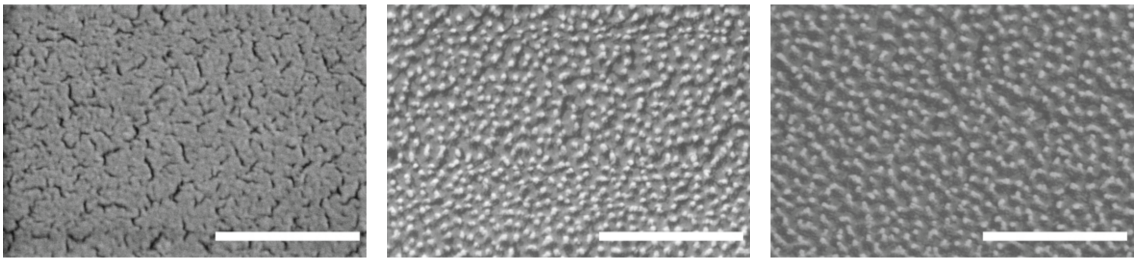

(a) 1 kJ (b) 2 kJ (c) 3 kJ

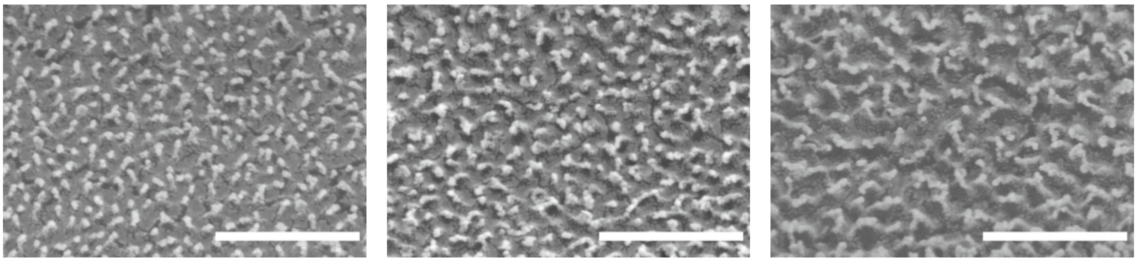

(d) 4.5 kJ (e) 5 kJ (f) 6 kJ

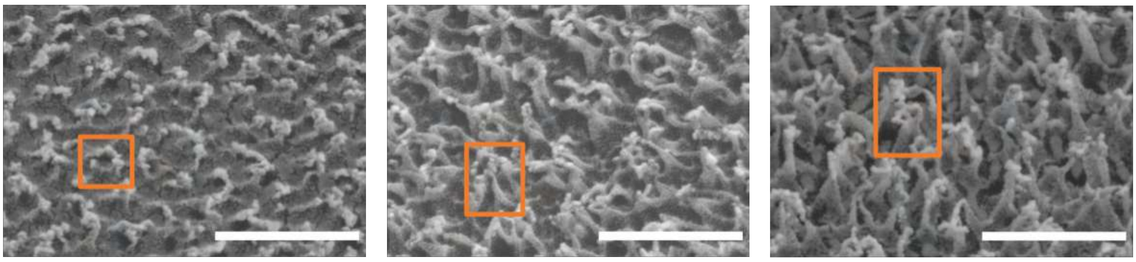

(g) 7 kJ (h) 8 kJ (i) 9 kJ

Fig. 6.3: SEM images of modified Teflon AF1600 surface by oxygen plasma treatment with varied plasma energy. All images are taken by tilting the samples by 30°. The length of white bar in each image represents 500 nm.

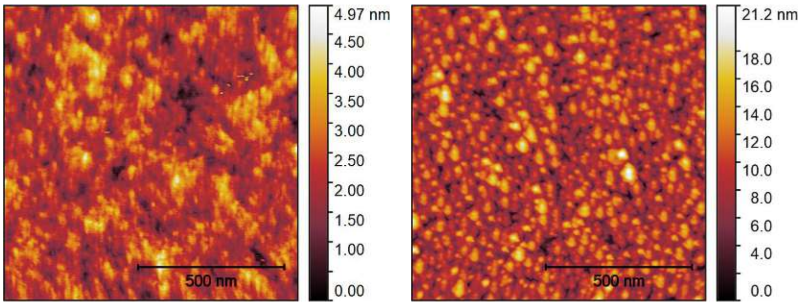

(a) pristine (b) 1 kJ

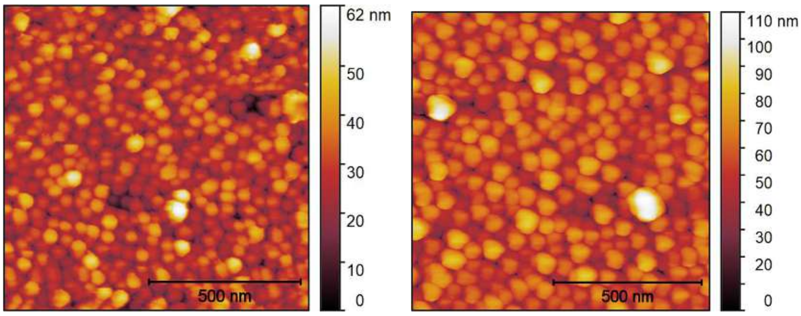

(c) 3 kJ (d) 4.5 kJ

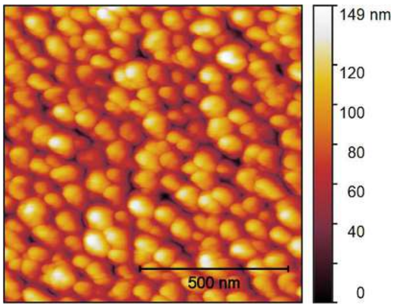

(e) 6 kJ

Fig. 6.4: The AFM images of (a) untreated surface and plasma treated Teflon AF1600 surface with plasma energy of (b) 1 kJ, (c) 3 kJ, (d) 4,5 kJ, and (e) 6 kJ.

Gwyddion[199] is employed to analyze AFM images for the determination of root mean square roughness (R_{RMS}) and the solid area ratio. The latter parameter represents the ratio of actual surface area to the projected surface area. The outcomes, presented in Fig.6.5, illustrate a notable increase in R_{RMS} resulting from oxygen plasma treatment. Specifically, the R_{RMS} rises from 0.7 ± 0.09nm on the untreated surface to 18.7 ± 3.12 nm for the surface treated with 6 kJ of plasma energy. Moreover, the area ratio exhibits a significant elevation with increasing plasma energy. The pristine surface has an area ratio of 1.006 ± 0.002, while for the surface treated with 6 kJ of plasma energy, it correspondingly increases to 1.867 ± 0.153.

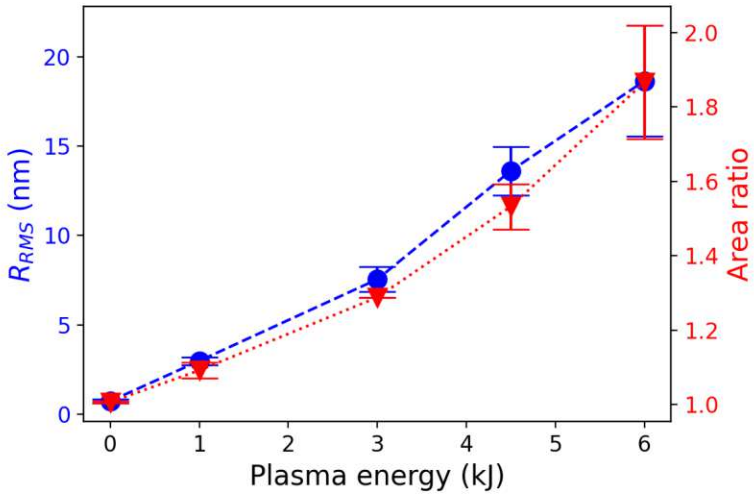

Fig. 6.5: RMS roughness and area ratio of actual surface area to the projected surface as a function of plasma energy. Data are obtained by analysis of AFM images with a scan area of 1 × 1 µm by Gwyddion.

6.2.1.3 Wetting property

The wetting property of a surface is determined by the advancing and receding CA, as described in Chapter 2.1.1. The results of the wetting property of plasma-treated Teflon AF1600 are plotted as a function of plasma energy in Fig. 6.6. The results show that the plasma-treated surfaces exhibit three different wetting behaviors:

(1) low advancing and zero receding CA,

(2) super high advancing but zero receding CA,

(3) super high advancing and high receding CA.

Here, super high refers to a CA larger than 150 °, while high and low refer to values higher and lower than the CAs observed on pristine surfaces.

When the applied plasma energy is low (< 1 kJ), the advancing CA decreases to $115.5 \pm 0.45°$ due to oxygen plasma treatment in comparison to the pristine surface value of $124.1 \pm 0.35°$. Notably, the observed receding CA is 0°, indicating that the triple line sticks to the solid surface, and the solid-liquid interface area remains unchanged while the CA continuously decreases. This wetting behavior is characterized as low advancing and zero receding CA. As the plasma energy increases to the range of 2 to 3 kJ, there is a significant augmentation in the advancing CAs, reaching 157.0 ± 0.31 ° and $156.3 \pm 0.60 - 163.3 \pm 0.46$ °. However, a receding CA of 0° is observed on these surfaces, categorizing them as exhibiting super high advancing but zero receding CA behavior. As the plasma energy continues to rise, the advancing CA slightly increases ($\theta_{\mathrm{adv}} > 160°$), and a receding CA larger than 118.5 ± 0.74 °is measured, which is higher than that on the pristine surface ($113.3 \pm 0.23°$). This wetting behavior is characterized as super high advancing and high CA.

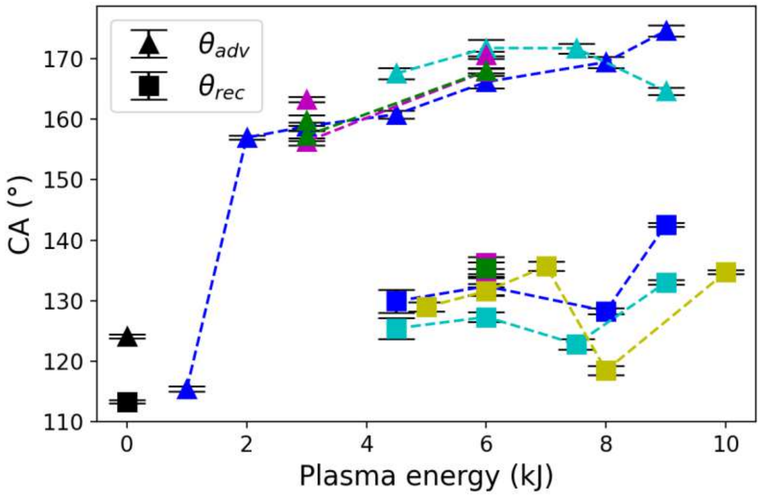

Fig. 6.6: Advancing (triangle points) and receding CA (rectangular points) as a function of plasma energy at $T = 25\,°\mathrm{C}$. The points in black represent the θ_{adv} and θ_{rec} on pristine Teflon AF1600[137]. Points in other colors represent CAs on the oxygen plasma-treated surface with different treatment parameters and the color coding is identical to that shown in Fig. 6.1.

Commonly, the Cassie[17] and Wenzel[18] equations are used to describe the CA on structured and roughened surfaces. The details about Cassie and Wenzel's equation are presented in Chapter 2.1.2.

In the following, the application of Cassie-Baxter and Wenzel equations to the surfaces that exhibit super high advancing CA and high receding CA are discussed. These surfaces are obtained by treating Teflon AF1600 with plasma energy larger than 4 kJ.

When measuring the advancing CA, the droplet exhibits a Cassie state, characterized by an advancing CA consistently exceeding 160°. Notably, this value remains independent of the plasma energy, and consequently, unaffected by variations in the resulting structure size and the corresponding solid area fraction (f_{solid}). This finding aligns with observations made by Kwon et al.[200], Öner and McCarthy[67], and is corroborated by the author's measurements of advancing CA on regularly micro-structured surfaces in this study (Chapter6.3). The structure-independent high value of θ_{adv} is attributed to the presence of discrete structures, as discussed by [78] and [200]. These discrete structures, such as pillar-like and fiber-like features, create a discontinuous contact between the liquid droplet and the solid surface, separated by several local solid-air contact interfaces or air pockets. This discontinuity results in a substantial energy barrier that must be overcome when the triple line moves across these discontinuous pillar- and fiber-like structures. Consequently, the advancing CA remains high irrespective of the size and density of the surface structures, and its behavior cannot be accurately predicted by the Cassie-Baxter equation.

A substantial difference of approximately 30° between the receding and advancing CAs is evident, as depicted in Fig. 6.6, signifying distinct wetting states. On surfaces featuring pillar-like structures, the liquid droplet wets from the top, flowing along the side walls of the pillar structures and the pocket areas. Consequently, a continuous solid-liquid contact is established, indicating an equilibrium Wenzel state. The receding CA in the

Wenzel state is calculated by Eq. 2.3 with the receding CA on the pristine surface (113.3 °) and the area fraction value obtained from AFM analysis. The calculated receding CA on surfaces treated by plasma energies with 4.5 and 6 kJ is 127.2 and 137.6 °, revealing consistent results shown in Fig. 6.6. Additionally, it is important to note that the AFM scanning area is 1×1 µm, which is substantially smaller than the solid-liquid contact area with a radius of $1 - 1.3$ mm.

When the structures are more fiber-like (plasma energy > 6 kJ), obtaining precise AFM images and accurately measuring the area fraction becomes challenging due to the presence of undercuts. Consequently, the application of the Wenzel equation for predicting the receding CA becomes unfeasible under these conditions.

Next, the previously proposed model, the Friction-Adsorption (FA) model[137, 139], is employed to describe the advancing and receding CA on the plasma-treated surfaces. Details of the Friction-Adsorption model are presented in Chapter 5. According to the FA model, CAs are determined by surface tensions, temperature-independent friction force F_f, and temperature-dependent adsorption $F_\mathrm{ad}(\mathrm{T})$.

A proper application of the FA model is based on the assumption that the oxygen plasma treatment predominately induces topography modification so that the friction force F_f is enhanced, while the adsorption contribution F_ad stays unchanged. A similar approach is suggested by Vandencasteele, Merche, and Reniers, who conducted XPS experiments on oxygen plasma-treated PTFE. The results revealed that oxygen plasma treatment did not graft new species on the surface of PTFE and the hydrophobicity is enhanced by the increased roughness[176]. To validate the assumption, FTIR as well as XPS experiments on some selected samples are conducted. These samples involve pristine surface and samples treated by oxygen plasma with the energy of 1, 2, 6 kJ, which represents the different wetting behaviors: original wetting behavior, low advancing, and zero receding CA, super high advancing and zero receding CA, and super high advancing and high receding CA, respectively.

In the next section, the FTIR and XPS results are presented and followed by the detailed application of the FA model.

6.2.1.4 Chemical analysis

The XPS and FTIR characterization methods are conducted to investigate the surface chemical changes of Telfon AF1600 after oxygen plasma treatment. These methods are introduced in Chapter 4.6.

The FTIR results of pristine and oxygen plasma treated polymer are shown in Fig. 6.7. These results indicate no functional group changes by oxygen plasma treatment concerning the bulk material.

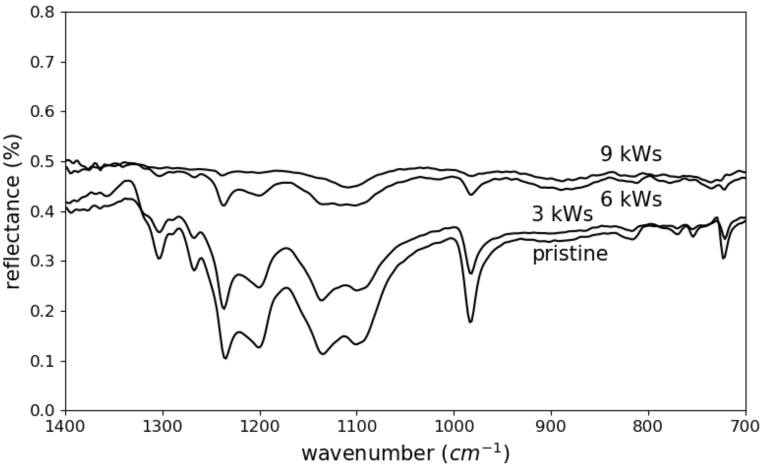

Fig. 6.7: FTIR results of pristine and oxygen plasma treated surfaces.

The results of the XPS investigation are shown in Figs. 6.8 and 6.9. The C1s spectra of the pristine Teflon AF1600 surface, depicted in Fig.6.8(a) (top), exhibit four distinct chemical states of carbon atoms: CF_3, CF_2, O-C-F, and O-C-O at binding energies of 293.8, 291.8, 291.3, and 290.6eV, respectively. The observed intensity ratios of 2:1:2:1 for CF_3:CF_2:O-C-F:O-C-O align with the expected ratios based on the chemical formula of Teflon AF1600, as illustrated in Fig. 2.10. Furthermore, the presence of peaks at 289.1 and 287.9 eV corresponds to O-C=O and C=O[201, 202], suggesting surface contamination and/or polymer deterioration resulting from exposure to X-rays[115, 176]. Following oxygen plasma treatment, the components of Teflon AF1600 remained present in the aforementioned ratio, while an increase in the quantity of oxygen was noted. At binding energies of 286.4 and 285.1 eV, the presence of C-O and C-C/C-H is characterized[176]. This escalation can be attributed to enhanced surface modification stemming from the increasing plasma energy.

Fig. 6.8(b) shows the O1s spectra. Two components labeled CO1 and CO2, are assigned to CO groups (C=O, C-O, O-C=O), which are similar to the deconvolution of the C1s signal. Additionally, a minor presence of titanium oxide is detected, originating from the Ti primer used in the film spin-coating process (refer to Chapter 3).

The F1s spectra, as shown in Fig.6.9(a), do not exhibit significant differences between the pristine and plasma-treated samples. This result suggests the unchanged presence of the functional groups of Teflon AF1600 (refer to Fig.2.10) following oxygen plasma treatment. This consistency aligns with the observation that the ratio of CF_2/O-C-O/O-C-F to CF_3 in the C1s spectra remains constant.

The results of the quantification analysis are presented in Table 6.2, indicating a slight decrease in the fluorine (F) concentration, coupled with a marginal increase in the oxygen (O) concentration, both remaining below 4%. A comparable XPS result for PTFE treated with oxygen plasma, as reported by Vandencasteele and Reniers, also demonstrates a minor increase in O concentration (less than 5

Given the XPS experimental findings presented in this study, along with similar results from chemical analyses of plasma-treated fluoropolymers[176, 201], it is reasonable to infer that oxygen plasma treatment primarily induces material etching, thereby modifying the surface topography.

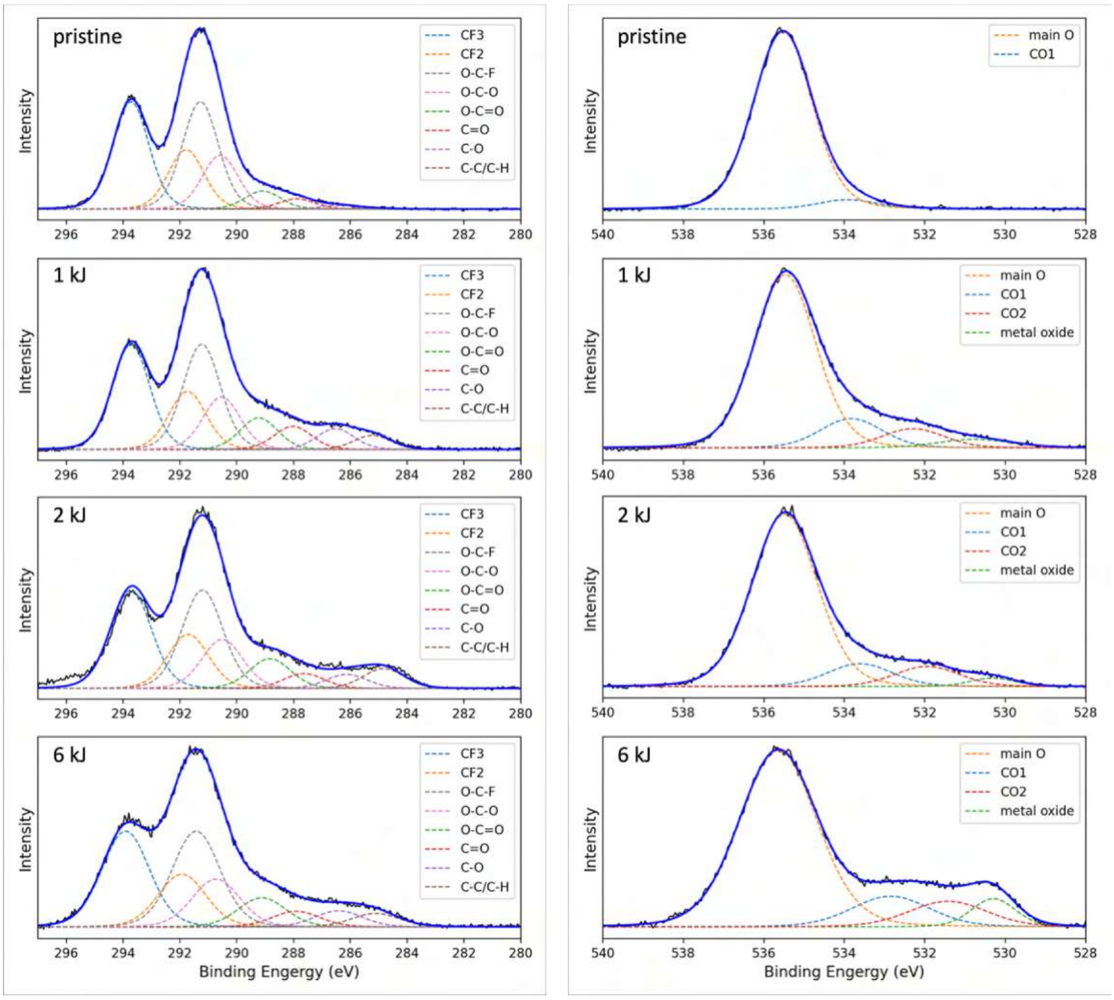

(a) C1s

(b) O1s

Fig. 6.8: (a) C1s, (b) O1s XPS. From top to bottom: pristine Teflon AF1600, and plasma treated surface by oxygen plasma energy of 1, 2, and 6 kJ, respectively.

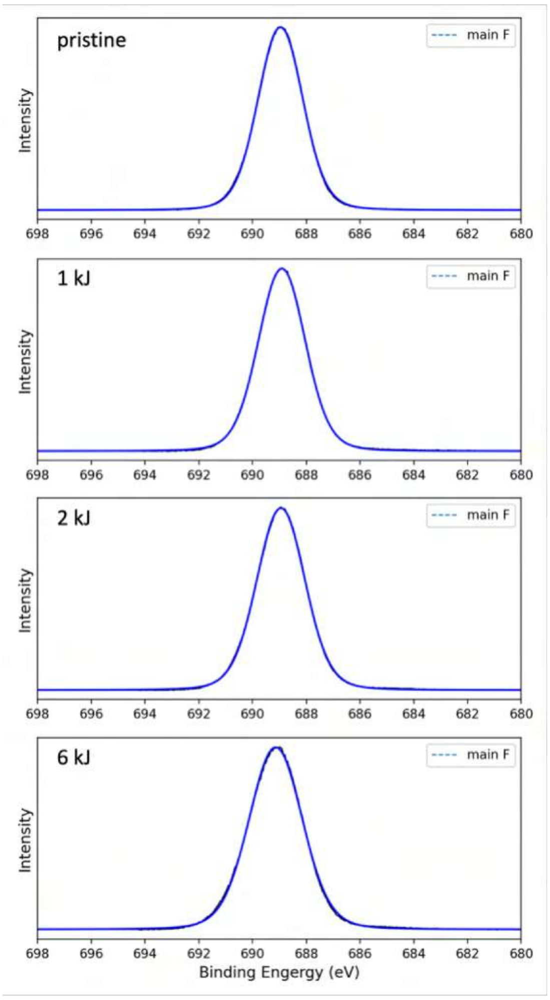

(a) F1s

Fig. 6.9: (a) F1s XPS. From top to bottom: pristine Teflon AF1600, and plasma treated surface by oxygen plasma energy of 1, 2, and 6 kJ, respectively.

sample	at%C	at%F	at%O
pristine	41.1	48.3	10.6
T1	41.5	46.1	12.4
T2	41.4	46.1	12.5
T6	41.2	44.0	13.9

Tab. 6.2: Surface composition of pristine as well as plasma treated Teflon AF1600. T1, T2, and T6 represent the sample treated with oxygen plasma energy of 1, 2, and 6 kJ.

6.2.1.5 FA model on rough surfaces

As discussed earlier, the primary effect of oxygen plasma treatment is material removal and the modification of surface topography. Consequently, it is assumed that the friction force limit (F_{fmax}) is predominantly altered, while the change in F_{ad} is considered negligible.

According to the FA model, the advancing and receding CA are dependent on liquid-air interface tension γ_{la}, friction force limit F_{fmax} and Young's CA θ_{Y}[137, 139]. Details are introduced in Chapter 5.5.

The F_{fmax} on the pristine surface is experimentally determined as $F_{\mathrm{fmax}} = 3.15 \pm 0.19$mN/m[137, 139]. θ_{Y} is described by the force equilibrium at the triple line by the three interface tensions[2].

Combining the advancing and receding CA equations (Eqs. 5.25 and 5.26 from Chapter 5.5), we get

$$\gamma_{\mathrm{la}} \cdot (\cos\theta_{\mathrm{adv}} - \cos\theta_{\mathrm{rec}}) + F_{\mathrm{ad}} = -2 \cdot F_{\mathrm{fmax}}. \tag{6.1}$$

It is observed that the F_{fmax} is independent of temperature, while all other parameters are temperature-dependent[137, 139]. Among these parameters, the liquid-air interface tension, γ_{la}(T), is well-known[192] and verified by some of our own experiments. Both θ_{adv}(T) and θ_{rec}(T) can be experimentally determined. The temperature-dependent F_{ad}(T) is assumed to be identical to that of pristine Teflon AF1600 as Eq. 5.29.

To determine the temperature-independent F_{fmax} on plasma-treated surfaces, CA measurements at different temperatures on representative plasma-treated surfaces are conducted. The results of θ_{adv}(T) and θ_{rec}(T) are shown in Fig. 6.10, indicating a constant trend with temperature in the investigated range of 25 to 80 °C. Based on these temperature-dependent factors, the temperature-independent F_{fmax}, is calculated. Fig. 6.11 depicts the results of $\gamma_{\mathrm{la}} \cdot (\cos\theta_{\mathrm{adv}} - \cos\theta_{\mathrm{rec}})$ (dashed line), as well as the calculated value of $\gamma_{\mathrm{la}} \cdot (\cos\theta_{\mathrm{adv}} - \cos\theta_{\mathrm{rec}}) + F_{\mathrm{ad}}$, which is theoretically equal to $-2 \cdot F_{\mathrm{fmax}}$ (solid line), as a function of temperature. The results distinctly indicate a significant enhancement in the friction force limit (F_{fmax}) following plasma treatment compared to that observed on the pristine surface. For nanoscaled pillar-like structures presented surfaces, F_{fmax} maintains a consistent trend with a slight variation: 9.7 ± 0.49 and $9.1 \pm 0.37, \mathrm{mN/m}$ for surfaces treated with 5 and 6 kJ, respectively. However, the transformation of the resulting structures from pillar-like to fiber-like, achieved by plasma treatment with an energy of 7 kJ, leads to a reduction in F_{fmax} to 7.2 ± 0.36mN/m. A further increase in plasma energy to 8 kJ results in a remarkable rise in the friction force limit (F_{fmax}) to 15.7 ± 0.43mN/m, believed to be due to the more predominant pinning sites.

The F_{fmax} results are further justified by EWOD experiments and are presented in Chapter 7.4.3.

6.3 Photolithographic micro-structuring

The micro-structured superhydrophobic surface is fabricated by photolithography. Experimental details are shown in Chapter 3.3.2. The micro-structures are designed as cubic and hexagonal arranged pillars.

The dimensions of the designed microstructures are listed in Tables. 6.3 and 6.4. The diverse dimensions of the micro-structures result in a wide range of f_{solid} $(0.01 - 0.4)$ and f_{r} $(1.002 - 1.159)$, which are necessarily for using Cassie-Baxter and Wenzel equations (Eqs. 2.5 and 2.3) to describe the CAs. The results of the measured and calculated θ_{adv} and θ_{rec} are shown in Figs. 6.12 and 6.13. The θ_{adv} shows a high and constant value over

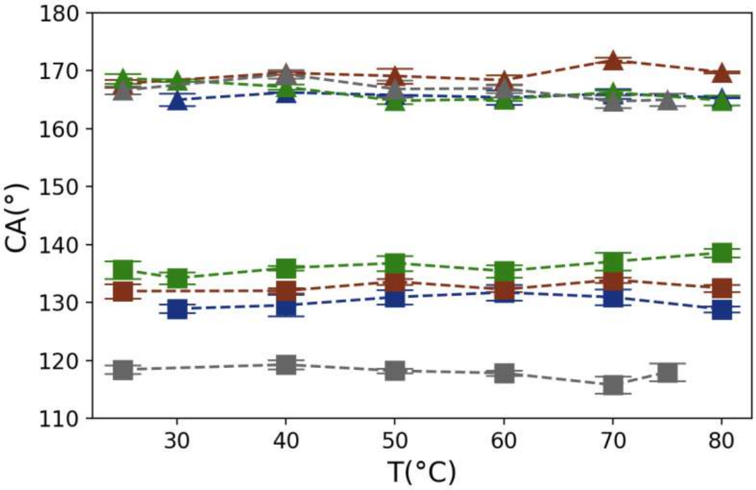

Fig. 6.10: The advancing (triangular points) and receding CAs (rectangular points) of Teflon AF1600 surfaces treated with plasma energies between 5 to 8 kJ as a function of temperature. (blue: 5 kJ, red 6 kJ, green 7 kJ, gray: 8 kJ). The dashed lines are a guide for the eyes.

the investigated range of f_{solid} and does not follow the Cassie-Baxter equation. This is due to the discontinuous pillar structures[78, 200], as explained in the previous section, Chapter 6.2.1. The receding CA, however, could not be described by either Cassie or Wenzel equations, see Figs. 6.12 and 6.13.

sample name	a [µm]	b[µm]
C0203	2	3
C0205	2	5
C0208	2	8
C0303	3	3
C0308	3	8
C0404	4	4
C0406	4	6
C0408	4	8
C1050	10	50
C2050	20	50

Tab. 6.3: Dimensions of the cubic-arranged micro-pillars. a, b is the diameter of the pillars, and the distance between the two pillars, respectively.

6.4 Summary

In this chapter, the investigations of surface properties of Teflon AF1600 treated with oxygen plasma are introduced.

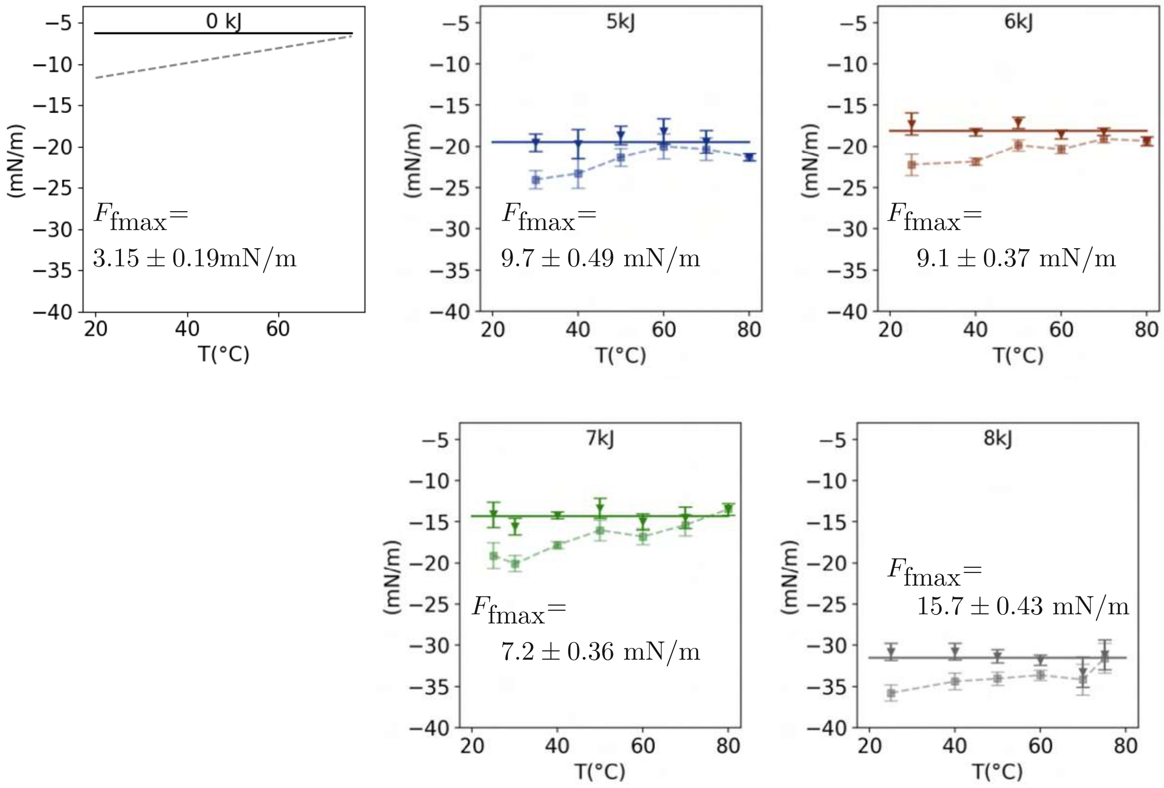

Fig. 6.11: Measurement results of $\gamma_{\text{la}} \cdot (\cos\theta_{\text{adv}} - \cos\theta_{\text{rec}})$ (dashed line) and calculated $-2 \cdot F_{\text{fmax}}$ (solid line) on surfaces treated with different oxygen plasma energies as a function of temperature. The experimental data on the pristine surface (0 kJ) can be found in reference paper [137].

The results reveal

- The plasma energy plays the determinant role for etched depth, CAs, as well as surface topography.
- Depending on the plasma energy, nanoscaled needle- ($\leq$ 6 kJ) and fiber-like (>6 kJ) structures are formed on the surface.
- Depending on the plasma energy, the treated surface exhibits different wetting behaviors: (1) low advancing and zero receding CA (<1 kJ), (2) super high advancing but zero receding CA (2-3 kJ), and (3) super high advancing and high receding CA (4.5 – 10 kJ).
- Cassie-Baxter equation fails to describe the advancing CAs both on plasma-treated and photolithographic structured surfaces due to the discontinuously presented structures.
- The receding CAs on pillar-like structures presented surfaces show agreement with the results calculated by the Wenzel equation, while for fiber-like structures Wenzel equation is not applicable due to the lack of knowledge of the area ratio.

sample name	a [µm]	b[µm]
H0202	2	2
H0204	2	4
H0206	2	6
H0212	2	12
H0216	2	16
H0404	4	4
H0408	4	8
H0416	4	16
H0425	4	25
H0508	5	8
H0510	5	10
H0603	6	3
H0606	6	6
H0607	6	7
H0612	6	12
H0624	6	24
H0808	8	8
H0816	8	16
H0832	8	32
H0840	8	40
H1005	10	5
H1020	10	20
H1040	10	50
H2020	20	20
H2040	20	40

Tab. 6.4: Dimensions of the hexagonal-arranged micro-pillars. a, b is the diameter of the pillar, and the distance between the two pillars, respectively.

- FTIR and XPS investigations reveal that the oxygen plasma treatment predominantly modifies the surface topography, and the surface functional groups stay constant.
- The FA model is applied to describe the advancing and receding CAs on plasma-treated surfaces by assuming that the oxygen plasma treatment predominantly modifies the surface topography and consequently the friction force limit F_{fmax}, while the F_{ad}, which associates with the surface chemical compositions, stayed unchanged as for the pristine surface.
- The advancing and receding CAs on plasma-treated surfaces exhibit a constant trend with temperature in the range of 25-80 °C.
- The friction force limit F_{fmax} is calculated based on the FA model as 9.73, 9.06, 7.17 and 15.72 mN/m for 5, 6, 7 and 8 kJ oxygen plasma treated surface, respectively, and are further justified by EWOD experiments. The EWOD results are presented in Chapter 7.4.3.

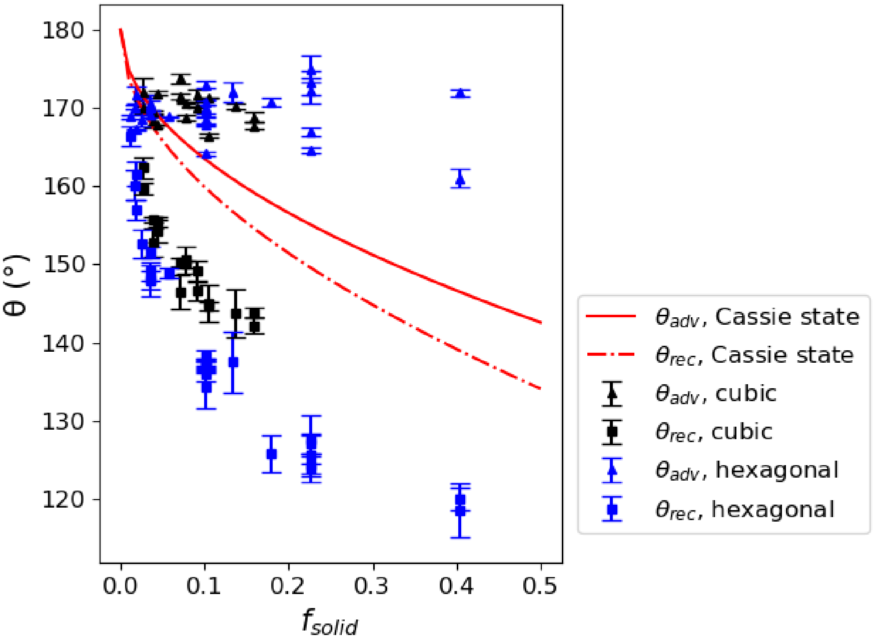

Fig. 6.12: The CAs as a function of f_{solid} for Cassie state.

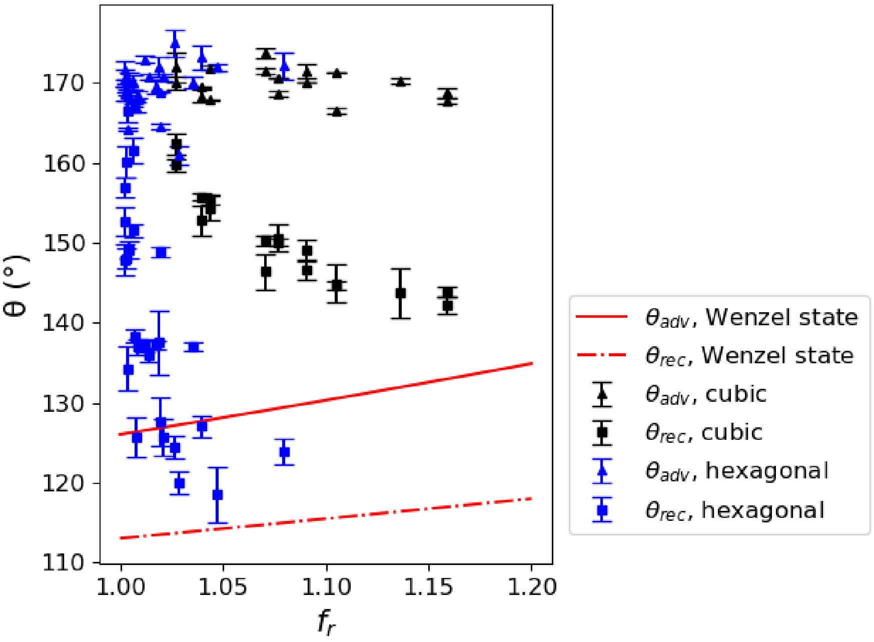

Fig. 6.13: The CAs as a function of f_{r} for Wenzel state.

Chapter 7

Eletrowetting on Teflon AF1600

Contents

Some sections of this chapter were previously published in the paper titled “Temperature-dependent electrowetting behavior on Teflon AF1600”[139].

7.1 Introduction

As introduced in Chapter 2.4, the EWOD effect is one of the most widespread techniques for controlling the CA between an electrolyte droplet and a dielectric surface due to the low energy consumption, as well as easy and fast manipulation of small liquid volumes[93, 139]. The EWOD technique has enabled numerous applications, including the generation, transportation, and mixing of small droplets in microfluidic devices [41–43], adjustable liquid lenses [43–48], and many others. According to the famous Young-Lippmann equation, which is introduced in detail in Chapter 2.4, the CA between the electrolyte and dielectric surface is determined by the corresponding interface tensions and the electric energy stored in the solid dielectric layer. However, similar to the CA measurements discussed in Chapter 5, the EW-CA is also prone to various material and ambient-related factors. Theses factors include surface roughness[13], chemical inhomogeneity[14], as well as water adsorption and temperature effects[15, 137].

Several works have been published to explore the EW response on materials with high CA variations/hysteresis[49–51]. In these studies, the EW response was investigated by increasing and decreasing droplet volume at a constant applied voltage to achieve the advancing and receding triple line as well as the corresponding CAs. Additionally, Reid, Merrill, and Thomas observed a stick-slip behavior when increasing the droplet volume during the EW experiments when a DC voltage was applied[51]. Moreover, the temperature is a crucial influence factor for the CA determination[52, 137], especially in the liquid lens application field, since the interface tensions, as well as the CA hysteresis, are temperature-dependent [137, 138].

In Chapter 5, the temperature-dependent CA is introduced, and the friction-adsorption (FA) model is proposed to describe CAs under both different triple line and temperature conditions. By using this model, the CA variation between the advancing and receding limit is interpreted by temperature-independent and temperature-dependent contribution factors. In this chapter, the proposed FA model is applied to describe the EW-CA on Teflon AF1600 as well. Finally, The results are presented and discussed in the following sections.

7.2 Modified equation for EW-CA

In Chapter. 5, the static CA is determined by the three interface tensions, γ_{sl}, γ_{la} and γ_{sa}, a temperature-independent friction-like force F_{f} ($\leq F_{\mathrm{fmax}} = 3.15$ mN/m), and a temperature-dependent contribution of adsorption on the dielectric surface $F_{\mathrm{ad}}(\mathrm{T})$ (Eq. 5.29), shown in Fig. 7.1. In this section, it is introduced how these two contributions affect the EW-CA in detail.

The vectorial force equilibrium at the triple line is reduced to the equilibrium of the horizontal radial components, while the vertical z-components are compensated by the substrate. With the additional force F_{el} due to the stored electric energy,

$$F_{\mathrm{el}} = c \cdot U^2/2 \quad , \tag{7.1}$$

the CA, θ, is described by:

$$\gamma_{\mathrm{la}} \cdot (\cos\theta - \cos\theta_Y) = F_{\mathrm{f}} + F_{\mathrm{ad}} + F_{\mathrm{el}} \quad . \tag{7.2}$$

In the initial, static equilibrium state (F_{f}=F_{ad}=F_{el}=0), Equation 7.2 gives the standard Young's CA, $\cos\theta_{\mathrm{Y}}$. The $\cos\theta_{\mathrm{Y}}$ is temperature dependent, and the dependency is described by Equation 5.27 in Chapter. 5.

The forces F_{el} and F_{ad} are always positive in sign, which means they are directed towards an increase in the base diameter in cases where their values are non-zero. The friction force F_{f} varies in the range between 0 and F_{fmax}, and can act in both directions, as shown in Fig. 7.1.

When applying a voltage on the droplet, an additional force, F_{el}, is introduced to the force equilibrium, which is compensated by the variable friction force up to its maximum value of F_{fmax}. As F_{el} ($\propto U^2$) increases, it drives the tripe line towards the dry dielectric surface with a zero adsorption contribution, $F_{\mathrm{ad}} = 0$, establishing the advancing triple line

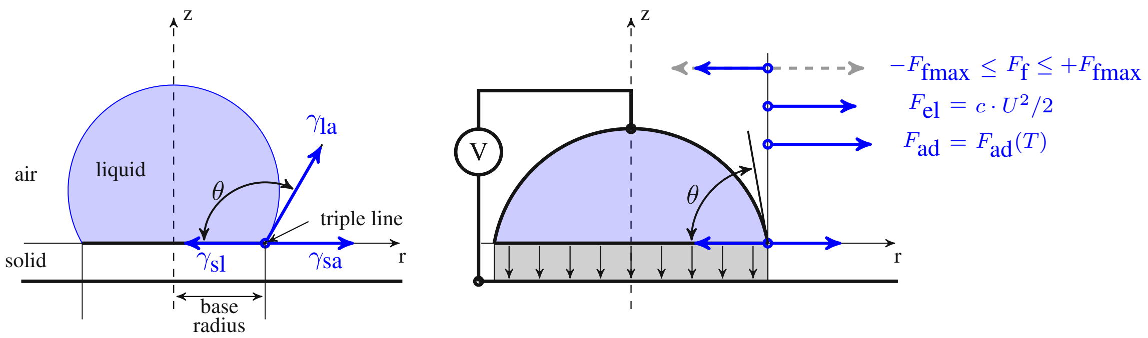

Fig. 7.1: Equilibrium of static forces at the triple line. Left: Young's CA equilibrium of interface tensions. Right: Additional forces due to friction F_f, adsorption contribution F_{ad}, and the electric energy F_{el}. The electric energy is stored in the gray-shaded dielectric layer below the droplet.

condition and the corresponding CA, θ_{adv}. According to Equation 7.2, θ_{adv} is described by:

$$\gamma_{la} \cdot \cos\theta_{adv} = \gamma_{la} \cdot \cos\theta_Y - F_{fmax} + F_{el}. \tag{7.3}$$

When the applied voltage and F_{el} begin to decrease, the triple line tends to move back across the dielectric surface previously covered by the droplet. Once the friction force F_f reaches its maximal value F_{fmax}, the receding triple line condition is established. The force equilibrium at the triple line is determined by F_{fmax} and the adsorption contribution F_{ad}, in addition to the interface tensions. The receding CA, θ_{rec}, is therefore written as:

$$\gamma_{la} \cdot \cos\theta_{rec} = \gamma_{la} \cdot \cos\theta_Y + F_{ad} + F_{fmax} + F_{el}. \tag{7.4}$$

Figure 7.2 summarizes the solutions of Eqs. 7.3 and 7.4 with our EWOD samples, i.e. 1.09 µm thick Teflon AF1600 with a characterized dielectric constant of 1.92 (details can be found in Chapter 4.3 and the following Chapter 7.3.1), and illustrates the advancing and receding CA.

Figure 7.2 reveals two different hystereses, namely the

- horizontal hysteresis: an applied voltage may not necessarily lead to a change in CA, because the resulting force from the stored electric energy (F_{el}) can be compensated by the friction force (F_f);
- vertical hysteresis: at a constant voltage, the CA can vary between advancing and receding CA, depending on the triple line condition.

A more detailed explanation of the two hysteresis loops can be found in Figure 7.3. The vertical lines in Fig. 7.3(a) represent the range of the CA hysteresis during EW performance at constant voltages, for instance, the CA can be manipulated by changing the droplet volume. In this work, the EW performance is conducted with a constant droplet volume. The variation between the advancing and receding CAs is solely caused by the applied voltage. Fig.7.3(b)(c) show the CA behavior for a positive voltage half-cycle. Specifically, when the voltage is increased from zero, the CA remains constant until the advancing CA limit is reached. In this constant CA regime, the force equilibrium is

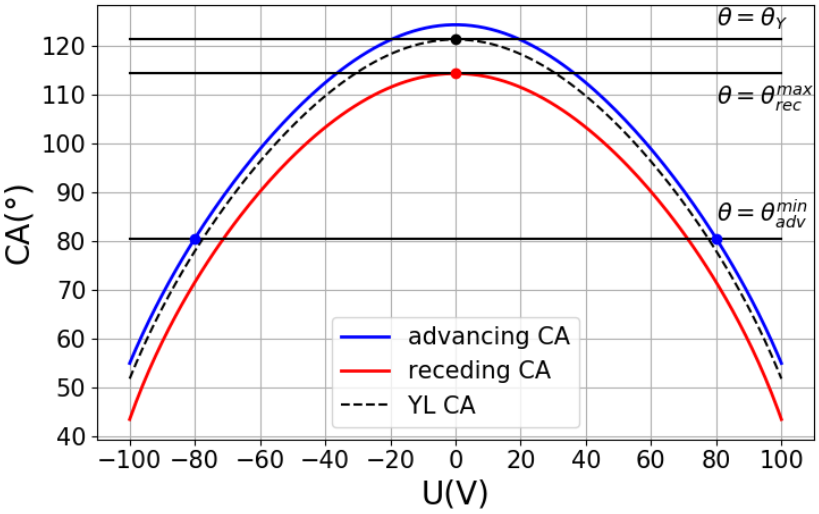

Fig. 7.2: Voltage dependence of the advancing (in blue) and the receding CA (in red) at a temperature of 30 °C according to the FA model. The limits of the friction-force F_f ($-F_{fmax} \leq F_f \leq +F_{fmax}$) and $F_{ad}(T)$ define the CA hysteresis range. The dashed line is calculated by the Young-Lippmann equation. The black point represents a droplet with a CA of θ_Y ($F_f = F_{ad} = F_{el} = 0$). The red point represents the maximal receding CA ($\theta_{rec}^{max} = \theta_{rec} \quad @ \quad U = 0\,V$). The blue points represent the minimal advancing CA (θ_{adv}^{min}) at the maximal applied voltage in this work, ±80 V.[139].

established additionally by the variable F_f and the increasing F_{el} (as described by Eq.7.2). As the voltage level is further increased, the CA moves along the advancing line (blue line in Fig.7.2) with the uniquely defined dependence $\theta(U)$ (Eq.7.3), accompanied by the movement of the triple line. When the voltage starts decreasing, the CA again stays constant as long as F_f and F_{ad} can compensate for the changing F_{el}. This constant CA regime is maintained until the receding CA limit is reached. From there on the CA follows the receding CA line (red line in Fig. 7.2), with $\theta(U)$ given by Eq. 7.4. For $U = 0\,V$, the maximum receding CA, θ_{rec}^{max}, is determined, which sets an upper limit that cannot be exceeded by any subsequent voltage changes.

7.3 Pre-investigations

To ensure reliable EWOD performance, the experimental setup must fulfill two requirements. First, it is essential that the properties of the EWOD devices remain unchanged during experiments to ensure long-term performance. This means that both the electrical and surface properties of the dielectric layer must remain stable throughout the experiments. Second, the triple line movement during EW performance should be controlled to ensure a quasi-static condition. Details on the introduction of the quasi-static condition can be found in Chapter 5.3.1.

In the following sections, the pre-investigations for satisfying these requirements are presented and discussed.

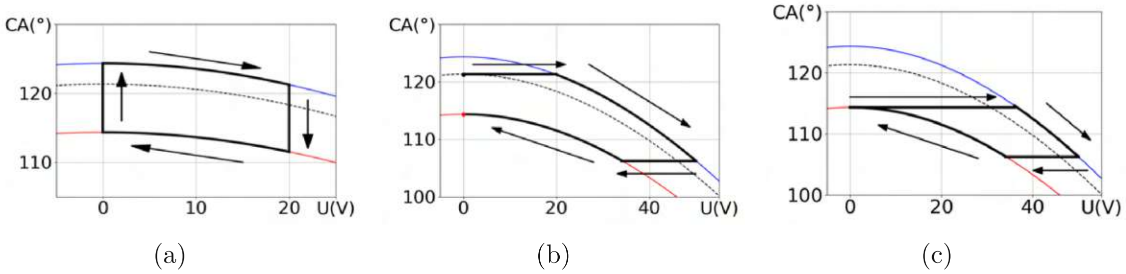

(a) (b) (c)

Fig. 7.3: CA hystereses. (a) vertical hysteresis during EWOD: a sequence of CA variations is shown within the limits of the advancing and receding CA. For a given applied voltage the CA can be manipulated e.g. by changing the droplet volume, as shown by the vertical lines in the graph. (b) Horizontal hysteresis: starting with a CA of θ_{Y}, increasing the voltage (horizontal line) does not result in a change of CA until the intersection with the advancing CA line (blue) is reached. Afterward, the EW-CA follows the advancing line $\theta(U)$ until the applied voltage level starts decreasing. The horizontal line in the hysteresis graph represents a constant CA until the receding line (red) is reached when the voltage decreases. Then the CA follows the receding line until $U = 0\,\mathrm{V}$, the maximum receding CA ($\theta_{\mathrm{rec}}^{\mathrm{max}}$) is reached and determined, which cannot be exceeded by any following voltage changes. (c) Horizontal hysteresis similar to the hysteresis as shown in (b). After applying a voltage cycle as shown in (b), the CA cannot reach a value greater than $\theta_{\mathrm{rec}}^{\mathrm{max}}$.

7.3.1 Electrical characterization

The voltage versus current (IV) measurement method is used to determine the dielectric properties, and to assess the dielectric layer's ability to withstand the applied high voltage up to 100 V.

The current I is the time derivative of charge Q and the applied voltage U and is written as

$$I = \dot{Q} = C \cdot \dot{U} \tag{7.5}$$

with a constant capacitance C. A typical measurement result is shown in Fig.7.4 and the measurement details are introduced in Chapter 4.3. A perfect linear relationship between the measured voltage and time at various constant currents between -100 and $100\,\mu\mathrm{A}$ was observed, indicating that the capacitance and dielectric constant of the Teflon AF layers remained. After calibration of the measurement setup, the result of the specific capacitance and the dielectric constant of the Teflon AF1600 layer is $c = C/A$ =16.03 µF/m^2, and $\epsilon_r = 1.92$, respectively.

In summary, the results of this pre-investigation indicate that the dielectric property is constant and stable, independent of the magnitude and polarity of the applied voltage within the range of -100 to $+100$ V.

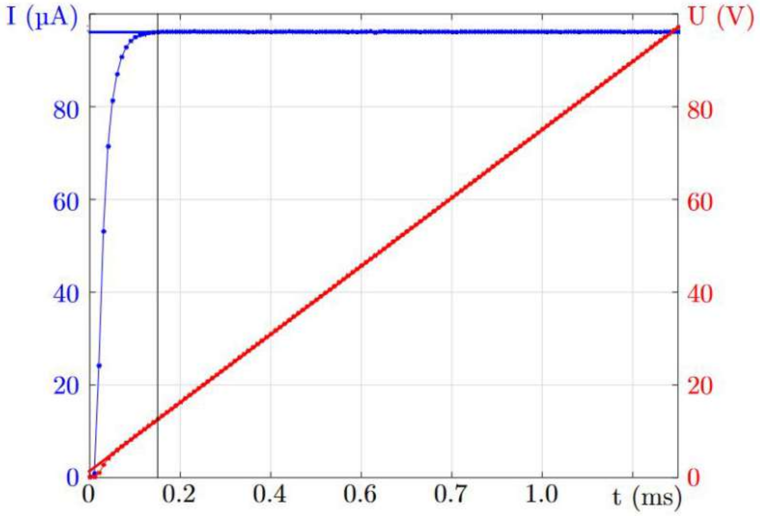

Fig. 7.4: A typical IV measurement result. After a settling time of ≈0,15 ms the constant I and the constant $\dot{U} = \mathrm{d}U/\mathrm{d}t$ show the linear dielectric material with constant $C = I/\dot{U}$ up to a voltage of 100 V. The thick solid lines denote the linear fit.

7.3.2 CA Saturation

CA saturation is a phenomenon observed during EWOD experiments where the CA reaches a maximum value and cannot be further manipulated by increasing the applied voltage[203–207]. However, the origin of CA saturation remains controversial. Some studies have suggested that the saturation is attributed to dielectric breakdown during the experiments[205, 206], while others have reported that it is due to reversible or irreversible charge trapping.[53, 208–211]. More details regarding CA saturation can be found in Chapter 2.

To ensure the long-term reliable properties of the dielectric layer, it is important to avoid CA saturation in EWOD experiments. Therefore, the saturation behavior of the CA and voltage on the EWOD samples was pre-investigated by applying a triangular voltage with a maximal amplitude of 100 V and a speed of 1 V/s. The results are shown in Fig. 7.5, where it can be observed that the saturation voltage is around 88 V, with a corresponding saturation CA of $70 - 72°$.

In conclusion, to prevent permanent and irreversible changes in the surface properties due to CA saturation, a maximal voltage level of 80 V was applied for EWOD experiments.

7.3.3 Quasi-static condition

To satisfy the quasi-static condition in EWOD experiments, the capillary number (Ca), which describes the relative effect of viscous forces on the surface tensions, should be small so that any dynamic effects can be neglected. In general, a capillary number of $\mathrm{Ca} < 10^{-5}$ is considered to satisfy the quasi-static condition. Details regarding Ca and quasi-static condition can be found in Chapter 5.3.1.

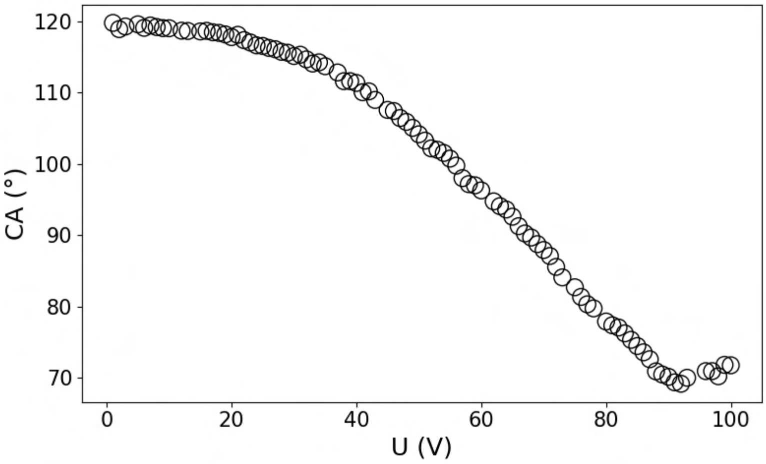

Fig. 7.5: CA as a function of voltage for the CA saturation investigation.

In the following, the process of connecting the velocity of the triple line to the speed/slope of the applied voltage is introduced, and as a result, the voltage slope for ensuring quasi-static conditions is obtained.

As described in Chapter 5.3.1, the droplet volume can be expressed as a function of the base radius and the CA, as shown in Equation 4.3. During EWOD performance, the CA measurement was conducted using the *Saturated-Humidity-Setup*, which ensured that the droplet volume remained constant. Therefore, the droplet volume equation given in Eq. 4.3 can be rearranged to express the droplet base radius r as a function of the CA θ. This gives:

$$r(\theta)^3 = \frac{3 \cdot V}{\pi} \cdot \frac{\sin^3\theta}{(1-\cos\theta)^2 \cdot (2+\cos\theta)}. \tag{7.6}$$

The change of the CA due to the applied voltage leads to a change in the base radius, manifested as a movement of the triple line:

$$\frac{\partial r}{\partial \theta} = \frac{-r(\theta)}{(2+\cos\theta)\cdot\sin\theta} \tag{7.7}$$

The variation of the CA due to the applied voltage U is described by the Young-Lippmann equation, $\cos\theta = \cos\theta_Y + \frac{c \cdot U^2}{2 \cdot \gamma_{\mathrm{la}}}$, as

$$\frac{\partial \theta}{\partial U} = \frac{-c \cdot U}{\gamma_{\mathrm{la}} \cdot \sin\theta}, \tag{7.8}$$

with the liquid-air interface tension γ_{la}, and the specific capacitance c of the dielectric layer. The CA and contact radius r as a function of the applied voltage are shown in Fig. 7.6(left). Finally, the velocity of triple line, $v = \partial r/\partial t$, due to the applied voltage is determined by:

$$v = \frac{\partial r}{\partial \theta} \cdot \frac{\partial \theta}{\partial U} \cdot \frac{\partial U}{\partial t} \tag{7.9}$$

In the EWOD experimental series, a triangular voltage is applied with a constant slope $k_u[V/s]$. Combined with Eq. 7.9, The velocity of the the triple line, v, is written as a function of the voltage slope k_u:

$$v = k_u \cdot \frac{\partial r}{\partial U}. \tag{7.10}$$

The derivative of base radius and applied voltage, $\partial r/\partial U$, was calculated using Equations 7.7 and 7.8. The results are shown in Fig. 7.6(right), and reveal that the maximal derivative of base diameter to the applied voltage, $\partial r/\partial U$, occurs at the maximal applied voltage of $U = 80$ V at a temperature of 25 °C.

As the critical velocity of the triple line that ensures a quasi-static condition is temperature dependent, details can be seen in Fig. 5.3 from Chapter 5.3.1, the critical voltage slope is temperature dependent as well. The critical voltage at the investigated temperature range is shown in Fig. 7.7.

In conclusion, it is necessary for the applied voltage slope to be smaller than the critical value to ensure a quasi-static condition of the triple line movement and accurate CA determination.

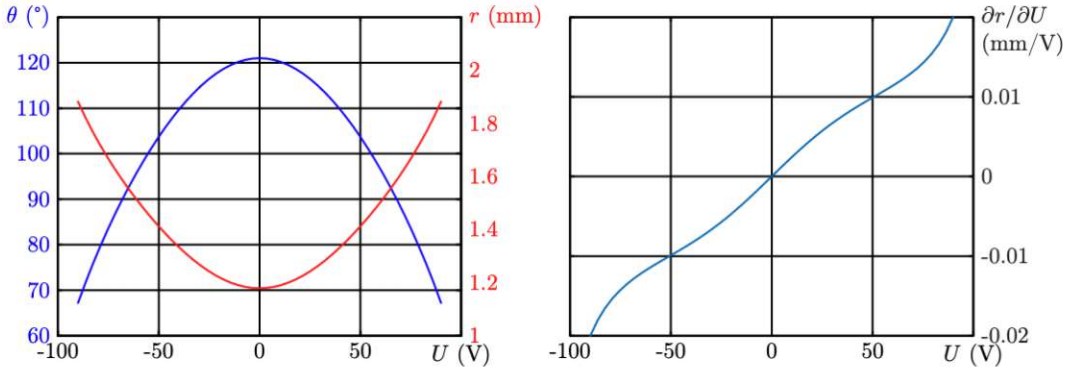

Fig. 7.6: Calculated voltage dependence of CA (θ) and base radius (r) (left) and $\partial r/\partial U$ (right) for a small water droplet ($V = 10\,\mu\mathrm{L}$, $\gamma_{\mathrm{la}} = 72\,\mathrm{mN/m}$ at $T = 25$ °C) placed on the Teflon AF 1600 layer ($c = 16.03\ \mu\mathrm{F/m}^2$).

To give a short summary of the pre-investigation section, the dielectric constant, the maximal applied voltage, and the critical voltage slope were pre-investigated to enable constant sample properties during EWOD experiments by preventing CA saturation and maintaining a quasi-static condition.

7.4 Results and Discussion

7.4.1 EW performance

The following section presents the experimental setup and results of the EWOD performance on the single dielectric layer, which are described in detail in Chapter 3.4.1.

The applied voltage is a symmetric triangle signal with a maximum level of 80 V to prevent irreversible surface changes due to CA saturation, and a limited voltage slope for

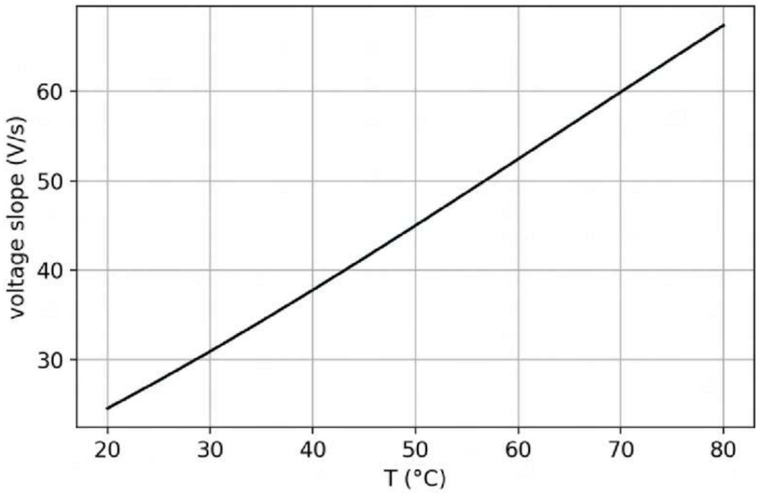

Fig. 7.7: Calculated voltage slope as a function of temperature.

quasi-static conditions (Chapter 7.3.3). The details of the EWOD setup are described in Chapter 4.4. To ensure a reliable response of the CA, the voltage signal is applied for 10 cycles. Figure 7.8 shows the applied voltage and a typical response of the CA.

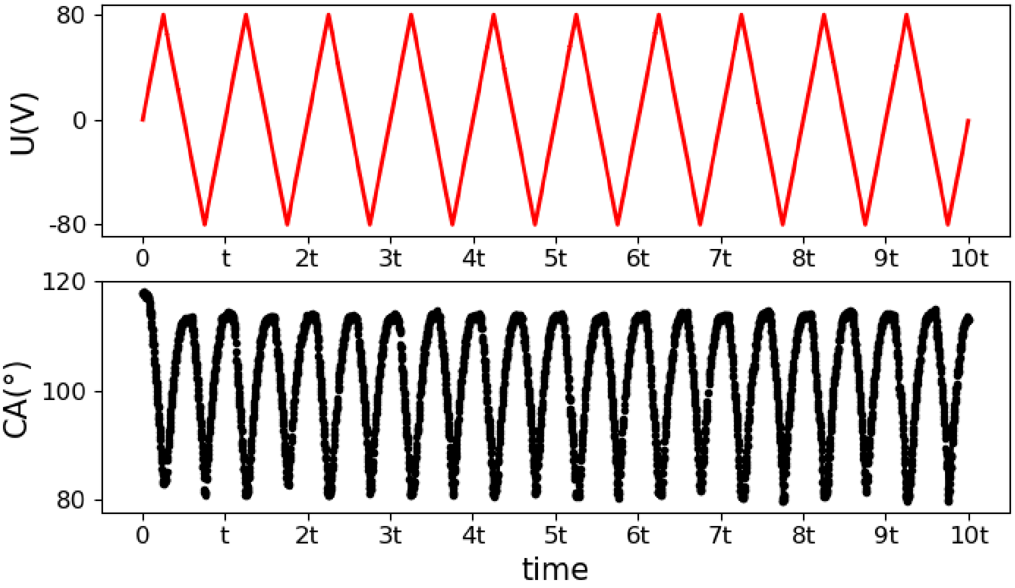

Fig. 7.8: Applied symmetric triangular voltage (in red) and the corresponding EW-CA (in black) over ten cycles at $T = 30\,°\mathrm{C}$. The time axis is scaled using the period length t = 32 s.

To investigate the effect of the voltage changing velocity (voltage slope) on the EWOD response, several experiments were performed at a temperature of $T = 30\,°\mathrm{C}$ with voltage slopes ranging from 1 V/s to 16 V/s, all of which are lower than the limit stated above. Fig. 7.9 shows the CA results of the first and second cycles as a function of voltage. The obtained CA results demonstrate that the applied voltage slopes used in the experiments have a negligible effect on the EWOD response within the quasi-static condition. Moreover, the experimental data exhibit excellent agreement with the FA model in the positive voltage range. The FA model and its details are presented in the previous section, Chapter 7.2. In the negative voltage range, the FA model perfectly predicts the CA up to $-40\,\text{V}$. However, as the applied voltage increases further, the CA becomes higher than predicted. At an applied voltage of -80 V, a higher CA of $1-3$ ° is presented. This phenomenon is observed in each cycle and can be explained by charge trapping on the dielectric surface[53, 209, 211]. Some representative droplet images are shown in Fig. 7.10. The charge trapping effect weakens the electrical field, thereby reducing the electrical energy stored in the dielectric layer, F_{el}, leading to a higher CA than expected at a given voltage (Eq. 7.2). Moreover, this trapping effect is reversible since the CA is consistent with the FA model again in the following positive half-voltage cycle after the negative voltage range where the trapping effect appeared.

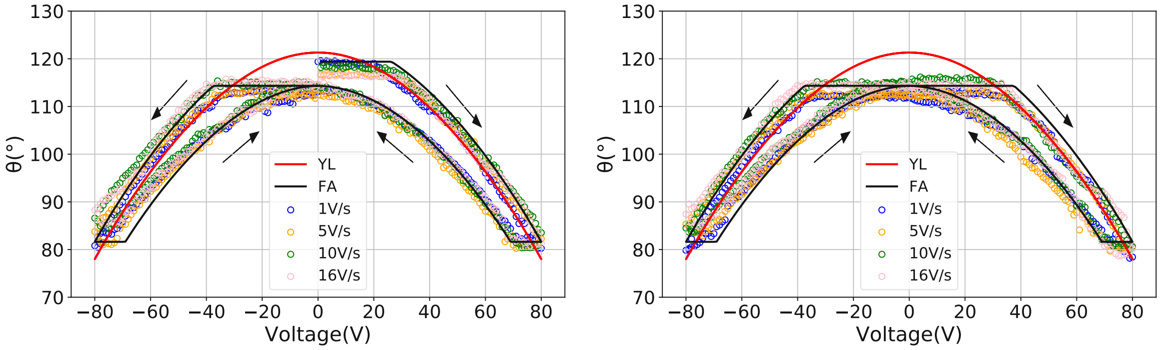

(a) 1^{st} cycle (b) 2^{nd} cycle

Fig. 7.9: Characteristic EW response at a temperature of 30 °C with different voltage slopes for the (a) first cycle, and (b) second cycle. The solid red line represents the EW-CA described by the classical YL equation. The solid black line is the EW-CA described by the FA model.

7.4.2 Temperature-dependency of EW

The previous part proves that the CA is independent of the applied voltage slope under quasi-static conditions, and shows high accordance between experimental results and the FA model, where the CA is determined additionally by a temperature-dependent adsorption contribution (F_{ad}) and a temperature-independent friction force (F_{f}), see Eqs. 7.3 and 7.4. The EW-CA is not only influenced by the voltage but also by the temperature due to the temperature-dependent adsorption contribution (F_{ad}), Young's contact angle (θ_{Y}), and the liquid surface tension (γ_{la}). In this chapter, the temperature dependency of EW-CA is presented and discussed.

EWOD experiments were performed using a voltage ramp speed of 10 V/s for ten cycles over a temperature range of 25 °C to 70 °C. A few characteristic EW-CAs for the chosen voltage level are extracted:

- the minimal advancing CA, $\theta_{\text{adv}}^{\text{min}}$, at positive voltage polarity, $U = 80\,\text{V}$;

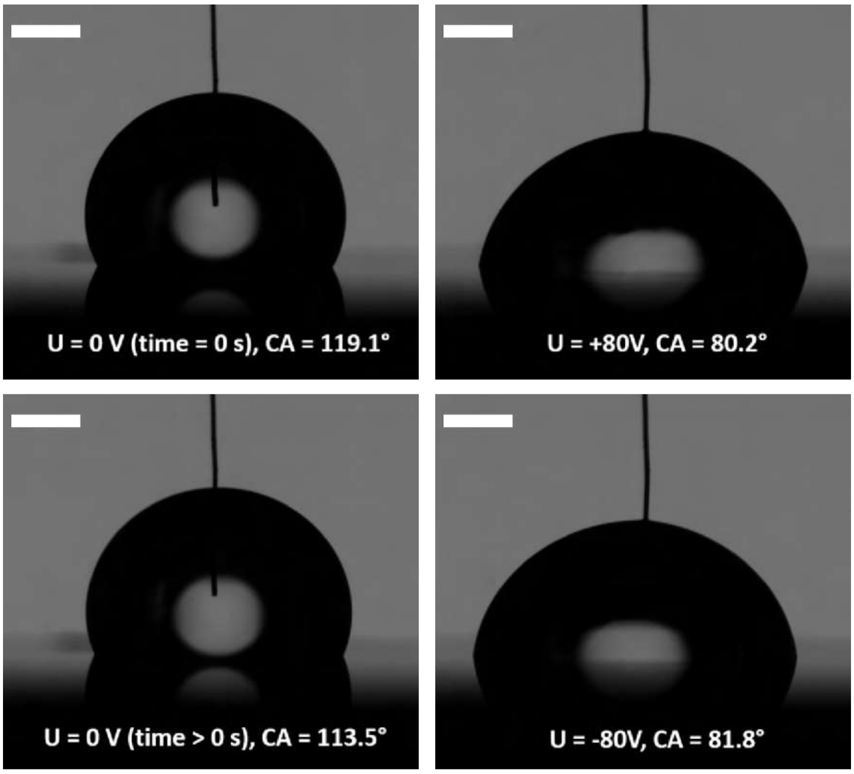

Fig. 7.10: Typical images of the droplet at different applied voltage. The length of the white bar represents 1 mm.

- the minimal advancing CA, $\theta_{\mathrm{adv}}^{\mathrm{min}}$, at negative voltage polarity, $U = -80\,\mathrm{V}$;
- the maximal receding CA, $\theta_{\mathrm{rec}}^{\mathrm{max}}$, at zero voltage, $U = 0$.

These characteristic CAs are shown in Fig. 7.2 in blue and red points for $\theta_{\mathrm{adv}}^{\mathrm{min}}$ and $\theta_{\mathrm{rec}}^{\mathrm{max}}$, respectively. Fig. 7.11 shows the average values of the characteristic CAs over ten cycles as a function of temperature, and compares the experimental data to the predictions of the Young-Laplace equation and the FA model. The results of $\theta_{\mathrm{rec}}^{\mathrm{max}}$, shown in Fig. 7.11(a), reveal that the maximal receding CA, $\theta_{\mathrm{rec}}^{\mathrm{max}}$, increases with temperature. At temperatures below 50 °C, the experimental results are consistent with the FA model. At higher temperatures, the EW-CAs are overestimated by the FA model, and more scattered[137]. The results of $\theta_{\mathrm{adv}}^{\mathrm{min}}$, shown in Fig. 7.11(b)(c), reveal that the minimal advancing CA, $\theta_{\mathrm{adv}}^{\mathrm{min}}$ decreases with temperature, and this trend is consistent with the CA predicted by the FA model. However, for the negative voltage polarity (Fig. 7.11(c)), the experimental CAs are higher by $1-3°$ compared to the positive voltage polarity and the expected values from the FA model. These higher CAs are also shown in Fig. 7.9 from the previous part. The reason could be a negative charge trapping onto the Teflon AF1600 layer [53, 209, 211]. This observed trapping effect is reversible since the CA at the positive voltage polarity over ten voltage cycles is well predicted by the FA model.

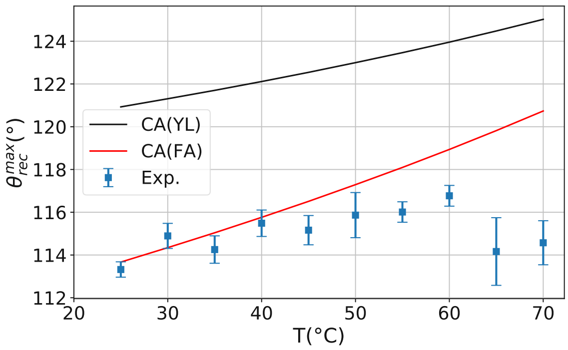

(a) $\theta_{\text{rec}}^{\text{max}}$, $U = 0\,\text{V}$

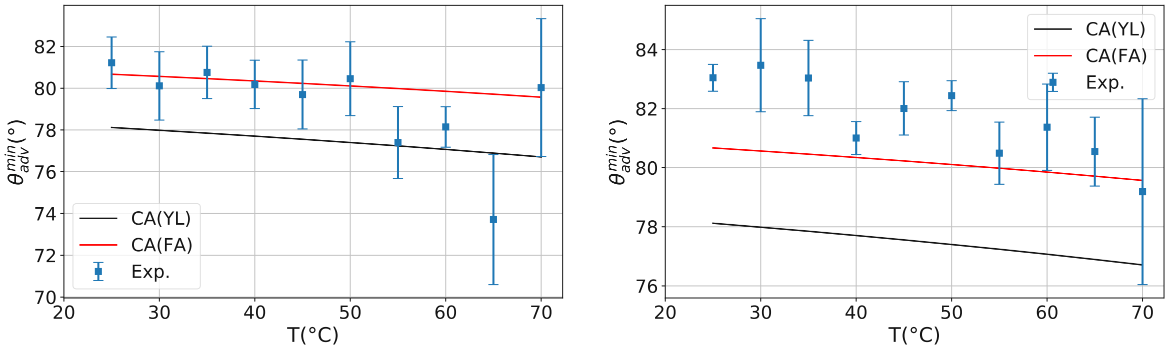

(b) $\theta_{\text{adv}}^{\text{min}}$, $U = 80\,\text{V}$.

(c) $\theta_{\text{adv}}^{\text{min}}$, $U = -80\,\text{V}$.

Fig. 7.11: The characteristic EW-CAs with voltage slope of $10\,\text{V/s}$ for ten cycles over temperature: (a) $\theta_{\text{rec}}^{\text{max}}$ for $U = 0\,\text{V}$, (b) $\theta_{\text{adv}}^{\text{min}}$ for positive polarity $U = 80\,\text{V}$, (c) $\theta_{\text{adv}}^{\text{min}}$ for negative polarity $U = -80\,\text{V}$.

7.4.3 Electrowetting on superhydrophobic surface

The previous sections presented the EW response on the pristine Teflon AF1600, which has a very smooth surface with a R_{RMS} of less than 1 nm. The results reveal high accordance with the proposed FA model. A further question to consider is whether the FA model is also valid for rough surfaces.

In Chapter 6, the surface modification of Teflon AF1600 through plasma treatment was presented and discussed. The results of the surface characterization revealed that after the oxygen plasma treatment, nanoscaled structures were formed on the surface while the changes in chemical compositions were negligible. Based on these findings, it is assumed that after the oxygen plasma treatment, the friction force limit, F_{fmax}, on the surface increases while the ability of the surface to adsorb water molecules, F_{ad}, remains unchanged. Therefore, the adsorption contribution, F_{ad}, which is acquired from pristine Teflon AF1600, was used to describe the adsorption contribution on the plasma-treated surfaces as well. The F_{fmax} on each plasma-treated surface was experimentally determined. Details can be found in Chapter 6.2.

Here, the EW experiments were conducted on these plasma-treated surfaces and the acquired results are shown in Fig. 7.12. The $\theta(U)$ at advancing and receding limits are shown by red and blue solid lines, while the black points represent the experimental EW-CAs. When applying an increasing voltage on plasma-treated surfaces, the measured EW-CA stays constant first and then follows the advancing CA line. This trend is visible in Fig. 7.12(a)(b), for the samples which exhibit pillar-like surface structures due to oxygen plasma treatment with energies of 5 and 6 kJ. On surfaces that are treated with higher plasma energies (> 6 kJ), the CA is subjected to additional stick-slip phenomena, as shown in Fig. 7.12(c)(d). The CA as well as the triple line stays unchanged when increasing the voltage after reaching the advancing line. This is the so-called stick phase. Then, the CA as well as the triple line jumps, which is the so-called slip phase. Although the FA model does not account for stick-slip phenomena, it successfully predicts the CA after each slipping. This can be observed in Fig. 7.12(c)(d), where the CAs jump to the advancing CA line following each stick phase. One probable interpretation for the stick-slip phenomena is that the fiber-like structures (see Fig. 6.3 in Chapter 6) with their undercuts act as pinning sites, leading to the alternated stick and slip phases[51].

When the applied voltage is decreased, the CA should remain constant until the receding CA line is reached, and then follow this line, according to the FA model. In the experimental results (Fig. 7.12), however, this behavior is not visible. The CA remains constant until zero voltage, with a θ_{rec} smaller than that predicted by the FA model. The reason might be that the nanoscaled structures have a strong trapping effect on ions, and therefore result in an unchanged CA when reducing the voltage.

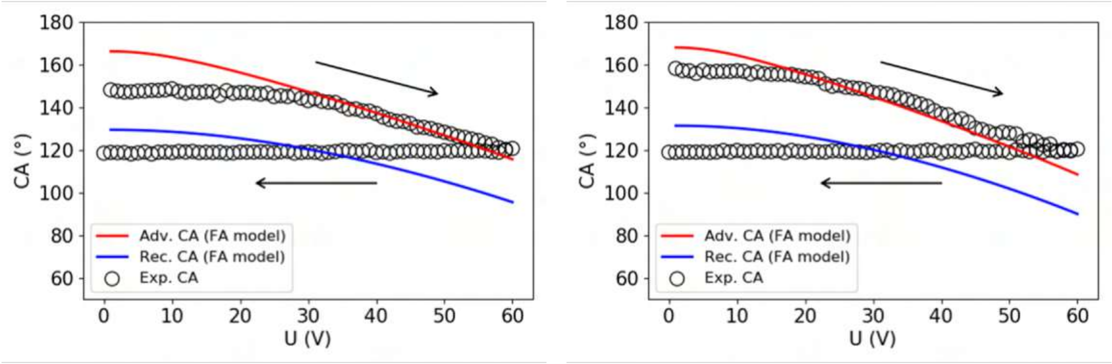

(a) 5 kJ (b) 6 kJ

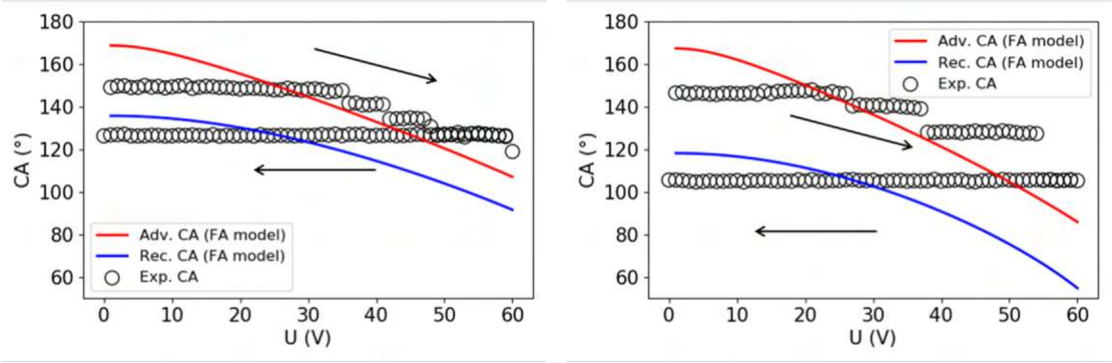

(c) 7 kJ (d) 8 kJ

Fig. 7.12: EW response on oxygen-plasma treated surface with the energy of 5, 6, 7, and 8 kJ. The arrows indicate that the applied voltage is increased from 0 to 60 V and then decreased back to 0 V with a voltage change of 1 V/s.

7.5 Summary

In this Chapter, the results of both pre-investigations and EW performances on pristine as well as plasma-treated Teflon AF1600 are presented and discussed. The results reveal that

- within the quasi-static condition, the results of EW-CA are independent of the applied voltage slope (i.e. velocity of triple line movement).
- The EW-CA at a temperature up to 50 °C is in good agreement with the proposed FA model.
- However, the reversible trapping effect happens on the surface when a negative voltage is applied, and weakens the electrical energy, leading to a higher CA than predicted by the FA model.
- The FA model is applied to describe the EW behavior on oxygen plasma-treated Teflon AF1600 surfaces as well. The EW-CAs at advancing limits are well predicted by the FA model up to the energy of 6 kJ. For surfaces treated with higher energies,

the nanoscaled fiber-like structures feature a few undercuts that serve as pinning sites, consequently leading to the stick-slip regime of the CA in the advancing limit. The EW-CAs do not follow the receding limit, a probable reason is that the surface structures have a strong trapping effect, which is not reversible.

Chapter 8

Hydrophobic recovery of PDMS

Contents

Some sections of this chapter were previously published in the paper titled "Surface properties of µm and sub-µm polydimethylsiloxane thin films after oxygen plasma treatment"[140].

8.1 Introduction

As introduced in Chapter 2.3.2, PDMS has enabled various application fields such as surface engineering[126–129], optical gratings[130, 131], microfluidics[132–134], stretchable electronics[135], biochips[128, 133, 136] and so on, due to its outstanding thermal and chemical stability, optical transparency, biocompatibility, and extreme cost-efficiency. In addition, PDMS is hydrophobic and is seen as an excellent alternative to Teflon AF1600 for various applications requiring a hydrophobic surface. However, PDMS is also an easily tailored and self-aging material. That is, the surface wetting properties are easily modified when it is exposed to a UV light environment or oxygen plasma due to the creation of silanol (Si-OH) terminal groups and formation of a silica layer onto the surface[119–123, 125, 133, 212]. Moreover, the surface-wetting properties undergo continuous changes attributed to both the migration of low molecule weight (LMW) species from the bulk material to the surface and the reorientation of hydrophilic terminal groups into the bulk material[133]. This self-aging process is known as hydrophobicity recovery[133].

The ability to modify the surface wetting properties of PDMS can be highly beneficial in various applications. For instance, in microfluidics where a hydrophilic surface is crucial for capillary-driven fluid flow, exposure to oxygen plasma can achieve surface hydrophilization of PDMS.[132–134]. Moreover, Pascual et al. proposed a method to locally tune the wettability of a PDMS surface. This method involves local heating of a plasma-hydrophilized PDMS surface to accelerate the hydrophobicity recovery process while the rest surface remains hydrophilic[213]. However, in certain applications that require a long-term and consistently hydrophilic or hydrophobic surface, the self-aging of surface wetting properties can pose a severe challenge.

In addition to the surface wetting properties, the surface topography of the soft PDMS can be also efficiently modified. This is achieved by forming buckling structures on the surface, which results from the mismatch in mechanical properties between the silica layer and the soft PDMS[119, 121, 125]. Such a property has made PDMS a significant material in surface engineering[126–129] and optical grating applications[130, 131].

Therefore, a comprehensive understanding of the surface properties of PDMS is crucial to ensure its proper utilization in various applications. There are numerous studies on the surface properties of PDMS in the literature[119–125], and the continued interest in PDMS is evidenced by several recent review papers[128, 133, 134, 214, 215]. These studies indicate that the surface properties of pristine and plasma-treated PDMS are subject to variability due to the influence of fabrication parameters (e.g. prepolymer-to-crosslinker ratio, treatment time) as well as the layer thickness[119–123, 216, 217]. Liu et al. investigated the mechanical properties of PDMS with a thickness ranging from 30 to 350 µm. Their findings indicated that as the thickness of PDMS increased, the Young's modulus decreased[120]. Hyun and Jeong deposited a thin polymer layer on an oxygen plasma-treated PDMS surface and induced buckling structures on the surface. The resulting waviness of the buckling structures (2.76, 3.31 and 3.52 µm) increases when the thickness of PDMS increases (0.5, 2 and 20 mm)[119]. Studies by Nguyen et al. and Bhandaru et al. explored the impact of PDMS thickness on the hydrophobicity recovery process after hydrophilization of the surface. Their investigations were carried out on PDMS films with thicknesses ranging from a few micrometers to 1 mm and $3.9 - 30$ mm, respectively. The results revealed that the recovery process was faster on thicker PDMS films[122, 123]. The study by Firpo et al. demonstrated that the permeability of PDMS membranes to CO_2 and He is thickness-dependent when the membrane thickness is below tens of micrometers[218].

In summary, the studies discussed above emphasize the importance of PDMS film thickness in determining its mechanical properties, buckling structures, hydrophobicity recovery, and ultimately its suitability for various applications. With the increasing use of PDMS in devices requesting lower film thicknesses, it is essential to understand how its surface properties in the micrometer and submicrometer thickness range are influenced by process parameters.

For this purpose, a comprehensive understanding of the surface properties of both pristine and plasma-modified PDMS thin films in the thickness micrometer and submicrometer range of was provided. Thin PDMS films were fabricated by varying the dilution ratio, and the PDMS surface was exposed to oxygen plasma treatment with various treatment times. A wide range of surface properties, including effective Young's moduli, surface topographies, and wetting properties, as well as the hydrophobicity recovery process, were investigated over a time period of more than one month.

8.2 Experimental details

Details on the fabrication process of the PDMS thin films can be found in Chapter 3.2.2. The films were fabricated using spin-coating and controlled to have thicknesses of 0.86 µm and 3.5 µm by adjusting the spin-coating parameters and using different dilution ratios (dilution liquid vs PDMS). To provide better clarity in the following part, the samples are labeled with M and m for indicating the micrometer range (3.5 µm), N and n for indicating the nanometer range (0.86 µm). A lowercase letter (e.g. m and n) indicates a relatively higher dilution ratio than the uppercase letter (e.g. M and N). The dilution ratios for each sample can be seen in Table. 8.1.

After fabrication, the samples were subjected to oxygen plasma treatment for 5, 15, and 30 s. Further details on the plasma treatment can be found in Chapter 3.3.1. The samples were then characterized for their effective surface near Young's moduli, surface topographies, and wetting properties using a force-indentation curve, AFM imaging, and CA measurement, respectively. More information on these characterization methods can be found in Chapters 4.5.2 and 4.2.2.2. The results of these investigations are presented and discussed in the following sections.

8.3 Results and discussion

8.3.1 Young's modulus

Table 8.1 shows the obtained results of the effective surface near Young's modulus for each sample. For the cross-linked PDMS film with a dilution ratio of 0:1 (M sample, non-diluted), the effective Young's modulus value was found to be 3.1 ± 0.12 MPa, which is comparable to values reported in literature [119, 133, 219, 220].

The effective Young's modulus of samples m and N are found to be identical despite having different film thicknesses but the same dilution ratio of 5:1. This observation indicates that the dilution ratio plays a more dominant role than the thickness in affecting the effective Young's modulus of the film within the investigated range. Specifically, a higher dilution ratio results in a lower effective Young's modulus.

Several studies in the literature have investigated Young's modulus of cross-linked PDMS films and membranes[119–121, 221]. Liu et al. fabricated membranes with a thickness ranging from 35 to 350 µm using non-diluted PDMS and reported a thickness-dependency of the Young's modulus[120]. Their results revealed that an increase in thickness leads to a decrease in Young's modulus of the cross-linked PDMS. In contrast to their results, the investigation in this study reveals that the effective surface near Young's modulus is independent of film thickness within the investigated range of 0.86 µm to 3.5 µm. In addition, it is important to note that the experimental setup in this study is different from the one used in Liu et al.'s study[120]. They performed tensile tests using a microforce tester to measure Young's modulus, which characterizes the bulk material's properties. In contrast, the force-distance curves were obtained by AFM, which reveals the effective surface near Young's modulus. Hyun and Jeong and Kim et al. investigated the impact of the prepolymer-to-crosslinker ratio on the Young's modulus of bulk PDMS[119, 121]. Their findings indicate that a lower prepolymer-to-crosslinker ratio (i.e., a higher

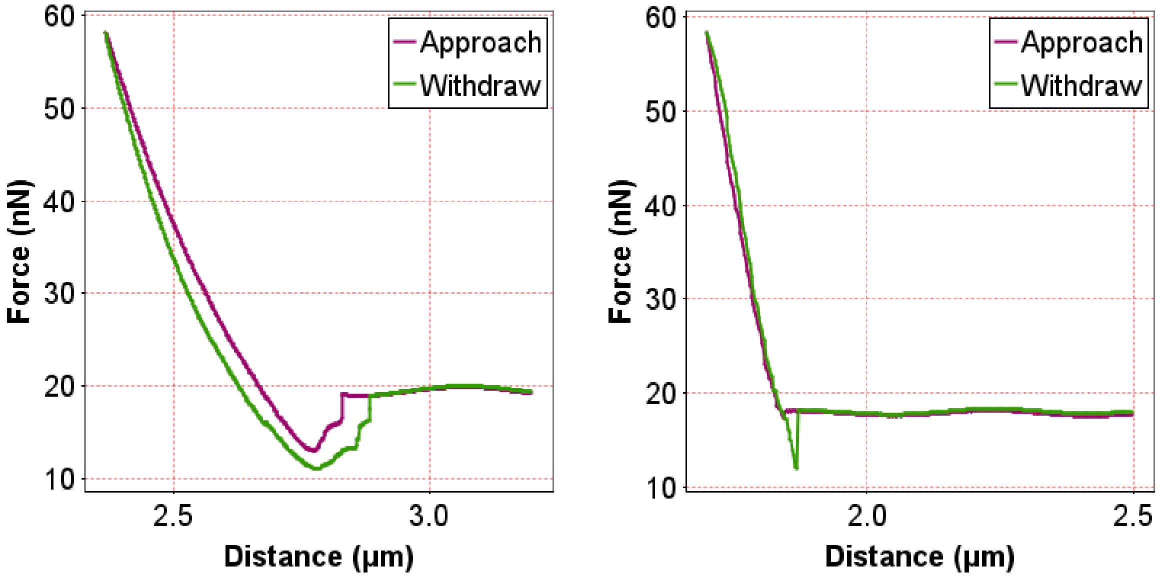

(a) (b)

Fig. 8.1: The force-distance curve acquired by AFM for (a) untreated pristine sample *n*, and (b) *m* sample treated by oxygen plasma for 15 s, *m15*.

percentage of crosslinker) results in a higher density of crosslinked PDMS, leading to an increased Young's modulus. In contrast, the prepolymer-to-crosslinker ratio was kept constant at 10:1 in this work, while the dilution ratio was varied to obtain thin films of different thicknesses. The results from this study demonstrate the importance of the dilution ratio in controlling the effective surface near Young's modulus, which provides new insights into the fabrication of thin PDMS films. Recent work from Inoue et al.(2022), who diluted the PDMS with hexane to create PDMS rubber and conducted tensile tests, showed a similar dependence of bulk Young's modulus on the dilution ratio.

An increase in the effective surface near Young's modulus was observed, reaching $8-10$ MPa after the formation of the stiff silica layer on the surface via oxygen plasma treatment, as shown in Fig. 8.2. A slight enhancement in the value of the effective surface near Young's modulus was also observed with increasing plasma treatment time. No clear correlation between sample type, i.e., PDMS film thickness and dilution ratio, and effective Young's modulus can be revealed.

Over the course of one month, a decrease below 1 MPa was observed in the effective surface near Young's modulus on all types of samples after conducting oxygen plasma treatment for different durations. It should be noted that the thickness of the silica layer produced by plasma treatment is typically only a few nanometers[222], and the effective Young's modulus measured by force-distance curve refers to the bilayer consisting of both the silica and PDMS layers.

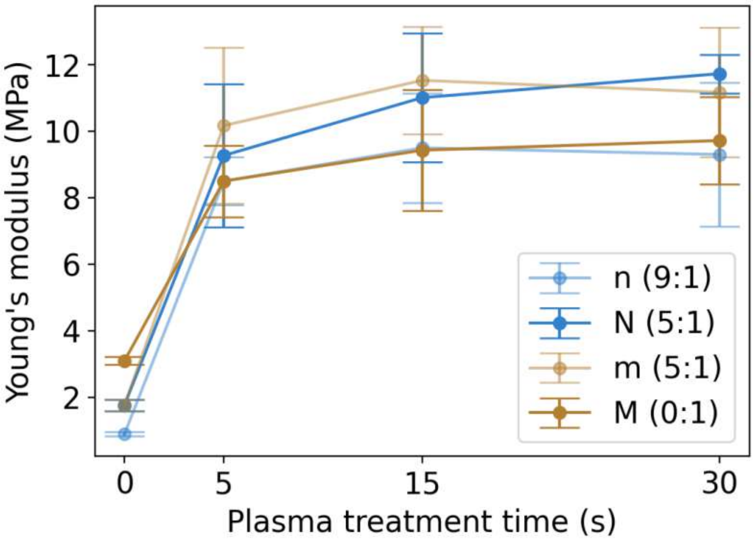

Fig. 8.2: The effective surface near Young's modulus of PDMS as a function of plasma treatment time. The inserted lines serve as guides for the eyes.

sample	E [MPa]	W [nm]		A [nm]	
		15 s	30 s	15 s	30 s
M (0:1)	3.1 ± 0.12	222 ± 0.1	231 ± 9.2	6.3 ± 0.63	19.8 ± 1.87
m (5:1)	1.8 ± 0.19	321 ± 14.1	342 ± 2.1	17.5 ± 1.22	27.0 ± 3.14
N (5:1)	1.8 ± 0.14	299 ± 7.8	318 ± 12.0	14.4 ± 1.79	23.6 ± 2.45
n (9:1)	0.9 ± 0.06	380 ± 41.7	367 ± 13.44	16.1 ± 1.74	31.7 ± 3.12

Tab. 8.1: Young's modulus, and the waviness (W) and amplitude (A) of buckling structure by 15 and 30 s plasma treatment of each sample.

8.3.2 Surface topography

In this section, the results of surface topography analyses with respect to the plasma treatment time, as well as the influence of sample type (thickness, dilution ratio, and effective Young's modulus) on surface topography are discussed. Additionally, the evolution of surface topography over time is analyzed.

Surface topography vs. plasma treatment time. Firstly, the changes in surface topography as a function of plasma treatment time are discussed. Examples of AFM images of untreated and plasma-treated N samples are shown in Fig. 8.3. With a treatment time of 5 s, the surface topography remained unchanged compared to the pristine PDMS surface, as observed from the AFM images. However, there was a significant drop in CAs, which will be further discussed in the section on wetting property analysis. A significant topographical modification is observed after 15 s plasma treatment, as buckling structures are formed on the surface, as shown in Fig.8.3(c). This surface modification is due to the mismatch of the thermal expansion coefficients between the stiff silica surface ($1 \times 10^{-6}\mathrm{K}^{-1}$ to $1 \times 10^{-7}\mathrm{K}^{-1}$) and the bulk elastomeric PDMS ($\approx 3.1 \times 10^{-4}\mathrm{K}^{-1}$)[124, 223–225]. The plasma treatment considerably increases the sample temperature, while the stiff silica layer is generated, leading to the formation of the observed buckling structures. Compressive stress is created in the top silica layer when the temperature decreases again during the purging process. The buckling structures are therefore formed to relieve the compressive stress[124, 223–225], as we can see from the AFM images illustrated in Fig. 8.3(c)(d).

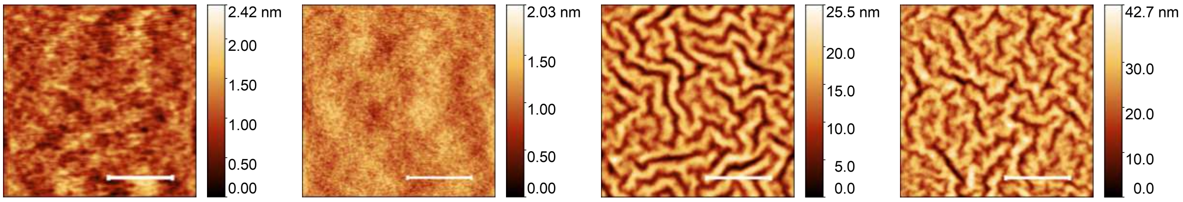

(a) N (1:5) (b) N5 (1:5) (c) N15 (1:5) (d) N30 (1:5)

Fig. 8.3: Topography of N sample with respect to the plasma treatment time. (a) non-treated surface (0 s). Sample treated by oxygen plasma for (b) 5 s, (c) 15 s, and (d) 30 s, respectively. The number inside the parentheses (1:5) represents the dilution ratio. The length of the white bar represents 1 µm.

Typically, the buckling structure is characterized by its waviness W and amplitude A, which are described by[212, 226, 227]

$$W = 2\pi h_s \left(\frac{\overline{E}_s}{3\overline{E}_P} \right)^{1/3}, \tag{8.1}$$

and

$$A = h_s \left(\frac{\varepsilon}{\varepsilon_c} - 1 \right)^{1/2}, \tag{8.2}$$

respectively. h_s is the thickness of the stiff silica layer. $\overline{E}_s$ and $\overline{E}_P$ are the in-plane strain moduli of the silica layer and the PDMS, respectively, and are described by Young's modulus E and Poisson's ratio ν, as

$$\overline{E} = E/(1-\nu^2) \tag{8.3}$$

where ε represents the compressive strain on the bilayer. The parameter ε_c is described by

$$\varepsilon_c = -\frac{1}{4} \left(\frac{3\overline{E}_P}{\overline{E}_s} \right)^{2/3}, \tag{8.4}$$

and defined as the critical buckling strain, or in other words, the minimum strain needed to induce buckling[227]. These equations indicate that the waviness and amplitude are proportional to the thickness of the silica layer, and the latter additionally depends on the strain.

The results of waviness and amplitude are shown in Table. 8.1 and demonstrate that when the plasma treatment time increases from 15 to 30 s, the waviness increases from 222, 321, and 299 nm to 231, 342, and 318 nm for samples M, m, and N, respectively. The amplitude increases from 6.3, 17.5, and 14.4 nm to 19.8, 26.9, and 23.6 nm, respectively.

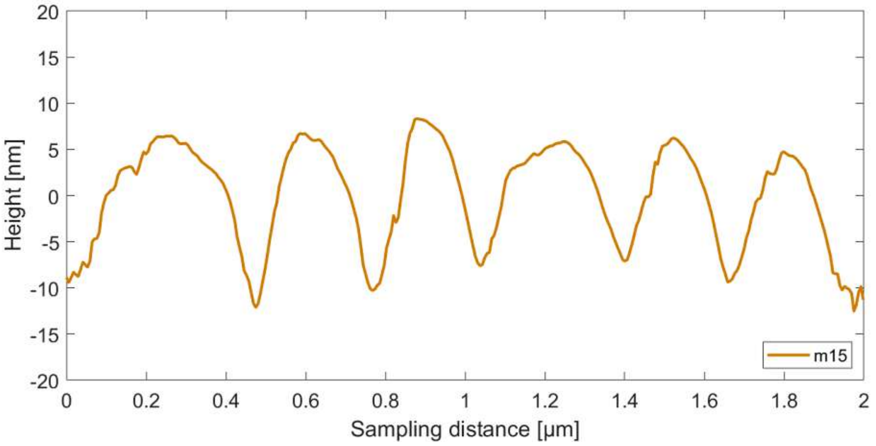

(a)

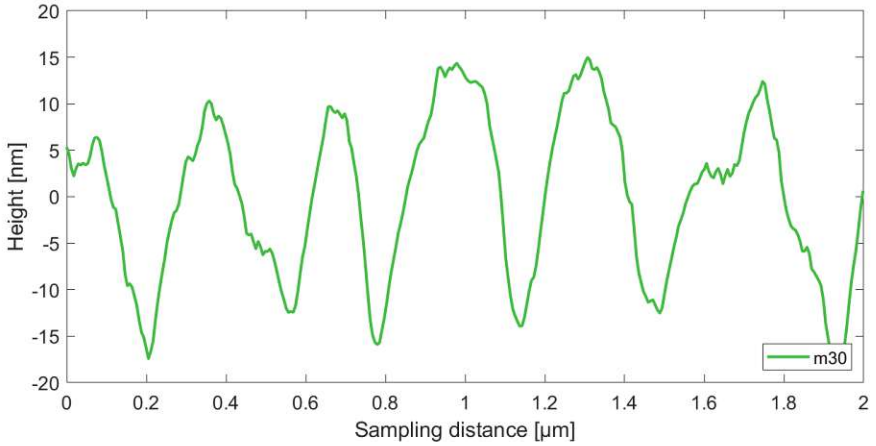

(b)

Fig. 8.4: Typical surface profiles for sample m treated by oxygen plasma for 15 s (a) and 30 s (b).

This increasing trend of waviness (W) and amplitude (A) with increasing plasma treatment time is consistent with Eqs. 8.1 and 8.2. When the plasma treatment time increases, the thickness of the silica layer (h_s) and the thermally-induced strain (ε) raises[151–153]. The raise in the former (h_s) results in an increase in waviness, while the raise of both quantities h_s and ε leads to an increase in amplitude. Accordingly, the amplitude shows a more pronounced increase (> 50 %) compared to waviness (< 7 %). The surface profiles of the m sample treated for 15 and 30 s are shown in Fig.8.4, revealing the significant increase in amplitude with plasma treatment time. Typical surface profiles of the m sample treated for 15 and 30 s are shown in Fig. 8.4 and reveal the slight increase of waviness and the significant increase in amplitude with increased plasma treatment time. However, the waviness of sample n changes from 380 ± 41.7 to 367 ± 13.44 when the plasma treatment time increases from 15 to 30 s. No significant increasing trend of waviness by increasing the treatment time can be revealed, as the error bars overlap. This may indicate the onset of treatment saturation.

Surface topography vs. sample type. The surface topography after oxygen plasma treatment is discussed regarding the sample type, more specifically, thickness, dilution ratio, and effective surface near Young's modulus. It is assumed that the thickness of the silica layer is independent of the sample type, as it is determined by the plasma treatment time and energy input[151–153]. According to Eq. 8.1, a decreased value of Young's modulus of PDMS leads to a raised value in waviness ($W \propto (1/\overline{E}_P)^{1/3}$). The results of waviness W are consistent with this statement, see the values of W in Table. 8.1. Furthermore, the comparison of the samples m and N, which have the same dilution ratio (5:1) and Young's modulus of PDMS (1.8 MPa), but different thicknesses, shows that the waviness of the buckling structure on sample m (3.5 µm), is larger than on sample N (0.86 µm). It is evident that the thickness of the PDMS also plays a role in waviness. This correlation between the PDMS thickness and the waviness is not included in Eq. 8.1 and has been also observed by the work of Hyun and Jeong in a PDMS thickness range of $0.5 - 20$ mm.

The resulting amplitude A exhibits a consistent trend described by the theoretical predictions. According to Eqs. 8.4 and 8.2, the critical strain, ε_c is proportional to $\overline{E}_P{}^{2/3}$, and the amplitude A is proportional $(\varepsilon/\varepsilon_c - 1)^{1/2}$, respectively. Therefore, a higher effective surface near Young's modulus leads to a higher critical strain, consequently resulting in a lower value of the amplitude of the buckling structure. Additionally, the results reveal that the amplitude of the formed buckling structure is also affected by the thickness of the PDMS layer. The thicker the PDMS film, the larger the amplitude of the formed buckling structure. This correlation between the amplitude and the film thickness is not accounted for in Eq. 8.2.

Surface topography vs. time. Last, the surface topography was investigated on each sample over a period of 30 days after plasma treatment. The waviness and amplitude of the buckling structure as a function of time are shown in Figs. 8.6 and 8.7, respectively. The blue graphs represent results for the sub-micrometer samples N and n, while the brown graphs show results for the micrometer samples, M and m. The lighter color represents samples with a higher dilution ratio. The lighter color indicates a higher dilution ratio. The results suggest that the waviness (W) remains relatively constant over time, while the amplitude (A) decreases, which may indicate surface relaxation.

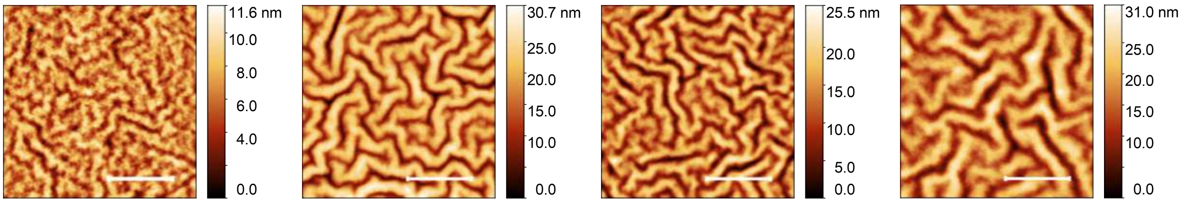

(a) *M15 (1:0)* (b) *m15 (1:5)* (c) *N15 (1:5)* (d) *n15 (1:9)*

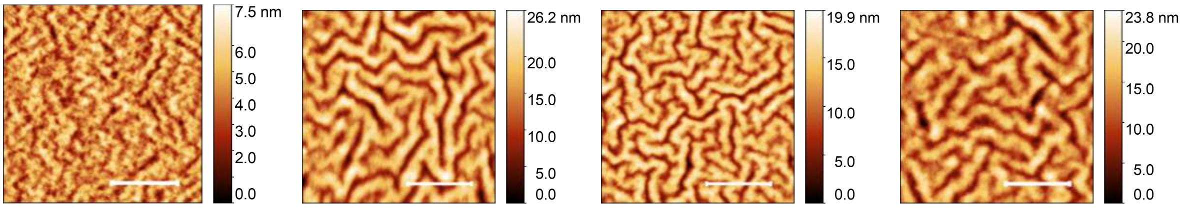

(e) *M15 (1:0)* at day 15 (f) *m15 (1:5)* at day 15 (g) *N15 (1:5)* at day 15 (h) *n15 (1:9)* at day 15

Fig. 8.5: The top row of AFM images shows typical images of samples *M*, *m*, *N*, and *n* treated with 15 s oxygen plasma obtained on day 1 after oxygen plasma treatment. The bottom row shows the corresponding AFM images obtained 15 days after plasma treatment. The length of the white bar represents 1 µm. The horizontal topography images demonstrate how the buckling structure changes across the different sample types. On the other hand, the vertical topography images reveal how the buckling structure evolves over time.

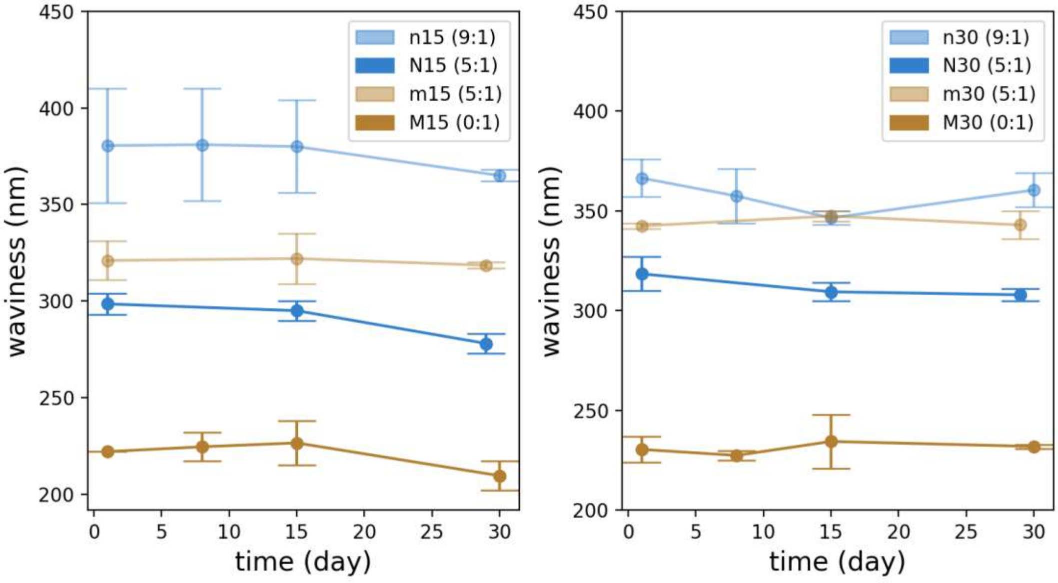

Fig. 8.6: The waviness of buckling structure over time after plasma treatment. Day 0 represents the day of plasma treatment conducting. For a better view, the points in the same color represent the results on samples with identical thicknesses (blue for M and m, brown for N and n). The number after the sample name refers to the plasma treatment time. The ratio in brackets is the dilution ratio and is represented by the transparency of the points. The results of the sample fabricated by a more diluted solution are shown in a higher transparency. The lines serve as guides for the eyes.

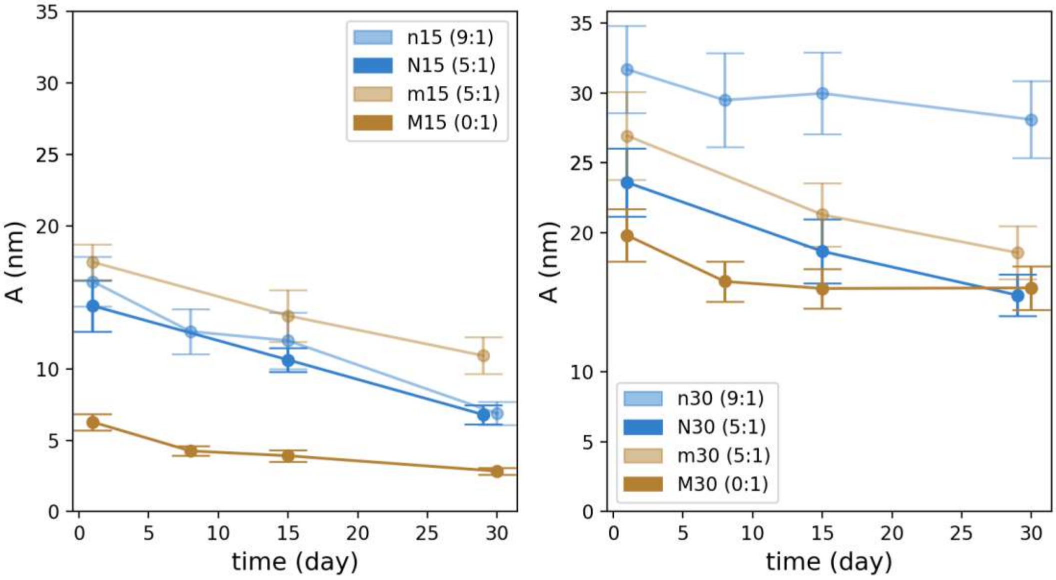

Fig. 8.7: The amplitude of buckling structure over time after plasma treatment. The lines serve as guides for the eyes.

8.3.3 Wetting property

The CA results are shown in Fig. 8.8. The advancing and receding CA on pristine PDMS, $\theta_{\mathrm{p}}^{\mathrm{adv}} = 117.4 \pm 1.02$ ° and $\theta_{\mathrm{p}}^{\mathrm{rec}} = 98.4 \pm 0.61$ °, reveal its natural hydrophobicity. This hydrophobicity is independent of sample types. The oxygen plasma treatment causes a drastic reduction in the hydrophobicity of the PDMS surface, leading to a highly hydrophilic surface. The initial CAs of the plasma-treated surface, which were obtained for the surfaces on the first day after oxygen plasma treatment, were $\theta_{\mathrm{i}}^{\mathrm{adv}} = 17 - 27$ ° and $\theta_{\mathrm{i}}^{\mathrm{rec}} = 0°$ for the advancing and receding CA, respectively, as shown in Fig. 8.8. These initial CAs are independent of the plasma treatment duration, surface topography, dilution ratio, and film thickness. The reduction of CA from $\theta_{\mathrm{p}}^{\mathrm{adv}}$ and $\theta_{\mathrm{p}}^{\mathrm{rec}}$ to $\theta_{\mathrm{i}}^{\mathrm{adv}}$ and $\theta_{\mathrm{i}}^{\mathrm{rec}}$ is due to the creation of hydrophilic silanol (Si-OH) terminal groups on the surface [122, 123, 133].

The CAs on plasma-treated surfaces were monitored over time, and they exhibited an increasing trend. This increasing trend is attributed to the reorientation of the hydrophilic functional groups to the bulk PDMS and the migration of hydrophobic LMW species from bulk to the surface[122, 123, 133]. Fig. 8.8 depicts the recovery process as the CAs on plasma-treated surfaces increase with time.

The CA is determined by the force equilibrium at the triple line by Young's equation[2], the effective solid surface tension, γ, is therefore written as

$$\gamma = \gamma_{\mathrm{sa}} - \gamma_{\mathrm{sl}} = \gamma_{\mathrm{la}} \cos(\theta), \tag{8.5}$$

where the γ_{sa}, γ_{sl} and γ_{la} represent solid-air, solid-liquid and liquid-air interface tension. θ can be advancing or receding CA. Using the measured CAs and the γ_{la} at 20 °C,

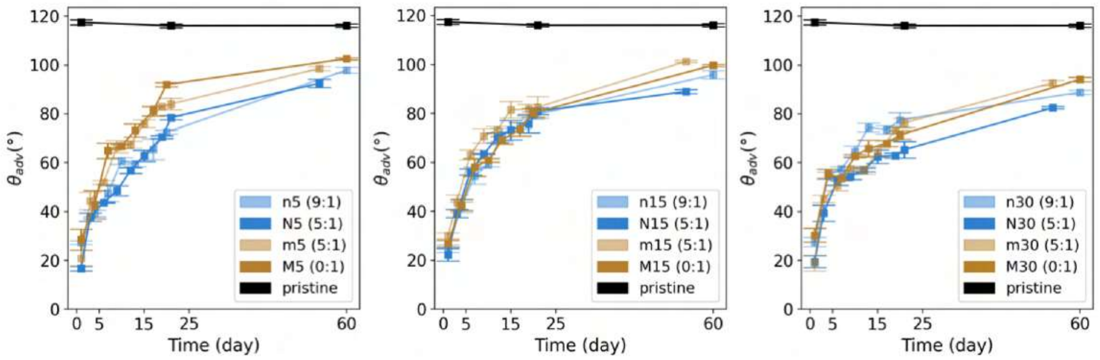

(a) advancing limit

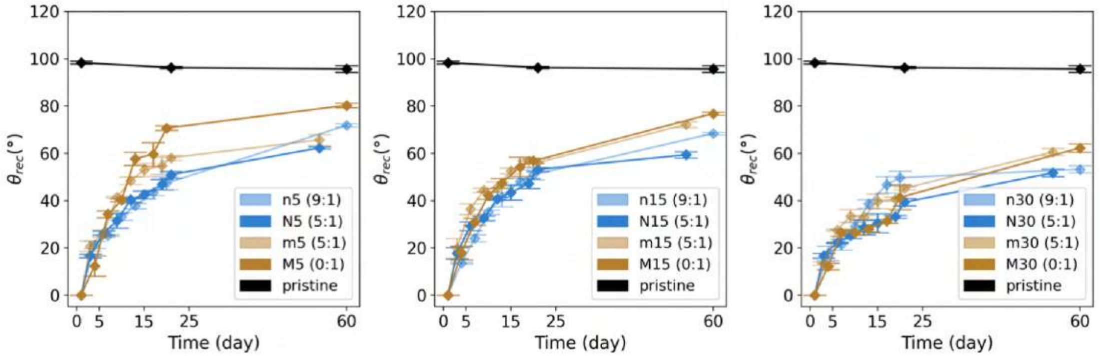

(b) receding limit

Fig. 8.8: Time dependent advancing (a) and receding CA (b). The CAs on pristine (untreated samples), θ_p, are shown in black. The hydrophobicity recovery process is shown by the CA increase on the plasma-treated surfaces over time. From left to right: PDMS treated by oxygen plasma for 5, 15, and 30 s. The lines serve as guides for the eyes.

72,8 mN/m[192], the effective solid surface tensions, γ are calculated for the advancing and receding limit.

To characterize the recovery process, it was approximated by an exponential function, starting with the effective solid surface tension of the initial plasma-treated surface, γ_i, and assuming that the final state of the recovery process is the pristine PDMS, γ_p. The recovery process of hydrophobicity described by γ is therefore written as

$$\gamma = (\gamma_\mathrm{i} - \gamma_\mathrm{p}) \cdot \exp(-\frac{t}{\tau}) + \gamma_\mathrm{p}, \tag{8.6}$$

where τ is the time constant and characterizes the initial and maximum speed of the recovery process. γ_i and γ_p are calculated through Eq. 8.5 with the corresponding θ_i and θ_p, respectively.

The recovery process within the first month is fitted according to Eq. 8.6. The slope of the fitting line, $-1/\tau$, is shown in Fig. 8.9 and characterizes the recovery speed. The higher the $1/\tau$, the faster the surface hydrophobicity recovers. Overall, the recovery speed reveals a smaller value when the plasma treatment time increases, and shows a significantly smaller value in the receding than in the advancing limit. For PDMS treated by oxygen plasma for 5 seconds, the recovery speed ($1/\tau$) for the micrometer samples M and m is considerably larger than that for the sub-micrometer samples N and n. Additionally, the dilution ratio also plays a role in the recovery process. A lower dilution ratio leads to a higher recovery speed. This higher recovery speed is assumed to be caused by the greater reservoir of LMW species in the thicker[122, 123, 133] and the less-diluted PDMS films. However, for samples treated with oxygen plasma for 15 and 30 s, there is no clear correlation between recovery speed and film thickness or dilution ratio. It is worthwhile to mention that the influence of the buckling structures on the CAs was neglected, since the effective increase of the surface area by the buckling structures is less than 4.4%. The CAs were measured again two months after the plasma treatment as shown in Fig. 8.8. The CAs on all plasma-treated samples did not reach the hydrophobic state of pristine PDMS.

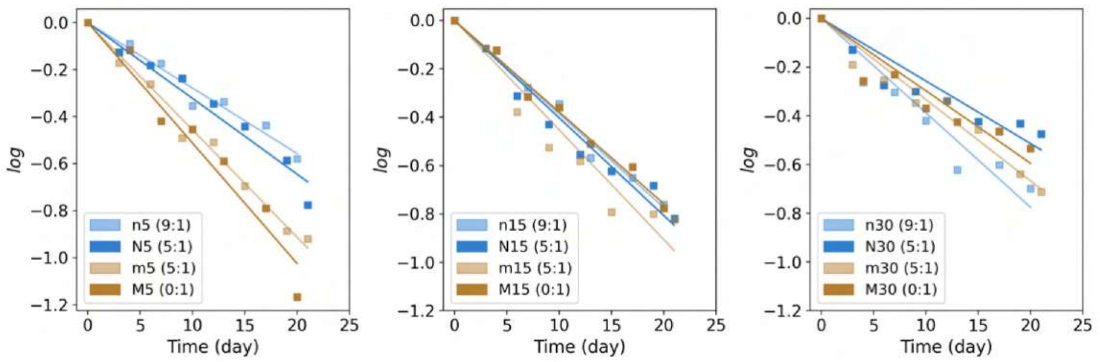

(a) advancing limit

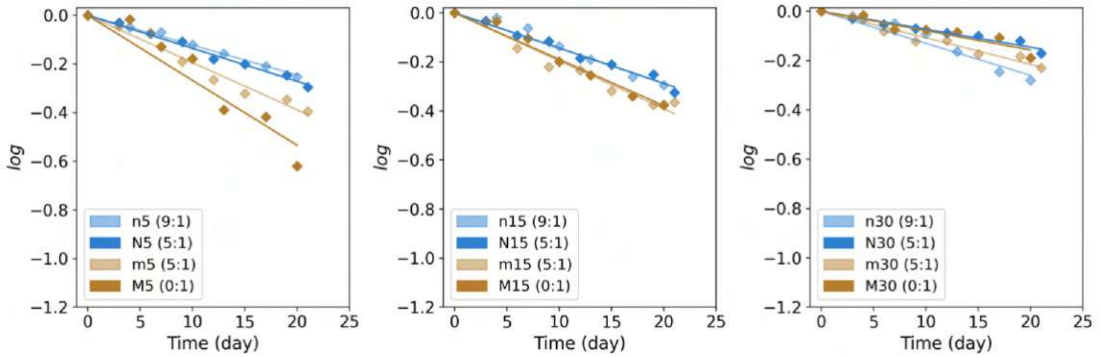

(b) receding limit

Fig. 8.9: Results of $\log(\frac{\gamma-\gamma_p}{\gamma_i-\gamma_p})$ at the (a) advancing limit and (b) receding limit. The inserted lines represent the linear fit. The recovery speed in the first recovery stage is represented by the absolute value of the slope, $1/\tau$.

8.4 Summary

In summary, the effects of film thickness (submicrometer and a few micrometers), dilution ratio, and plasma treatment time on Young's modulus, wettability, hydrophobic recovery, and buckling structure of PDMS were investigated and discussed.

The investigation of Young's modulus on pristine PDMS surface reveals that

- the effective Young's modulus on pristine PDMS shows a strong correlation to the dilution ratio and is independent of film thickness.
  A higher dilution ratio leads to a lower effective Young's modulus of PDMS.

This result provides a new aspect to control the mechanical properties of the PDMS surface by controlling the dilution ratio.

When exposing the PDMS surface to oxygen plasma, the surface wetting property is modified.

- The hydrophilization of PDMS does not depend on the film thickness, dilution ratio, or oxygen plasma treatment time.
- The hydrophobicity recovery process shows a dependency on both film thickness and dilution ratio.
  Thicker PDMS films and less-diluted PDMS films show a higher recovery speed due to their higher reservoirs of low molecular weight species.
- There is a correlation between the hydrophobicity recovery speed and the plasma treatment time, with longer plasma treatment resulting in a slower recovery speed.
- It was observed that the recovery speed has a higher value in the advancing than in the receding limit.

Oxygen plasma treatment can effectively modify the surface topography of PDMS as well, leading to the formation of buckling structures when the critical strain is reached. In this study, the critical strain was achieved with plasma treatment times longer than 15 s. The results that

- The thickness of PDMS has a significant impact on both the waviness and amplitude. A higher thickness results in higher values for both parameters.
- The evolution of the buckling structure over time was investigated, and the results showed that the waviness remained constant while the amplitude decreased.

Overall, oxygen plasma treatment is an effective method for modifying the surface properties of PDMS, with the resulting properties dependent on the dilution ratio and film thickness. Compared to thicker films, submicrometer and micrometer-thick PDMS films exhibit different buckling structures and hydrophobic recovery processes, with smaller waviness in buckling structures and longer recovery times. These findings highlight the importance of film thickness in optimizing the use of PDMS for various applications.

Chapter 9

Conclusion and outlook

Contents

9.1 Summary and Discussion

This study provides precise determinations of CA by controlling the measurement method, surface conditions (roughness and structures), and the environmental factor (such as temperature), and introduces the Friction-Adsorption (FA) model for describing CAs on both experimental flat and structured surfaces across a range of temperatures. The validation of this model is demonstrated through its correlation with electrowetting (EW) performance. In the following, the main results of this work are discussed in detail.

This study addresses the temperature dependency of wetting properties for Teflon AF1600. The CA measurement conditions, namely, the temperature and the speed of the triple line movement were controlled, so that quasi-static conditions were established for the CA determinations. The FA model is developed based on the experimental findings. The FA model describes CAs by introducing a temperature-independent friction force and a temperature-dependent adsorption contribution to the force equilibrium at the triple-line. Both factors are experimentally quantified by measuring the temperature-dependent water CAs on Teflon AF1600. Furthermore, the application of the FA model is extended to describe and predict the EW behavior on Teflon AF1600 at different temperatures. The experimental results show high consistency at a temperature up to 50 °C.

The utility of the FA model is not only confined to pristine surfaces but is also adaptable to plasma-treated surfaces of Teflon AF1600. In contrast to traditional approaches, which rely on area ratios of structurally altered surfaces to depict CAs on plasma-treated surfaces, the FA model provides a more straightforward and accurate characterization of CAs and EW-CAs. An essential pre-requisite is that the surface structures exhibit negligible chemical modifications due to the plasma treatment, thereby ensuring the unchanged adsorption contribution as in the pristine material. Consequently, the plasma treatment predominantly modifies the friction force limit.

Moreover, this study extends its scope beyond surface wettability to investigate other crucial attributes such as surface topographies and chemical compositions. An in-depth understanding of surface modifications induced by oxygen plasma treatment on Teflon

AF1600 and PDMS has been achieved, expanding the understanding of the material-related surface properties.

For Teflon AF1600, oxygen plasma treatment predominantly removes material and induces nanoscaled structures on the surface. The nanoscaled structures can be pillar- or fiber-like, depending on the applied plasma energy. The resulting wetting properties also imply various behavior depending on the plasma energy. With a plasma energy smaller than 1 kJ, the surface exhibits low advancing and zero receding CA. When the energy rises to 3 kJ, super high advancing but zero receding CA are observed. A further increase in the plasma energy ($4.5 - 10$ kJ) results in a surface exhibiting super high advancing and high receding CA. As mentioned before, the chemical analysis is carried out and the results reveal that the functional groups remain unchanged after the plasma treatment. Consequently, the FA model is successfully applied to describe the CAs on plasma-treated surfaces.

Unlike Teflon AF1600, the oxygen plasma does not remove the material of PDMS but creates a stiff oxide layer on the surface. Buckling structures are therefore generated due to the mechanical mismatch between the stiff top oxide layer and the soft PDMS bulk material. The exploration of the CAs following the plasma treatment reveals the hydrophilization of the material. However, this hydrophilicity does not last long, as the hydrophobicity of PDMS recovers over time. High correlations between the hydrophobicity recovery speed and key parameters such as the plasma treatment time, dilution ratio, and film thickness are revealed.

In conclusion, this comprehensive study not only contributes to the fundamental understanding of surface properties for Teflon AF1600 and PDMS but also introduces a novel modeling approach that can be applied to analyze and predict wetting behaviors under varying conditions, paving the way for advancements in surface science and future devices design.

9.2 Outlook

The FA model provides new and valuable insights into describing the CAs and elucidates the precise relationship between the advancing, receding, and Young's CA. It extends to describing CAs across diverse surface conditions – pristine, roughened, and structured – as well as under varying operating conditions, spanning across different temperatures and voltages. This model, combined with the experimental setup will certainly stimulate further research and industry-driven activities in the future.

Nevertheless, like any scientific endeavor, certain aspects await deeper exploration. From a material perspective, expanding the validation of the FA model to encompass a broader spectrum of hydrophobic materials as well as liquids holds promising potential. Such an extension could refine the model's effectiveness and broaden its applicability to diverse materials. Furthermore, the investigation into temperature effects, a critical aspect of wettability, necessitates expanded attention. Although this study achieved high consistency between experimental findings and the FA model between room temperature and 50 °C, the emergence of deviations beyond this temperature requires dedicated investigation. A more expansive examination of temperature impacts, covering a wider range of conditions, is crucial for broadening the model's limitations and boundaries, thereby enhancing its range and accuracy in predicting experimental results. Last but not least, EWOD stands out as a low energy-consume and effective technique for manipulating small liquid volumes and enables numerous applications. In addition to the limited research on the impact of temperature on EWOD behavior, there exist several other facets that warrant a deeper understanding. Notably, the phenomenon of ion trapping emerges when applying a negative voltage to Teflon AF1600 surfaces, leading to a CA higher than predicted. This unexpected and undesired effect has not received sufficient and thorough investigation in the existing literature and requires further studies.

List of Abbreviations

PDD	4,5-difluor-2,2-bis-(trifluormethyl)- 1,3-dioxol
TFE	trafluorethylen
PTFE	polytetrafluorethylen
PFA	perfluoralkoxy-Polymere
PDMS	poly-dimethylsiloxan
EW	electrowetting
EWOD	electrowetting on dielectric
CVD	chemical vapor deposition
PVD	physical vapor deposition
PECVD	plasma enhanced chemical vapor deposition
AFM	atomic force microscope
SEM	scanning electron microscope
SE	secondary electron
FTIR	fourier-transform infrared spectroscopy
ATR-FTIR	attenuated total reflection-fourier-transform infrared spectroscopy
CA	contact angle
WCA	water contact angle
CAH	contact angle hysteresis
CCA	constant contact angle regime
CCR	constant contact radius regime
DI	de-ionized
UV	ultra violet
Ca	Capillary number

List of Symbols

Symbol	Definition	Unit
θ	contact angle	°
θ_{Y}	Young's contact angle	°
θ_{c}	contact angle in Cassie state	°
θ_{w}	contact angle in Wenzel state	°
θ_{adv}	advancing contact angle	°
θ_{rec}	receding contact angle	°
θ_{init}	initial contact angle (for the evaporation process)	°
γ_{sl}	solid-liquid interface tension	mN/m
γ_{sa}	solid-air interface tension	mN/m
γ_{la}	liquid-air interface tension	mN/m
γ_{s}	solid surface tension	mN/m
γ_{s0}	solid surface tension in vacuum	mN/m
f	area coverage of the water-adsorbed area to total available adsorption area	–
e	energy of fully occupied adsorption area	mN/m
F_{f}	static friction-like force	mN/m
F_{fmax}	limit of F_{f}	mN/m
F_{ad}	adsorption contribution	mN/m
F_{el}	electrical energy	mN/m
Ca	Capillary number	–
λ	capillary length	m
μ	dynamic viscosity	Pa · s
v	velocity of triple line	m/s
r	contact radius	m
C	capacitance	F
c	specific capacitance	$\mathrm{F/m^2}$
ϵ_r	dielectric consistent	–
ϵ_0	vacuum permittivity	F/m
U	voltage	U
k_u	speed of voltage change	V/s
R	universal gas constant	J/K/mol
T	temperature	°C
A_m	molar surface area	$\mathrm{m^2/mol}$
N	Avogadro constant	$\mathrm{mol^{-1}}$
M_0	monomer weight	g/mol
ρ	density	$\mathrm{g/m^3}$

Γ	concentration of adsorbed vapor	mol/m^2
p_V	vapor pressure	Pa
p_0	equilibrium vapor pressure	Pa
f_solid	area fraction of solid-contacted area to the projected area in Cassie state	–
f_r	area fraction of contour area to the projected area in Wenzel state	–
W	waviness	nm
A	amplitude	nm
h_s	thickness of stiff silica layer	nm
$\overline{E}_P$	in-plane moduli of PDMS	MPa
$\overline{E}_s$	in-plane moduli of silica layer	MPa
E_P	Young's modulus of PDMS	MPa
E_s	Young's modulus of silica layer	MPa
ν	Poisson's ratio	–
ε	strain	–
ε_c	critical strain	–
$F_{wetting}$	wetting force	N
$F_{buoyancy}$	buoyancy force	N
g	gravity	N
$F_{tensiometer}$	force measured by tensiometer	N
w	width of Wilhelmy plate	m
d	thickness of Wilhelmy plate	m

List of Publications

1. Xiang Y, Fulmek P, Platz D, et al. Temperature dependence of water contact angle on teflon AF1600[J]. Langmuir, 2022, 38(4): 1631-1637.
2. Xiang Y, Fulmek P, Platz D, et al. Temperature-dependent electrowetting behavior on Teflon AF1600[J]. Journal of Materials Science, 2022, 57(31): 15151-15159.
3. Xiang Y, Dejkoski B, Fulmek P, et al. Surface properties of µm and sub-µm polydimethylsiloxane thin films after oxygen plasma treatment[J]. Polymer, 2023, 275: 125915.
4. Xiang Y, Fulmek P, et al. Characterization of Surface Modifications in Oxygen Plasma-Treated Teflon AF1600[J]. Langmuir, 2024.

Bibliography

[1] K.-Y. Law and H. Zhao. *Surface wetting: characterization, contact angle, and fundamentals*. Springer International Publishing Basel, Switzerland, 2016.

[2] T. Young. "III. An essay on the cohesion of fluids". In: *Philosophical transactions of the royal society of London* 95 (1805), pp. 65–87.

[3] M. E. Diaz, J. Fuentes, R. L. Cerro, and M. D. Savage. "Hysteresis during contact angles measurement". In: *Journal of Colloid and Interface Science* 343.2 (2010), pp. 574–583.

[4] H. Eral, D. t Mannetje, and J. M. Oh. "Contact angle hysteresis: a review of fundamentals and applications". In: *Colloid and polymer science* 291.2 (2013), pp. 247–260.

[5] M. Strobel and C. S. Lyons. "An essay on contact angle measurements". In: *Plasma Processes and Polymers* 8.1 (2011), pp. 8–13.

[6] H. Y. Erbil, G. McHale, S. M. Rowan, and M. Newton. "Determination of the receding contact angle of sessile drops on polymer surfaces by evaporation". In: *Langmuir* 15.21 (1999), pp. 7378–7385.

[7] E. Bormashenko, Y. Bormashenko, G. Whyman, R. Pogreb, A. Musin, R. Jager, and Z. Barkay. "Contact angle hysteresis on polymer substrates established with various experimental techniques, its interpretation, and quantitative characterization". In: *Langmuir* 24.8 (2008), pp. 4020–4025.

[8] J. K. Spelt and E. I. Vargha-Butler. "Contact Angle and Liquid Surface Tension Measurements: General Procedures and Techniques". In: *Applied Surface Thermodynamics*. CRC Press, 1996, pp. 397–430.

[9] L. Gao and T. J. McCarthy. "Wetting 101°". In: *Langmuir* 25.24 (2009), pp. 14105–14115.

[10] F. Garbassi, M. Morra, E. Occhiello, and F. Garbassi. "Polymer surfaces: from physics to technology". In: (1998).

[11] Y. Uyama, H. Inoue, K. Ito, A. Kishida, and Y. Ikada. "Comparison of different methods for contact angle measurement". In: *Journal of colloid and interface science* 141.1 (1991), pp. 275–279.

[12] L. M. Lander, L. M. Siewierski, W. J. Brittain, and E. A. Vogler. "A systematic comparison of contact angle methods". In: *Langmuir* 9.8 (1993), pp. 2237–2239.

[13] D. Quéré. "Wetting and roughness". In: *Annu. Rev. Mater. Res.* 38 (2008), pp. 71–99.

[14] J. Woodward, H. Gwin, and D. Schwartz. "Contact angles on surfaces with mesoscopic chemical heterogeneity". In: *Langmuir* 16.6 (2000), pp. 2957–2961.

[15] C. N. Lam, R. Wu, D. Li, M. Hair, and A. Neumann. “Study of the advancing and receding contact angles: liquid sorption as a cause of contact angle hysteresis”. In: *Advances in colloid and interface science* 96.1-3 (2002), pp. 169–191.

[16] P. B. Weisensee, N. K. Neelakantan, K. S. Suslick, A. M. Jacobi, and W. P. King. “Impact of air and water vapor environments on the hydrophobicity of surfaces”. In: *Journal of colloid and interface science* 453 (2015), pp. 177–185.

[17] A. Cassie and S. Baxter. “Wettability of porous surfaces”. In: *Transactions of the Faraday society* 40 (1944), pp. 546–551.

[18] R. N. Wenzel. “Resistance of solid surfaces to wetting by water”. In: *Industrial & Engineering Chemistry* 28.8 (1936), pp. 988–994.

[19] M. Nosonovsky. “On the range of applicability of the Wenzel and Cassie equations”. In: *Langmuir* 23.19 (2007), pp. 9919–9920.

[20] M. V. Panchagnula and S. Vedantam. “Comment on how Wenzel and Cassie were wrong by Gao and McCarthy”. In: *Langmuir* 23.26 (2007), pp. 13242–13242.

[21] L. Gao and T. J. McCarthy. “Reply to “comment on how Wenzel and Cassie were wrong by Gao and McCarthy””. In: *Langmuir* 23.26 (2007), pp. 13243–13243.

[22] G. McHale. “Cassie and Wenzel: were they really so wrong?” In: *Langmuir* 23.15 (2007), pp. 8200–8205.

[23] A. Ponter and A. Boyes. “Temperature dependence of contact angles of water on a low energy surface under conditions of condensation and at reduced pressures”. In: *Nature Physical Science* 231.24 (1971), pp. 152–153.

[24] M. Tadros, P. Hu, and A. Adamson. “Adsorption and contact angle studies: I. Water on smooth carbon, linear polyethylene, and stearic acid-coated copper”. In: *Journal of colloid and interface science* 49.2 (1974), pp. 184–195.

[25] M. Phillips and A. Riddiford. “Temperature dependence of contact angles”. In: *Nature* 205.4975 (1965), pp. 1005–1006.

[26] J. B. Jones and A. W. Adamson. “Temperature dependence of contact angle and of interfacial free energies in the naphthalene-water-air system”. In: *The Journal of Physical Chemistry* 72.2 (1968), pp. 646–650.

[27] T. Hayashi, T. Hazuku, T. Takamasa, and K. Takamori. “Contact angle of water droplets in a high-temperature, high-pressure environment”. In: *International Conference on Nuclear Engineering*. Vol. 46873. 2004, pp. 797–800.

[28] J.-W. Song, D.-L. Zeng, and L.-W. Fan. “Temperature dependence of contact angles of water on a stainless steel surface at elevated temperatures and pressures: In situ characterization and thermodynamic analysis”. In: *Journal of colloid and interface science* 561 (2020), pp. 870–880.

[29] Y. Hirose, T. Hayashi, T. Hazuku, and T. Takamasa. “Experimental study on contact angle of water droplet in high-temperature condition”. In: *International Conference on Nuclear Engineering*. Vol. 42452. 2006, pp. 709–716.

[30] K. L. Osborne. “Temperature-dependence of the contact angle of water on graphite, silicon, and gold”. PhD thesis. Worcester Polytechnic Institute Worcester, MA, 2009.

[31] J. M. Grace and L. J. Gerenser. “Plasma treatment of polymers”. In: *Journal of dispersion science and technology* 24.3-4 (2003), pp. 305–341.

[32] L. R. Scarratt, B. S. Hoatson, E. S. Wood, B. S. Hawkett, and C. Neto. “Durable superhydrophobic surfaces via spontaneous wrinkling of teflon AF”. In: *ACS applied materials & interfaces* 8.10 (2016), pp. 6743–6750.

[33] N. Frøvik, M. Greve, and L. Helseth. “Nanostructures and wetting properties controlled by reactive ion etching of fluorinated ethylene propylene”. In: *Colloids and Surfaces A: Physicochemical and Engineering Aspects* 574 (2019), pp. 228–238.

[34] X. Guo and L. E. Helseth. “Optical and wetting properties of nanostructured fluorinated ethylene propylene changed by mechanical deformation and its application in triboelectric nanogenerators”. In: *Materials Research Express* 2.1 (2015), p. 015302.

[35] H. M. Powell and J. J. Lannutti. “Nanofibrillar surfaces via reactive ion etching”. In: *Langmuir* 19.21 (2003), pp. 9071–9078.

[36] T. Takahashi, Y. Hirano, Y. Takasawa, T. Gowa, N. Fukutake, A. Oshima, S. Tagawa, and M. Washio. “Change in surface morphology of polytetrafluoroethylene by reactive ion etching”. In: *Radiation Physics and Chemistry* 80.2 (2011), pp. 253–256.

[37] J. Ryu, K. Kim, J. Park, B. G. Hwang, Y. Ko, H. Kim, J. Han, E. Seo, Y. Park, and S. J. Lee. “Nearly perfect durable superhydrophobic surfaces fabricated by a simple one-step plasma treatment”. In: *Scientific reports* 7.1 (2017), pp. 1–8.

[38] Y. Xiang, B. Dejkoski, P. Fulmek, and U. Schmid. “Surface properties of μm and sub-μm polydimethylsiloxane thin films after oxygen plasma treatment”. In: *Polymer* (2023), p. 125915.

[39] E. A. Carbone, N. Boucher, M. Sferrazza, and F. Reniers. “How to increase the hydrophobicity of PTFE surfaces using an rf atmospheric-pressure plasma torch”. In: *Surface and interface analysis* 42.6-7 (2010), pp. 1014–1018.

[40] E. Wohlfart, J. P. Fernández-Blázquez, E. Arzt, and A. del Campo. “Nanofibrillar patterns on PET: the influence of plasma parameters in surface morphology”. In: *Plasma Processes and Polymers* 8.9 (2011), pp. 876–884.

[41] V. Jain, T. P. Raj, R. Deshmukh, and R. Patrikar. “Design, fabrication and characterization of low cost printed circuit board based EWOD device for digital microfluidics applications”. In: *Microsystem Technologies* 23.2 (2017), pp. 389–397.

[42] F. Mugele and J.-C. Baret. “Electrowetting: from basics to applications”. In: *Journal of physics: condensed matter* 17.28 (2005), R705.

[43] J. Li et al. “Current commercialization status of electrowetting-on-dielectric (EWOD) digital microfluidics”. In: *Lab on a Chip* 20.10 (2020), pp. 1705–1712.

[44] B. Berge and J. Peseux. “Variable focal lens controlled by an external voltage: An application of electrowetting”. In: *The European Physical Journal E* 3.2 (2000), pp. 159–163.

[45] S. Terrab, A. M. Watson, C. Roath, J. T. Gopinath, and V. M. Bright. “Adaptive electrowetting lens-prism element”. In: *Optics express* 23.20 (2015), pp. 25838–25845.

[46] T. Roques-Carmes, A. Gigante, J.-M. Commenge, and S. Corbel. “Use of surfactants to reduce the driving voltage of switchable optical elements based on electrowetting”. In: *Langmuir* 25.21 (2009), pp. 12771–12779.

[47] W. Y. Lim, O. D. Supekar, M. Zohrabi, J. T. Gopinath, and V. M. Bright. “Liquid combination with high refractive index contrast and fast scanning speeds for electrowetting adaptive optics”. In: *Langmuir* 34.48 (2018), pp. 14511–14518.

[48] H. Huang and Y. Zhao. “Optofluidic lenses for 2D and 3D imaging”. In: *Journal of Micromechanics and Microengineering* 29.7 (2019), p. 073001.

[49] F. Li and F. Mugele. “How to make sticky surfaces slippery: Contact angle hysteresis in electrowetting with alternating voltage”. In: *Applied Physics Letters* 92.24 (2008), p. 244108.

[50] M. H. Merrill, R. C. Reid, N. Gogotsi, and J. P. Thomas. “Electrowetting on polyimide and silicon substrates with high hysteresis”. In: *Microsystem Technologies* 24.12 (2018), pp. 4847–4854.

[51] R. C. Reid, M. H. Merrill, and J. P. Thomas. “Stick–slip behavior during electrowetting-on-dielectric: polarization and substrate effects”. In: *Microfluidics and Nanofluidics* 24.10 (2020), pp. 1–9.

[52] S. M. Wadhai, Y. B. Sawane, and A. G. Banpurkar. “Electrowetting behaviour of thermostable liquid over wide temperature range”. In: *Journal of Materials Science* 55.6 (2020), pp. 2365–2371.

[53] A. G. Banpurkar, Y. Sawane, S. M. Wadhai, C. Murade, I. Siretanu, D. van den Ende, and F. Mugele. “Spontaneous electrification of fluoropolymer–water interfaces probed by electrowetting”. In: *Faraday discussions* 199 (2017), pp. 29–47.

[54] D. L. Herbertson, C. R. Evans, N. J. Shirtcliffe, G. McHale, and M. I. Newton. “Electrowetting on superhydrophobic SU-8 patterned surfaces”. In: *Sensors and Actuators A: Physical* 130 (2006), pp. 189–193.

[55] J. Heikenfeld and M. Dhindsa. “Electrowetting on superhydrophobic surfaces: present status and prospects”. In: *Journal of Adhesion Science and Technology* 22.3-4 (2008), pp. 319–334.

[56] R. Roy, J. A. Weibel, and S. V. Garimella. “Re-entrant cavities enhance resilience to the Cassie-to-Wenzel state transition on superhydrophobic surfaces during electrowetting”. In: *Langmuir* 34.43 (2018), pp. 12787–12793.

[57] M. S. Dhindsa, N. R. Smith, J. Heikenfeld, P. D. Rack, J. D. Fowlkes, M. J. Doktycz, A. V. Melechko, and M. L. Simpson. “Reversible electrowetting of vertically aligned superhydrophobic carbon nanofibers”. In: *Langmuir* 22.21 (2006), pp. 9030–9034.

[58] P.-G. De Gennes. “Wetting: statics and dynamics”. In: *Reviews of modern physics* 57.3 (1985), p. 827.

[59] K. L. Mittal. *Contact Angle, Wettability and Adhesion, Volume 3*. CRC Press, 2003.

[60] R. B. Center. “Contact angle, wettability and adhesion”. In: (1964).

[61] A. Lafuma and D. Quéré. “Superhydrophobic states”. In: *Nature materials* 2.7 (2003), pp. 457–460.

[62] R. E. Johnson Jr and R. H. Dettre. “Contact angle hysteresis: I. Study of an idealized rough surface”. In: ACS Publications, 1964.

[63] T. Onda, S. Shibuichi, N. Satoh, and K. Tsujii. “Super-water-repellent fractal surfaces”. In: *Langmuir* 12.9 (1996), pp. 2125–2127.

[64] S. Shibuichi, T. Onda, N. Satoh, and K. Tsujii. “Super water-repellent surfaces resulting from fractal structure”. In: *The Journal of Physical Chemistry* 100.50 (1996), pp. 19512–19517.

[65] C. Neinhuis and W. Barthlott. “Characterization and distribution of water-repellent, self-cleaning plant surfaces”. In: *Annals of botany* 79.6 (1997), pp. 667–677.

[66] J. Bico, C. Marzolin, and D. Quéré. “Pearl drops”. In: *EPL (Europhysics Letters)* 47.2 (1999), p. 220.

[67] D. Öner and T. J. McCarthy. “Ultrahydrophobic surfaces. Effects of topography length scales on wettability”. In: *Langmuir* 16.20 (2000), pp. 7777–7782.

[68] Z. Yoshimitsu, A. Nakajima, T. Watanabe, and K. Hashimoto. “Effects of surface structure on the hydrophobicity and sliding behavior of water droplets”. In: *Langmuir* 18.15 (2002), pp. 5818–5822.

[69] D. Y. Kwok and A. W. Neumann. “Contact angle measurement and contact angle interpretation”. In: *Advances in colloid and interface science* 81.3 (1999), pp. 167–249.

[70] A. Neumann and R. Good. “Thermodynamics of contact angles. I. Heterogeneous solid surfaces”. In: *Journal of Colloid and Interface Science* 38.2 (1972), pp. 341–358.

[71] R. J. Good. “Contact angle, wetting, and adhesion: a critical review”. In: *Journal of adhesion science and technology* 6.12 (1992), pp. 1269–1302.

[72] J. Eick, R. Good, and A. Neumann. “Thermodynamics of contact angles. II. Rough solid surfaces”. In: *Journal of Colloid and Interface Science* 53.2 (1975), pp. 235–248.

[73] S. Zhang, Z. Yi, L. Mingchao, A. H. Dorian, and G. Yixiang. “Dynamic contact angle hysteresis in liquid bridges”. In: *Colloids ans Surfaces A* 555 (2018), pp. 365–371.

[74] C. Extrand. “A thermodynamic model for contact angle hysteresis”. In: *Journal of Colloid and interface Science* 207.1 (1998), pp. 11–19.

[75] J. Joanny and P.-G. De Gennes. “A model for contact angle hysteresis”. In: *The journal of chemical physics* 81.1 (1984), pp. 552–562.

[76] N. A. Patankar. “Hysteresis with regard to Cassie and Wenzel states on superhydrophobic surfaces”. In: *Langmuir* 26.10 (2010), pp. 7498–7503.

[77] L. Gao and T. J. McCarthy. “How Wenzel and Cassie were wrong”. In: *Langmuir* 23.7 (2007), pp. 3762–3765.

[78] S. Parvate, P. Dixit, and S. Chattopadhyay. “Superhydrophobic surfaces: insights from theory and experiment”. In: *The Journal of Physical Chemistry B* 124.8 (2020), pp. 1323–1360.

[79] G. L. Mack and D. A. Lee. “The determination of contact angles from measurements of the dimensions of small bubbles and drops. II. The sessile drop method for obtuse angles”. In: *The Journal of Physical Chemistry* 40.2 (2002), pp. 169–176.

[80] A. Neumann and R. Good. “Techniques of measuring contact angles”. In: *Surface and Colloid Science: Volume 11: Experimental Methods* (1979), pp. 31–91.

[81] A. Skłodowska, M. Woźniak, and R. Matlakowska. “The method of contact angle measurements and estimation of work of adhesion in bioleaching of metals”. In: *Biological procedures online* 1 (1999), pp. 114–121.

[82] V. A. Lubarda and K. A. Talke. “Analysis of the equilibrium droplet shape based on an ellipsoidal droplet model”. In: *Langmuir* 27.17 (2011), pp. 10705–10713.

[83] Y. Rotenberg, L. Boruvka, and A. Neumann. “Determination of surface tension and contact angle from the shapes of axisymmetric fluid interfaces”. In: *Journal of colloid and interface science* 93.1 (1983), pp. 169–183.

[84] O. Del Rıo and A. Neumann. “Axisymmetric drop shape analysis: computational methods for the measurement of interfacial properties from the shape and dimensions of pendant and sessile drops”. In: *Journal of colloid and interface science* 196.2 (1997), pp. 136–147.

[85] F. Skinner, Y. Rotenberg, and A. Neumann. “Contact angle measurements from the contact diameter of sessile drops by means of a modified axisymmetric drop shape analysis”. In: *Journal of colloid and interface science* 130.1 (1989), pp. 25–34.

[86] D. C. Pease. “The significance of the contact angle in relation to the solid surface”. In: *The Journal of Physical Chemistry* 49.2 (1945), pp. 107–110.

[87] M. Morra, E. Occhiello, and F. Garbassi. “Knowledge about polymer surfaces from contact angle measurements”. In: *Advances in Colloid and Interface Science* 32.1 (1990), pp. 79–116.

[88] F. Bartell and A. D. Wooley. “Solid—Liquid—Air Contact Angles and their Dependence upon the Surface Condition of the Solid”. In: *Journal of the American Chemical Society* 55.9 (1933), pp. 3518–3527.

[89] L. Rayleigh. “XLIII. On the tension of water surfaces, clean and contaminated, investigated by the method of ripples”. In: *The London, Edinburgh, and Dublin Philosophical Magazine and Journal of Science* 30.186 (1890), pp. 386–400.

[90] R. Good. “CONTACT-ANGLE, WETTING, AND ADHESION-A CRITICAL-REVIEW (VOL 6, PG 1269-1302, 1992)”. In: *Journal of Adhesion Science and Technology* 7.9 (1993), pp. 1015–1015.

[91] K. L. Sutherland and I. W. Wark. “Principles of flotation”. In: Australasian Institute of Mining and Metallurgy. 1955.

[92] L. Wilhelmy. “Ueber die Abhängigkeit der Capillaritäts-Constanten des Alkohols von Substanz und Gestalt des benetzten festen Körpers”. In: *Annalen der Physik* 195.6 (1863), pp. 177–217.

[93] L. Chen and E. Bonaccurso. “Electrowetting—From statics to dynamics”. In: *Advances in colloid and interface science* 210 (2014), pp. 2–12.

[94] B. Hendriks, S. Kuiper, M. Van As, C. Renders, and T. Tukker. “Electrowetting-based variable-focus lens for miniature systems”. In: *Optical review* 12.3 (2005), pp. 255–259.

[95] Y. Takai, R. Koshiishi, S. Kirita, M. Tsuchiya, Y. Watanabe, K. Takahashi, Y. Imai, and Y. Shimpuku. “Electrowetting fresnel lenticular”. In: *2012 IEEE 25th International Conference on Micro Electro Mechanical Systems (MEMS)*. IEEE. 2012, pp. 632–635.

[96] M. E. Diaz, M. D. Savage, and R. L. Cerro. “The effect of temperature on contact angles and wetting transitions for n-alkanes on PTFE”. In: *Journal of colloid and interface science* 503 (2017), pp. 159–167.

[97] D. Sullivan. “Surface tension and contact angle of a liquid–solid interface”. In: *The Journal of chemical physics* 74.4 (1981), pp. 2604–2615.

[98] J.-W. Song and L.-W. Fan. “Temperature dependence of the contact angle of water: a review of research progress, theoretical understanding, and implications for boiling heat transfer”. In: *Advances in Colloid and Interface Science* 288 (2021), p. 102339.

[99] C.-Y. Hui and A. Jagota. “Surface tension, surface energy, and chemical potential due to their difference”. In: *Langmuir* 29.36 (2013), pp. 11310–11316.

[100] C. E. Stauffer. “The measurement of surface tension by the pendant drop technique”. In: *The journal of physical chemistry* 69.6 (1965), pp. 1933–1938.

[101] J. D. Berry, M. J. Neeson, R. R. Dagastine, D. Y. Chan, and R. F. Tabor. “Measurement of surface and interfacial tension using pendant drop tensiometry”. In: *Journal of colloid and interface science* 454 (2015), pp. 226–237.

[102] W. A. Zisman. “Relation of the equilibrium contact angle to liquid and solid constitution”. In: ACS Publications, 1964.

[103] F. M. Fowkes. “Determination of interfacial tensions, contact angles, and dispersion forces in surfaces by assuming additivity of intermolecular interactions in surfaces”. In: *The Journal of Physical Chemistry* 66.2 (1962), pp. 382–382.

[104] F. M. Fowkes. “Attractive forces at interfaces”. In: *Industrial & Engineering Chemistry* 56.12 (1964), pp. 40–52.

[105] F. M. Fowkes. “Donor-acceptor interactions at interfaces”. In: *The Journal of Adhesion* 4.2 (1972), pp. 155–159.

[106] Y. Kitazaki and T. Hata. “Surface-chemical criteria for optimum adhesion: Ii. the variability of critical surface tension (γc) and its choice”. In: *The Journal of Adhesion* 4.2 (1972), pp. 123–132.

[107] C. Van Oss, R. Good, and M. Chaudhury. “The role of van der Waals forces and hydrogen bonds in “hydrophobic interactions” between biopolymers and low energy surfaces”. In: *Journal of colloid and Interface Science* 111.2 (1986), pp. 378–390.

[108] C. J. Van Oss, M. K. Chaudhury, and R. J. Good. “Interfacial Lifshitz-van der Waals and polar interactions in macroscopic systems”. In: *Chemical reviews* 88.6 (1988), pp. 927–941.

[109] C. J. Van Oss. *Interfacial forces in aqueous media*. CRC press, 2006.

[110] A. Neumann, R. Good, C. Hope, and M. Sejpal. “An equation-of-state approach to determine surface tensions of low-energy solids from contact angles”. In: *Journal of colloid and interface science* 49.2 (1974), pp. 291–304.

[111] D. Li and A. Neumann. “A reformulation of the equation of state for interfacial tensions”. In: *Journal of Colloid and Interface Science* 137.1 (1990), pp. 304–307.

[112] P.-J. Sell and A. Neumann. “The surface tension of solids”. In: *Angewandte Chemie International Edition in English* 5.3 (1966), pp. 299–307.

[113] Dupré. *Théorie mécanique de la chaleur*. Gauthier-Villars, 1869.

[114] D. Ahmad, I. van den Boogaert, J. Miller, R. Presswell, and H. Jouhara. “Hydrophilic and hydrophobic materials and their applications”. In: *Energy Sources, Part A: Recovery, Utilization, and Environmental Effects* 40.22 (2018), pp. 2686–2725.

[115] S.-J. Ding, P.-F. Wang, X.-G. Wan, D. W. Zhang, J.-T. Wang, and W. W. Lee. “Effects of thermal treatment on porous amorphous fluoropolymer film with a low dielectric constant”. In: *Materials Science and Engineering: B* 83.1-3 (2001), pp. 130–136.

[116] *Teflon AF, Amorphous Fluoroplastic Resins*. `teflon-af-product-info.pdf`, available at `www.teflon.com`. Chemours Company FC. 2016.

[117] J. Scheirs. *Modern fluoropolymers: high performance polymers for diverse applications*. Wiley, 1997.

[118] N. J. Bazin, J. E. Andrew, and H. A. McInnes. “Formation of Teflon AF polymer thin films as optical coatings in the high-peak-power laser field”. In: *Third International Conference on Solid State Lasers for Application to Inertial Confinement Fusion*. Vol. 3492. International Society for Optics and Photonics. 1999, pp. 964–969.

[119] D. C. Hyun and U. Jeong. “Substrate thickness: An effective control parameter for polymer thin film buckling on PDMS substrates”. In: *Journal of applied polymer science* 112.5 (2009), pp. 2683–2690.

[120] M. Liu, J. Sun, Y. Sun, C. Bock, and Q. Chen. “Thickness-dependent mechanical properties of polydimethylsiloxane membranes”. In: *Journal of micromechanics and microengineering* 19.3 (2009), p. 035028.

[121] E. S. Kim, S. H. Kim, S.-J. Lee, J. H. Lee, M. Byeon, D. H. Suh, and W. J. Choi. “Facile fabrication of micro/nano-structured wrinkles by controlling elastic properties of polydimethylsiloxane substrates”. In: *Polymer* 212 (2021), p. 123087.

[122] L. Nguyen, M. Hang, W. Wang, Y. Tian, L. Wang, T. J. McCarthy, and W. Chen. “Simple and Improved Approaches to Long-Lasting, Hydrophilic Silicones Derived from Commercially Available Precursors”. In: *ACS Applied Materials & Interfaces* 6.24 (2014), pp. 22876–22883.

[123] N. Bhandaru, N. Agrawal, M. Banik, R. Mukherjee, and A. Sharma. “Hydrophobic recovery of cross-linked polydimethylsiloxane films and its consequence in soft nano patterning”. In: *Bulletin of Materials Science* 43.1 (2020), pp. 1–10.

[124] A. Tserepi, E. Gogolides, K. Tsougeni, V. Constantoudis, and E. S. Valamontes. “Tailoring the surface topography and wetting properties of oxygen-plasma treated polydimethylsiloxane”. In: *Journal of applied physics* 98.11 (2005), p. 113502.

[125] A. Chiche, C. M. Stafford, and J. T. Cabral. “Complex micropatterning of periodic structures on elastomeric surfaces”. In: *Soft Matter* 4.12 (2008), pp. 2360–2364.

[126] Y. Li, S. Dai, J. John, and K. R. Carter. “Superhydrophobic surfaces from hierarchically structured wrinkled polymers”. In: *ACS applied materials & interfaces* 5.21 (2013), pp. 11066–11073.

[127] K. Efimenko, J. Finlay, M. E. Callow, J. A. Callow, and J. Genzer. “Development and testing of hierarchically wrinkled coatings for marine antifouling”. In: *ACS applied materials & interfaces* 1.5 (2009), pp. 1031–1040.

[128] I. Miranda, A. Souza, P. Sousa, J. Ribeiro, E. M. Castanheira, R. Lima, and G. Minas. “Properties and applications of PDMS for biomedical engineering: A review”. In: *Journal of Functional Biomaterials* 13.1 (2021), p. 2.

[129] Q. Wang, G. Sun, Q. Tong, W. Yang, and W. Hao. “Fluorine-free superhydrophobic coatings from polydimethylsiloxane for sustainable chemical engineering: Preparation methods and applications”. In: *Chemical Engineering Journal* 426 (2021), p. 130829.

[130] C. Yu, K. O’Brien, Y.-H. Zhang, H. Yu, and H. Jiang. “Tunable optical gratings based on buckled nanoscale thin films on transparent elastomeric substrates”. In: *Applied Physics Letters* 96.4 (2010), p. 041111.

[131] A. Tan, L. Pellegrino, and J. T. Cabral. “Tunable Phase Gratings by Wrinkling of Plasma-Oxidized PDMS: Gradient Skins and Multiaxial Patterns”. In: *ACS Applied Polymer Materials* 3.10 (2021), pp. 5162–5170.

[132] J. C. McDonald and G. M. Whitesides. “Poly (dimethylsiloxane) as a material for fabricating microfluidic devices”. In: *Accounts of chemical research* 35.7 (2002), pp. 491–499.

[133] M. P. Wolf, G. B. Salieb-Beugelaar, and P. Hunziker. “PDMS with designer functionalities—Properties, modifications strategies, and applications”. In: *Progress in Polymer Science* 83 (2018), pp. 97–134.

[134] A. K. Singh et al. “Polydimethylsiloxane based sustainable hydrophobic/oleophilic coatings for oil/water separation: A mini review”. In: *Cleaner Materials* (2022), p. 100136.

[135] J. A. Rogers, T. Someya, and Y. Huang. “Materials and mechanics for stretchable electronics”. In: *science* 327.5973 (2010), pp. 1603–1607.

[136] T. Sathe and D. Bodas. “Development and characterization of a polydimethylsiloxane-cellulose acetate hybrid membrane for application in organ-on-a-chip”. In: *Materials Science and Engineering: B* 291 (2023), p. 116366.

[137] Y. Xiang, P. Fulmek, D. Platz, and U. Schmid. “Temperature Dependence of Water Contact Angle on Teflon AF1600”. In: *Langmuir* 38.4 (2022), pp. 1631–1637.

[138] H.-J. Butt and M. Kappl. *Surface and interfacial forces*. Wiley Online Library, 2010.

[139] Y. Xiang, P. Fulmek, D. Platz, and U. Schmid. “Temperature-dependent electrowetting behavior on Teflon AF1600”. In: *Journal of Materials Science* (2022), pp. 1–9.

[140] Y. Xiang, B. Dejkoski, P. Fulmek, and U. Schmid. “Surface properties of µm and sub-µm polydimethylsiloxane thin films after oxygen plasma treatment”. In: *Polymer* (2023), p. 125915. ISSN: 0032-3861. DOI: `https://doi.org/10.1016/j.polymer.2023.125915`. URL: `https://www.sciencedirect.com/science/article/pii/S0032386123002458`.

[141] T. Betancourt and L. Brannon-Peppas. “Micro-and nanofabrication methods in nanotechnological medical and pharmaceutical devices”. In: *International journal of nanomedicine* 1.4 (2006), p. 483.

[142] G. T. Kovacs et al. *Micromachined transducers sourcebook*. Vol. 2. WCB/McGraw-Hill New York, 1998.

[143] T. J. R. Christian Koch. *Photolithography. Basics of microstructuring*. MicroChemicals, 2017.

[144] M. J. Madou. *Fundamentals of microfabrication: the science of miniaturization*. CRC press, 2002.

[145] M. N. Chaudhari, R. B. Ahirrao, and S. D. Bagul. “Thin film Deposition Methods: A Critical Review”. In: ().

[146] D. Depla, S. Mahieu, et al. *Reactive sputter deposition*. Vol. 109. Springer, 2008.

[147] H. Mustafa and D. A. Jameel. “Modeling and the main stages of spin coating process: A review”. In: *J. Appl. Sci. Technol. Trends* 2.3 (2021), pp. 91–95.

[148] M. Köhler. *Etching in microsystem technology*. John Wiley & Sons, 2008.

[149] W. Menz, J. Mohr, and O. Paul. *Microsystem technology*. John Wiley & Sons, 2008.

[150] A. L. Thangawng, R. S. Ruoff, M. A. Swartz, and M. R. Glucksberg. “An ultra-thin PDMS membrane as a bio/micro–nano interface: fabrication and characterization”. In: *Biomedical microdevices* 9.4 (2007), pp. 587–595.

[151] B. Sarrazin, R. Brossard, P. Guenoun, and F. Malloggi. “Investigation of PDMS based bi-layer elasticity via interpretation of apparent Young’s modulus”. In: *Soft Matter* 12.7 (2016), pp. 2200–2207.

[152] F. A. Bayley, J. L. Liao, P. N. Stavrinou, A. Chiche, and J. T. Cabral. “Wavefront kinetics of plasma oxidation of polydimethylsiloxane: limits for sub-μm wrinkling”. In: *Soft matter* 10.8 (2014), pp. 1155–1166.

[153] B. A. Glatz and A. Fery. "The influence of plasma treatment on the elasticity of the in situ oxidized gradient layer in PDMS: Towards crack-free wrinkling". In: *Soft Matter* 15.1 (2019), pp. 65–72.

[154] K.-Y. Law and H. Zhao. "Determination of solid surface tension by contact angle". In: *Surface Wetting*. Springer, 2016, pp. 135–148.

[155] B.-B. Lee, P. Ravindra, and E.-S. Chan. "A critical review: surface and interfacial tension measurement by the drop weight method". In: *Chemical Engineering Communications* 195.8 (2008), pp. 889–924.

[156] C. Huh and S. Mason. "Sphere tensiometry: an evaluation and critique". In: *Canadian Journal of Chemistry* 54.6 (1976), pp. 969–978.

[157] J. W. Drelich, L. Boinovich, E. Chibowski, C. Della Volpe, L. Hołysz, A. Marmur, and S. Siboni. "Contact angles: History of over 200 years of open questions". In: *Surface Innovations* 8.1–2 (2019), pp. 3–27.

[158] B. E. Rapp. *Microfluidics: modeling, mechanics and mathematics*. William Andrew, 2016.

[159] A. Günther and K. F. Jensen. "Multiphase microfluidics: from flow characteristics to chemical and materials synthesis". In: *Lab on a Chip* 6.12 (2006), pp. 1487–1503.

[160] L. Gao and T. J. McCarthy. "Contact angle hysteresis explained". In: *Langmuir* 22.14 (2006), pp. 6234–6237.

[161] C. Bourges-Monnier and M. Shanahan. "Influence of evaporation on contact angle". In: *Langmuir* 11.7 (1995), pp. 2820–2829.

[162] J. M. Stauber, S. K. Wilson, B. R. Duffy, and K. Sefiane. "On the lifetimes of evaporating droplets with related initial and receding contact angles". In: *Physics of fluids* 27.12 (2015), p. 122101.

[163] J.-H. Kim, S. I. Ahn, J. H. Kim, and W.-C. Zin. "Evaporation of water droplets on polymer surfaces". In: *Langmuir* 23.11 (2007), pp. 6163–6169.

[164] T. Furuta, M. Sakai, T. Isobe, and A. Nakajima. "Evaporation behavior of microliter- and sub-nanoliter-scale water droplets on two different fluoroalkylsilane coatings". In: *Langmuir* 25.20 (2009), pp. 11998–12001.

[165] S. Ramos, J. Dias, and B. Canut. "Drop evaporation on superhydrophobic PTFE surfaces driven by contact line dynamics". In: *Journal of colloid and interface science* 440 (2015), pp. 133–139.

[166] A. Mohammed and A. Abdullah. "Scanning electron microscopy (SEM): A review". In: *Proceedings of the 2018 International Conference on Hydraulics and Pneumatics—HERVEX, Băile Govora, Romania*. 2018, pp. 7–9.

[167] N. Gupta, M. Kavya, Y. R. Singh, J. Jyothi, and H. C. Barshilia. "Superhydrophobicity on transparent fluorinated ethylene propylene films with nano-protrusion morphology by Ar+ O2 plasma etching: study of the degradation in hydrophobicity after exposure to the environment". In: *Journal of Applied Physics* 114.16 (2013), p. 164307.

[168] K. D. Vernon-Parry. "Scanning electron microscopy: an introduction". In: *III-Vs Review* 13.4 (2000), pp. 40–44.

[169] J. I. Goldstein, D. E. Newbury, J. R. Michael, N. W. Ritchie, J. H. J. Scott, and D. C. Joy. *Scanning electron microscopy and X-ray microanalysis*. Springer, 2017.

[170] D. Rugar and P. Hansma. "Atomic force microscopy". In: *Physics today* 43.10 (1990), pp. 23–30.

[171] P. Eaton and P. West. *Atomic force microscopy*. Oxford university press, 2010.

[172] M. Griepentrog, G. Krämer, and B. Cappella. "Comparison of nanoindentation and AFM methods for the determination of mechanical properties of polymers". In: *Polymer testing* 32.3 (2013), pp. 455–460.

[173] S. Kasas, G. Longo, and G. Dietler. "Mechanical properties of biological specimens explored by atomic force microscopy". In: *Journal of Physics D: Applied Physics* 46.13 (2013), p. 133001.

[174] P. Hermanowicz, M. Sarna, K. Burda, and H. Gabryś. "AtomicJ: an open source software for analysis of force curves". In: *Review of Scientific Instruments* 85.6 (2014), p. 063703.

[175] F. Rico, P. Roca-Cusachs, N. Gavara, R. Farré, M. Rotger, and D. Navajas. "Probing mechanical properties of living cells by atomic force microscopy with blunted pyramidal cantilever tips". In: *Phys. Rev. E* 72 (2 2005), p. 021914. DOI: `10.1103/PhysRevE.72.021914`. URL: `https://link.aps.org/doi/10.1103/PhysRevE.72.021914`.

[176] N. Vandencasteele and F. Reniers. "Plasma-modified polymer surfaces: Characterization using XPS". In: *Journal of Electron Spectroscopy and Related Phenomena* 178 (2010), pp. 394–408.

[177] P. R. Griffiths. "Fourier transform infrared spectrometry". In: *Science* 222.4621 (1983), pp. 297–302.

[178] J. Madejová. "FTIR techniques in clay mineral studies". In: *Vibrational spectroscopy* 31.1 (2003), pp. 1–10.

[179] Z. Movasaghi, S. Rehman, and D. I. ur Rehman. "Fourier transform infrared (FTIR) spectroscopy of biological tissues". In: *Applied Spectroscopy Reviews* 43.2 (2008), pp. 134–179.

[180] A. McClelland, E. Bulat, B. Bernier, and E. L. Murphy. "Specular reflection FTIR: A non-contact method for analyzing coatings on photographs and other cultural materials". In: *Journal of the American Institute for Conservation* 59.2 (2020), pp. 123–136.

[181] F. A. Stevie and C. L. Donley. "Introduction to x-ray photoelectron spectroscopy". In: *Journal of Vacuum Science & Technology A: Vacuum, Surfaces, and Films* 38.6 (2020), p. 063204.

[182] *X-ray photoelectron spectroscopy*. URL: `https://serc.carleton.edu/msu_nanotech/methods/xps.html`.

[183] P. Van der Heide. *X-ray photoelectron spectroscopy: an introduction to principles and practices*. John Wiley & Sons, 2011.

[184] R. Sedev, C. Budziak, J. Petrov, and A. Neumann. "Dynamic contact angles at low velocities". In: *Journal of colloid and interface science* 159.2 (1993), pp. 392–399.

[185] G. Callegari, A. Calvo, and J. Hulin. "Contact line motion: Hydrodynamical or molecular process?" In: *Contact Angle, Wettability and Adhesion, Volume 4* 4 (2006), p. 29.

[186] J.-B. Valsamis, M. De Volder, and P. Lambert. "Physical background". In: *Surface Tension in Microsystems*. Springer, 2013, pp. 3–16.

[187] T. Petrova and R. Dooley. "Revised release on surface tension of ordinary water substance". In: *Proceedings of the International Association for the Properties of Water and Steam, Moscow, Russia* (2014), pp. 23–27.

[188] F. Fowkes, D. McCarthy, and M. Mostafa. "Contact angles and the equilibrium spreading pressures of liquids on hydrophobic solids". In: *Journal of colloid and interface science* 78.1 (1980), pp. 200–206.

[189] J. Chessick, F. Healey, and A. Zettlemoyer. "Adsorption and heat of wetting studies of teflon". In: *The Journal of Physical Chemistry* 60.10 (1956), pp. 1345–1347.

[190] M. Dubinin and V. Astakhov. "Development of the concepts of volume filling of micropores in the adsorption of gases and vapors by microporous adsorbents". In: *Bulletin of the Academy of Sciences of the USSR, Division of chemical science* 20.1 (1971), pp. 8–12.

[191] P. Hu and A. Adamson. "Adsorption and contact angle studies: II. Water and organic substances on polished polytetrafluoroethylene". In: *Journal of Colloid and Interface Science* 59.3 (1977), pp. 605–614.

[192] N. Vargaftik, B. Volkov, and L. Voljak. "International tables of the surface tension of water". In: *Journal of Physical and Chemical Reference Data* 12.3 (1983), pp. 817–820.

[193] Y. Xiang, M. S. Paul Fulmek, A. Foelske, and U. Schmid. "Characterization of Surface Modifications in Oxygen Plasma-Treated Teflon AF1600". In: *Langmuir* (2024).

[194] M. K. Yang, R. H. French, and E. W. Tokarsky. "Optical properties of Teflon® AF amorphous fluoropolymers". In: *Journal of Micro/Nanolithography, MEMS and MOEMS* 7.3 (2008), pp. 033010–033010.

[195] K. Sabbatovskii, V. Dutschk, M. Nitschke, F. Simon, and K. Grundke. "Properties of the teflon AF1601S surface treated with the low-pressure argon plasma". In: *Colloid Journal* 66.2 (2004), pp. 208–215.

[196] C.-C. Cho, R. Wallace, and L. Files-Sesler. "Patterning and etching of amorphous Teflon films". In: *Journal of electronic materials* 23.8 (1994), pp. 827–830.

[197] E. Liston, L. Martinu, and M. Wertheimer. "Plasma surface modification of polymers for improved adhesion: a critical review". In: *Journal of adhesion science and technology* 7.10 (1993), pp. 1091–1127.

[198] J. P. Fernández-Blázquez, D. Fell, E. Bonaccurso, and A. Del Campo. “Superhydrophilic and superhydrophobic nanostructured surfaces via plasma treatment”. In: *Journal of colloid and interface science* 357.1 (2011), pp. 234–238.

[199] D. Nečas and P. Klapetek. “Gwyddion: an open-source software for SPM data analysis”. In: *Central European Journal of Physics* 10 (1 2012), pp. 181–188. ISSN: 1895-1082. DOI: `10.2478/s11534-011-0096-2`.

[200] Y. Kwon, S. Choi, N. Anantharaju, J. Lee, M. Panchagnula, and N. Patankar. “Is the Cassie- Baxter formula relevant?” In: *Langmuir* 26.22 (2010), pp. 17528–17531.

[201] N. Vandencasteele, D. Merche, and F. Reniers. “XPS and contact angle study of N2 and O2 plasma-modified PTFE, PVDF and PVF surfaces”. In: *Surface and Interface Analysis: An International Journal devoted to the development and application of techniques for the analysis of surfaces, interfaces and thin films* 38.4 (2006), pp. 526–530.

[202] I. L. Bolotin, S. H. Tetzler, and L. Hanley. “XPS and QCM Studies of Hydrocarbon and Fluorocarbon Polymer Films Bombarded by 1- 20 keV C60 Ions”. In: *The Journal of Physical Chemistry C* 111.27 (2007), pp. 9953–9960.

[203] D. Klarman, D. Andelman, and M. Urbakh. “A model of electrowetting, reversed electrowetting, and contact angle saturation”. In: *Langmuir* 27.10 (2011), pp. 6031–6041.

[204] A. Quinn, R. Sedev, and J. Ralston. “Contact angle saturation in electrowetting”. In: *The journal of physical chemistry B* 109.13 (2005), pp. 6268–6275.

[205] A. Papathanasiou and A. Boudouvis. “Manifestation of the connection between dielectric breakdown strength and contact angle saturation in electrowetting”. In: *Applied Physics Letters* 86.16 (2005), p. 164102.

[206] A. Papathanasiou, A. Papaioannou, and A. Boudouvis. “Illuminating the connection between contact angle saturation and dielectric breakdown in electrowetting through leakage current measurements”. In: *Journal of Applied Physics* 103.3 (2008), p. 034901.

[207] S. Chevalliot, S. Kuiper, and J. Heikenfeld. “Experimental validation of the invariance of electrowetting contact angle saturation”. In: *Journal of Adhesion Science and Technology* 26.12-17 (2012), pp. 1909–1930.

[208] D. Thomas, M.-C. Audry, R.-M. Thibaut, P. Kleimann, F. Chassagneux, M. Maillard, and A. Brioude. “Charge injection in dielectric films during electrowetting actuation under direct current voltage”. In: *Thin Solid Films* 590 (2015), pp. 224–229.

[209] H. Verheijen and M. Prins. “Reversible electrowetting and trapping of charge: model and experiments”. In: *Langmuir* 15.20 (1999), pp. 6616–6620.

[210] Y. Guo, Y. Deng, B. Xu, A. Henzen, R. Hayes, B. Tang, and G. Zhou. “Asymmetrical Electrowetting on Dielectrics Induced by Charge Transfer through an Oil/Water Interface”. In: *Langmuir* 34.40 (2018), pp. 11943–11951.

[211] H. Wu, R. Dey, I. Siretanu, D. van den Ende, L. Shui, G. Zhou, and F. Mugele. "Electrically controlled localized charge trapping at amorphous fluoropolymer–electrolyte interfaces". In: *Small* 16.2 (2020), p. 1905726.

[212] M. Nania, F. Foglia, O. K. Matar, and J. T. Cabral. "Sub-100 nm wrinkling of polydimethylsiloxane by double frontal oxidation". In: *Nanoscale* 9.5 (2017), pp. 2030–2037.

[213] M. Pascual, M. Kerdraon, Q. Rezard, M.-C. Jullien, and L. Champougny. "Wettability patterning in microfluidic devices using thermally-enhanced hydrophobic recovery of PDMS". In: *Soft Matter* 15.45 (2019), pp. 9253–9260.

[214] X. Tan and D. Rodrigue. "A review on porous polymeric membrane preparation. Part II: Production techniques with polyethylene, polydimethylsiloxane, polypropylene, polyimide, and polytetrafluoroethylene". In: *Polymers* 11.8 (2019), p. 1310.

[215] L. Lin and C.-K. Chung. "PDMS microfabrication and design for microfluidics and sustainable energy application". In: *Micromachines* 12.11 (2021), p. 1350.

[216] R. A. Lawton, C. R. Price, A. F. Runge, W. J. Doherty III, and S. S. Saavedra. "Air plasma treatment of submicron thick PDMS polymer films: effect of oxidation time and storage conditions". In: *Colloids and Surfaces A: Physicochemical and Engineering Aspects* 253.1-3 (2005), pp. 213–215.

[217] M. Meincken, T. Berhane, and P. Mallon. "Tracking the hydrophobicity recovery of PDMS compounds using the adhesive force determined by AFM force distance measurements". In: *Polymer* 46.1 (2005), pp. 203–208.

[218] G. Firpo, E. Angeli, L. Repetto, and U. Valbusa. "Permeability thickness dependence of polydimethylsiloxane (PDMS) membranes". In: *Journal of Membrane Science* 481 (2015), pp. 1–8.

[219] E. Delamarche, A. Bernard, H. Schmid, A. Bietsch, B. Michel, and H. Biebuyck. "Microfluidic networks for chemical patterning of substrates: design and application to bioassays". In: *Journal of the American Chemical Society* 120.3 (1998), pp. 500–508.

[220] I. Johnston, D. McCluskey, C. Tan, and M. Tracey. "Mechanical characterization of bulk Sylgard 184 for microfluidics and microengineering". In: *Journal of Micromechanics and Microengineering* 24.3 (2014), p. 035017.

[221] M. Inoue, E. Ismail, S. Samitsu, H. Kanoh, and I. Ichinose. "High Hexane Sorption Capacity of Loosely Crosslinked PDMS Rubbers at Low Temperatures: Macromolecular and Physicochemical Elucidation for VOC Recovery". In: *Separation and Purification Technology* (2022), p. 122634.

[222] S. Béfahy, P. Lipnik, T. Pardoen, C. Nascimento, B. Patris, P. Bertrand, and S. Yunus. "Thickness and elastic modulus of plasma treated PDMS silica-like surface layer". In: *Langmuir* 26.5 (2010), pp. 3372–3375.

[223] N. Bowden, W. T. Huck, K. E. Paul, and G. M. Whitesides. "The controlled formation of ordered, sinusoidal structures by plasma oxidation of an elastomeric polymer". In: *Applied physics letters* 75.17 (1999), pp. 2557–2559.

[224] W. T. Huck, N. Bowden, P. Onck, T. Pardoen, J. W. Hutchinson, and G. M. Whitesides. “Ordering of spontaneously formed buckles on planar surfaces”. In: *Langmuir* 16.7 (2000), pp. 3497–3501.

[225] D. B. Chua, H. Ng, and S. F. Li. “Spontaneous formation of complex and ordered structures on oxygen-plasma-treated elastomeric polydimethylsiloxane”. In: *Applied Physics Letters* 76.6 (2000), pp. 721–723.

[226] J. Genzer and J. Groenewold. “Soft matter with hard skin: From skin wrinkles to templating and material characterization”. In: *Soft Matter* 2.4 (2006), pp. 310–323.

[227] H. Jiang, D.-Y. Khang, J. Song, Y. Sun, Y. Huang, and J. A. Rogers. “Finite deformation mechanics in buckled thin films on compliant supports”. In: *Proceedings of the National Academy of Sciences* 104.40 (2007), pp. 15607–15612.